TECHNISCHE UNIVERSITÄT MÜNCHEN

Fakultät für Medizin

Characterization of a MYC network dependent PRMT5 inhibitor sensitive pancreatic cancer subtype

Felix Orben

Vollständiger Abdruck der von der Fakultät für Medizin der Technischen Universität München zur Erlangung des akademischen Grades eines

Doctor of Philosophy (Ph.D.)

genehmigten Dissertation.

Vorsitzender: Prof. Dr. Marc Schmidt-Supprian

Betreuer: Prof. Dr. Günter Schneider

Prüfer der Dissertation:

1. Prof. Dr. Maximilian Reichert
2. Prof. Dr. Rainer Glaß

Die Dissertation wurde am 13.06.2022 bei der Fakultät für Medizin der Technischen Universität München eingereicht und durch die Fakultät für Medizin am 10.08.2022 angenommen.

Table of content

I. Summary

Pancreatic ductal adenocarcinoma (PDAC) has one of the highest mortality rates of all cancers and will become the second leading cause of cancer-related deaths until the end of this decade. Despite huge medical efforts, the 5-year survival rate is still unacceptably low with less than 10 %. Beside late diagnosis, one major challenge is the resistance to current chemotherapy. Especially tumor subtypes with activating aberrations of the oncogene MYC show high resistance to conventional treatment approaches and therefore, have an even worse clinical prognosis.

This work aimed to characterize MYC-associated epigenetic vulnerabilities to target MYC deregulated PDAC subtypes. These MYC-associated vulnerabilities were targeted with the protein-arginine N-methyltransferase 5 (PRMT5) inhibitor JNJ-64619178. Gain- and loss-of-function models confirmed an increased sensitivity of the PRMT5 inhibitor in cell lines with an upregulated MYC network. Furthermore, the existence of an especially sensitive PDAC subtype was demonstrated via the use of primary patient-derived cell and organoid lines. Mechanistically, PRMT5 inhibition induced DNA-damage, decreased the glycolytic activity, and arrested the cells in the G2M-phase of the cell cycle. Although all PDAC cell lines had a G2M-phase arrest, apoptotic death and inhibition of glycolysis were predominantly induced in cells with a high MYC expression. An upregulation of the alternative splicing network was also linked to a higher sensitivity, which is supported by a synergistic drug response of splicing inhibitors and PRMT5 inhibitors. In addition, it was shown that targeting of several PRMTs exceeds the therapeutic response of a PRMT5 monotherapy.

Taken together, this work characterizes a PRMT5 inhibitor sensitive PDAC subtype and investigates the underlying mechanisms in a variety of different cell models, suggesting the further development of PRMT5 inhibitor-based therapies for PDACs with aberrant MYC activity.

II. Zusammenfassung

Das Pankreaskarzinom ist eine der tödlichsten Krebsarten weltweit und es ist prognostiziert, dass es bis Ende dieses Jahrzehnts die zweithäufigste durch Krebs bedingte Todesursache wird. Trotz großer medizinischer Bemühungen verbleibt die 5-Jahresüberlebensrate bei weniger als 10 %. Neben einer oftmals späten Diagnose stellt die Resistenz gegen gegenwärtige Chemotherapien eine große Schwierigkeit bei der Behandlung von Pankreaskarzinomen dar. Vor allem Tumor-Subtypen mit einem stark aktivierten MYC-Netzwerk zeigen eine erhöhte Resistenz gegen Therapien und haben eine schlechtere klinische Prognose.

Das Ziel dieser Arbeit war es, MYC-assoziierte epigenetische Vulnerabilitäten zu charakterisieren, um Pankreaskarzinom-Zelllinien mit überregulierter MYC Expression zu behandeln. Der Inhibitor JNJ-64619178 der Protein Arginin N-Methyltransferase 5 (PRMT5) zeigte, dass diese Vulnerabilitäten gezielt ausgenutzt werden können. Gain- und Loss-of-function Modelle konnten verdeutlichen, dass die Sensitivität des PRMT5 Inhibitors JNJ-64619178 mit der Aktivität des MYC-Netzwerks korreliert. Außerdem konnte die Existenz einer besonders sensitiven Subgruppe des Pankreaskarzinoms in primären humanen Zelllinien gezeigt werden. Die Inhibition von PRMT5 induzierte Schäden an der DNA, reduzierte die Aktivität der Glykolyse und setzte die Zellen in der G2M-Phase des Zellzyklus fest. Obwohl alle Pankreaskarzinom-Zelllinien in der G2M-Phase festgesetzt wurden, wurde Apoptose und die Inhibition der Glykolyse hauptsächlich in Zellen mit erhöhter MYC-Expression festgestellt. Eine Hochregulation des alternativen Splicing-Netzwerks korrelierte ebenfalls mit einer erhöhten Sensitivität, was durch Kombinationstherapien mit Splicing- und PRMT5-Inhibitoren untermauert wurde. Ebenfalls konnte gezeigt werden, dass eine Inhibition von mehreren PRMTs die therapeutische Wirkung einer PRMT5 Monotherapie übersteigt. Zusammenfassend charakterisiert diese Arbeit eine PRMT5-Inhibitor-sensitive Untergruppe des Pankreaskarzinoms und untersucht die zugrundeliegenden Mechanismen in einer Vielzahl verschiedener Zellmodelle. Dadurch wird aufgezeigt, dass die Entwicklung von Therapieoptionen mit PRMT5 Inhibitoren einen wesentlichen Schritt für die bessere Behandlung von Patient*innen mit Pankreaskarzinom darstellen kann.

III. List of figures

IV. List of tables

V. List of abbreviations

2D/3D	Two-dimensional / three-dimensional
ADEX	Aberrantly differentiated endocrine exocrine
ATP	Adenosine triphosphate
AUC	Area under the dose response curve
AURKB	Aurora Kinase B
BET	Bromodomain and extra-terminal motif
BRD4	Bromodomain containing 4
BSA	Bovine Serum Albumin
CCND2	Cyclin D2
CCNE1	Cyclin E1
CDK	Cyclin dependent kinase
CDK4	Cyclin dependent kinase 4
CDKN2A	Cyclin dependent kinase inhibitor 2 A
CDKN2B	Cyclin dependent kinase inhibitor 1 B
CDKN2B	Cyclin dependent kinase inhibitor 2 B
CRNKL1	Crooked Neck Pre-MRNA Splicing Factor 1
CRISPR	Clustered Regularly Interspaced Short Palindromic Repeats
DMEM	Dulbecco's Modified Eagle's Medium
DMSO	Dimethylsulfoxid
DNA	Deoxyribonucleic acid
DSB	Double-strand breaks
dTAG	Degradation TAG system
E2F1	Transcription factor E2F2
E-Box	Enhancer Box
EDTA	Ethylenediaminetetraacetic acid
FBS	Fetal bovine serum
FDA	Food and Drug Administration
FOLFIRINOX	Folinic acid, 5-Flurouracil, Irinotecan, and Oxaliplatin
FOXP1	Forkhead Box P1
GSEA	Gene set enrichment analysis
GI50	Concentration for 50% growth inhibition
H3K4me3	Tri-methylation of Lys 4 at the histone H3
H2AR3	Arginine 3 at the Histone H2A
H3R8	Arginine 8 at Histone H3
HIF-1α	Hypoxia-inducible factor 1α
HR	Homologous recombination
KRAB	Krüppel associated Box
MAX	MYC associated factor X
MDM2	Mouse double minute 2 homolog
MeCP2	CpG-binding protein 2
MEP50	Methylosome protein 50

min	Minutes
MTA	Methylthioadenosine
MTAP	S-methyl-5'-thioadenosine phosphorylase
MYC	MYC proto-oncogene
NCCN	National Comprehensive Cancer Network
NHEJ	Non-homologous end joining
P/S	Penicillin/Streptomycin
PanIN	Pancreatic intraepithelial neoplastic lesions
PARP	Poly [ADP-Ribose] Polymerase
PBS	Phosphate buffered saline
PCR	Polymerase chain reaction
PDAC	Pancreatic ductal adenocarcinoma
PDCL	Patient-derived cell lines
PDO	Patient-derived organoids
PRMT	protein-arginine N-methyltransferase
RPMI	Roswell Park Memorial Institute
rRNA	ribosomal RNA
RspoI	R-spondin-I
SAH	S-adenosylhomocysteine
SAM	S-adenosylmethionine or Synergistic Activation Modulator
sec	Seconds
SMA	superior mesenteric artery
SmB	Small nuclear ribonucleoprotein B
SmD1	Small nuclear ribonucleoprotein D1
SmD3	Small nuclear ribonucleoprotein D3
SMN	Survival of Motor Neuron
SMV	superior mesenteric vein
snRNP	small nuclear ribonucleoproteins
SF3A2	Splicing Factor 3a Subunit 2
SRSF3	Serine/arginine-rich splicing factors 3
SUMO	Small ubiquitin-like modifier
TBS-T	Tris-Buffered saline buffer-Tween20
TP53	Tumor protein p53
TPX2	Targeting protein for Xklp2
US	United States of America
WDR5	WD40-repeat-containing protein 5

1. Introduction

1.1. Pancreatic Ductal Adenocarcinoma

Cancer is a major public health problem in the entire world and one of the leading causes of death in the US and Europe [1–3]. Although the mortality rates are declining, the number of cancer deaths is still increasing due to population growth and aging [4,5]. Pancreatic ductal adenocarcinoma is still one of the cancers with the poorest prognosis and a dismal 5-year survival rate of lower than 10%, which is partly because of a late diagnosis already at an advanced tumor stage [2,6,7]. Despite the extensive effort in research, it is estimated that PDAC will become the second leading cause of cancer-related deaths in the US and Germany by 2030 [1,8]. The causes which lead to pancreatic cancer are still not sufficiently understood, but some of the known risk factors are alcohol consumption, smoking, obesity, and diabetes mellitus [9]. These risk factors could also explain the worldwide distribution of PDAC incidences, with the highest incidence rates in western countries like Northern America and Europe and the lowest rates in Middle Africa and South-Central Asia [3,10].

So far, surgical resection of early and localized PDAC remains the only curative option, however, the diagnosis often comes at an advanced stage where the tumor is not resectable [11]. PDAC classified as “primary resectable” has no contact with arterial or venous vessels. The term “borderline resectable” was introduced by the National Comprehensive Cancer Network (NCCN) guidelines in 2006 [12] and describes a tumor with contact to the superior mesenteric artery (SMA) of ≤180° and contact to the superior mesenteric vein (SMV) or portal vein of >180° with the ability of resection and reconstruction. “Irresectable” describes PDAC with already distant metastasis, contact to the SMA of >180°, infiltration of the aorta, a not reconstructable invasion of the SMV or the portal vein, and contact to the first jejunal branch [13,14].

Recent insights in PDAC therapy demonstrate that neoadjuvant treatment can raise the chances of surgical tumor resection in up to 50% of the patients, even for borderline resectable and locally advanced PDAC [12,14–16]. The state-of-the-art neoadjuvant therapy includes the FOLFIRINOX (Folinic acid, 5-Flurouracil, Irinotecan, and Oxaliplatin) regime or a combination of chemoradiotherapy with Gemcitabine [14].

Although current poly-chemotherapies like FOLFIRINOX or gemcitabine plus nab-paclitaxel improved the outcome for metastatic PDAC patients with a good performance status [17], the survival rates remain unacceptably low. In contrast to other solid tumors, where targeted therapies are already well established and show pronounced survival benefit [18,19], trials for targeted therapies in pancreatic cancer are not successful. It is reported that different subgroups of PDAC have significantly different chemotherapy responses and treatment outcomes [20]. Moreover, the tumor-specific context needs to be taken into account when investigating new therapeutic targets and developing novel therapies, since the therapy response in one tumor entity cannot be extrapolated to another entity [21]. In the case of tumor progression, there are very limited options for a second-line therapy in the metastatic setting. After first-line therapy, the options that are approved by the European medicine agency and recommended by the S3-guideline consist of a combination of nanoliposomal-Irinotecan in combination with 5-FU and Leucovorin, and PARP-inhibitor maintenance therapy for gBRCA mutated patients. This indicates the need for developing new targeted therapies in the fight against PDAC.

1.1.1. Pathogenesis of pancreatic cancer

PDAC is the most frequent form of all pancreatic tumors, which encompass cancers of the endocrine and exocrine pancreas [7]. The current status of research suggests that PDAC originates from precursor lesions, which are intraepithelial neoplasias (PanINs), intraductal papillary mucinous neoplasms, or mucinous cystic neoplasms [22–24]. The majority of PDAC originates from PanINs. These are small, less than 5 mm, flat or papillary lesions, arising in the small intralobular pancreatic ducts [25,26]. PanINs are further classified with the attachment of -1, -2, and -3 based on their morphologic changes. The ductal epithelium transforms in PanIN-1 lesions into tall columnar cells with intracellular mucin. PanIN-2 lesions additionally acquired nuclear abnormalities which may include loss of polarity, nuclear crowding, or enlarged nuclei. PanIN-3 lesions are characterized by extensive nuclear crowding, a loss of nuclear polarity, luminal necrosis, and budding off of small clusters of epithelial cells into the lumen [24,25,27]. Since the Baltimore consensus meeting in 2014, PanIN-1 and PanIN-2 are summarized as “Low grade PanIN” and PanIN-3 lesions are called “High grade PanIN” [27].

During carcinogenesis and the progression throughout the different PanIN stages, genetic events accumulate. The carcinogenesis of PDAC in PanIN-1 usually starts with telomere shortening and activating mutations in *KRAS* and continues in PanIN-2 lesions with the inactivation of the *CDKN2A* tumor suppressor gene. The high-grade PanIN-3 lesions often exhibit a genetic inactivation in *TP53* and *SMAD4* [28,29] (Fig. 1). Another often found characteristic of PDAC is the aberrantly high *MYC* activation by a copy-number-variation of the *MYC* locus 8q24 [30,31]. The main tumor-drivers KRAS, TP53, and MYC are challenging therapeutic targets and were considered “undruggable” in the last decades. However, several new drugs which target these “undruggable” tumor drivers have recently entered clinical trials and will perchance make this term obsolete [32–34].

Despite KRAS being the main driver of PDAC, it is a very heterogeneous disease. Efforts to categorize PDAC grouped the cancer into four molecular subtypes based on differentially expressed gene signatures and histopathological characteristics [35]. The four subtypes are called: squamous, pancreatic progenitor, immunogenic, and aberrantly differentiated endocrine exocrine (ADEX). The squamous subtype is associated with the histological characteristics of adenosquamous carcinomas and patients with squamous PDAC have the poorest median survival with only 13.3 months [35]. The pancreatic progenitor and the immunogenic subtype are associated with mucinous carcinomas, whereas the ADEX is associated with rare acinar cell carcinomas. The median survival of these subtypes ranges from 23.7 to 30.0 months [35].

Genetic data of pancreatic cancer metastases reveals that genetically evolved clonal populations of the original parental tumor are found in the metastasis. Further analysis of the timing of the genetic evolution indicates that the development of the precursor lesion to parental, non-metastatic founder cells takes more than 10 years [36,37]. This time frame would allow early detection of the cancer and thereby, prevent the death of patients from metastatic disease. However, the options for early screening tests, which could also be performed on patients with a low risk level, are only slowly emerging [38].

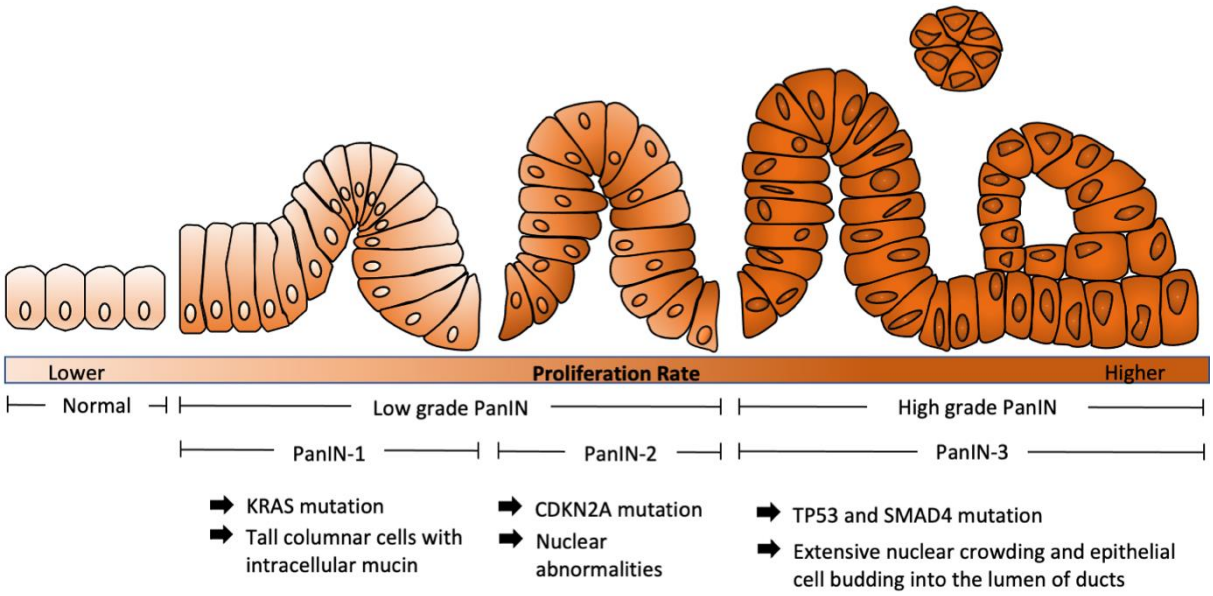

Figure 1: PDAC progression model
Progression model from pancreatic epithelial cells to PanIN-lesion. Often occurring mutations and morphological features are labeled. The color scheme indicates the proliferation rate.

1.2. MYCs physiological functions and impact on pancreatic cancer

MYC belongs to a family of oncogenic transcription factors with the three members c-MYC, N-MYC, and L-MYC which are estimated to regulate about 15% of the entire genome [39]. To bind to specific DNA sequences, MYC needs to dimerize with its partner, the basic helix-loop-helix protein MAX [40]. The main binding target of the MYC/MAX heterodimer is the Enhancer Box (E-Box) sequence CACGTG [41]. The expression of *MYC* strongly correlates with cell proliferation. Therefore, MYC is highly expressed during embryogenesis and in tissue compartments that are characterized by a high proliferative capacity [42]. On the other hand, a low *MYC* expression can be found in normal adult, uninjured, and nonproliferating pancreas cells [43]. In its physiological role, MYC is extensively involved in promoting cell-cycle progression [44,45] by activating or repressing target genes that are involved in cell-cycle regulation. Some of the first described cell cycle genes upregulated by MYC are *CCND2* (Cyclin D2), *CCNE1* (Cyclin E1), *CDK4*, and *E2F1* [46] while MYC represses CDK inhibitors such as P15 (*CDKN2B*), P21 (*CDKN2A*), and P27

(*CDKN1B*) [47]. Furthermore, it can inhibit cell differentiation and, counterintuitively, it can also induce apoptosis [48].

Due to its impact on cell proliferation, *MYC* is often deregulated in human cancers. In PanIN epithelial cells in mice, acute activation of *Myc* alone is sufficient to drive the transition to PDAC [43]. The pan-cancer analysis estimated the frequency of copy number amplifications of the *MYC* gene at approximately 14% on average in different cancer types, with the same frequency for pancreatic cancer alone [49–51]. Interestingly, amplification of *MYC* is associated with the adenosquamous subtype of PDAC, which is characterized by a worse survival and higher metastatic potential compared to other PDAC subtypes [51,52]. As mentioned above, targeting MYC remains challenging from a therapeutic view. One way to treat PDAC with oncogenic deregulated *MYC* is to take advantage of connected cellular vulnerabilities. Hassan et al. have shown that there is a synthetically lethal interaction between MYC and the small ubiquitin-like modifier (SUMO) in the context of PDAC [53] and another study has shown a synthetically lethal interaction of MYC with BET inhibitors [54].

The term synthetic lethality originates from work with *Drosophila melanogaster*, where it was defined as a situation in which inactivation of either of two genes had only little effect but the loss of function of both genes simultaneously lead to death [55]. Nowadays in cancer research, the term has been broadened and describes a state of the cell where certain perturbations of the cellular system lead to vulnerabilities that can be targeted by drugs [56].

The work presented here will introduce a novel synthetic lethality of MYC, where an MYC-associated vulnerability is exploited by using protein-arginine N-methyltransferase 5 (PRMT5) inhibitors.

1.3. Protein Arginine Methyltransferase 5

Protein arginine methyltransferases have a wide range of different epigenetic functions by controlling the methylation of proteins involved in alternative splicing, post-transcriptional regulation, proliferation, differentiation, apoptosis, and tumorigenesis [57–59]. These enzymes catalyze the transfer of methyl groups from S-adenosylmethionine (SAM) to the guanidine nitrogen residue of the amino acid arginine with the outcome of methylarginine and the by-product S-adenosylhomocysteine (SAH) [60]. The nine different members of the mammalian PRMT family are subdivided into three distinct groups based on the final form of

methylarginine products. Enzymes belonging to the type I PRMTs (PRMT1, -2, -3, -4/CARM1, -6, and PRMT8) catalyze the monomethylation and asymmetric dimethylation of arginine. Type II PRMTs (PRMT5, and the newest member PRMT9 [61]) monomethylate and symmetrically dimethylate arginine. PRMT7, the only member of the type III PRMTs, monomethylates arginine [62].

The regulation of PRMTs occurs mainly via cross-regulation, alternative splicing, or modulation with metabolites and metabolic pathways [59]. A common cross-regulation is the interaction of PRMT4 and PRMT5, which ends with the asymmetric methylation of PRMT5 at arginine 505. A lack of this methylation of PRMT5 would result in an decrease of its methyltransferase activity [63].

Another important regulation of PRMT5 is via the metabolite methylthioadenosine (MTA). MTA is generated in the polyamine biosynthesis as a side-product in the synthesis of spermidine and spermine. It is used in the methionine salvage pathway to regenerate methionine as a substrate for the enzyme S-methyl-5'-thioadenosine phosphorylase (*MTAP*) [64]. In cancer, *MTAP* is frequently co-deleted with the prevalent deletion of *CDKN2A*, on account of the close chromosomal proximity of both genes. The deletion of *MTAP* leads to accumulating levels of MTA, which, if not processed by MTAP, can interact with PRMT5 and decrease its activity by acting as an endogenous inhibitor [65].

One cellular role of PRMT5 is the regulation of transcription in both directions, activation, and repression. On the one hand, the symmetrical dimethylation of histone H2A and H4 at arginine-3 (H2AR3 and H4R3), and histone H3 at arginine-8 (H3R8) by PRMT5 mediates transcriptional repression by reducing the levels of H4K5ac [59]. On the other hand, symmetrical dimethylation of H3R2 favors WD40-repeat-containing protein 5 (WDR5) recruitment to the DNA, which trimethylates H3K4 and thereby activates transcription. Chiang et al. showed that the recruitment and symmetrical dimethylation of H3R2 of the *FOXP1* promotor via PRMT5 leads to self-renewal, proliferation, and maintenance of breast cancer stem cells [66].

Another key function of PRMT5 is the tuning of the splicing machinery via the methylation of three subunits of the Survival of Motor Neuron (SMN) complex (SmB, SmD1, and SmD3). The SMN complex is required for the assembly of small nuclear ribonucleoproteins (snRNP), which are essential components of the spliceosome. Consequently, PRMT5 depletion interferes with the spliceosome assembly and leads to aberrant splicing due to exon skipping and retention of introns with weak

5'-splice sites [59,67,68]. For the methylation of the SMN subunits, the methylosome protein 50 (MEP50) binds PRMT5 to stabilize and increase its activity while recruiting substrate proteins [69] (Fig. 2).

The depletion of PRMT5 can also cause DNA damage and genomic instability since PRMT5 is an important player in the DNA damage response. PRMT5 regulates homologous recombination of DNA double-strand breaks (DSB) via the methylation of the ATPase RuvB-like 1 (RUVBL1), which is a cofactor of the histone acetyltransferase TIP60 complex. The methylation of RUVBL1 is required for the acetylation of H4K16 by TIP60. This, in turn, promotes the displacement of the p53-binding protein 1 (53BP1), a protein complex that is associated with non-homologous end joining (NHEJ) dependent repair of DSBs [70], from DSBs and thereby allowing homologous recombination (HR) [71].

PRMT5, PRMT1, as well as PRMT4, promote oncogenesis through the control of gene expression, RNA splicing, and DNA damage response as mentioned above. With that in mind, it is not surprising that these three PRMTs are highly expressed in human cancer and the high expression correlates with a worse prognosis for patients in several different cancer types, including PDAC [72,73]. In addition, the robust connection of PRMT5 and MYC, which we observe in this work, supports the notion that PRMT5 could be a relevant target in an aggressive PDAC subtype.

The experiments in this thesis were performed with the novel PRMT5 inhibitor named JNJ-64619178. This selective and highly potent PRMT5 inhibitor binds simultaneously to the SAM- and protein substrate- binding pockets of the PRMT5/MEP50 complex [74,75]. JNJ-64619178 is currently being assessed in phase 1 clinical trials for the treatment of B cell non-Hodgkin lymphoma, myelodysplastic syndromes, and advanced solid tumors (ClinicalTrials.gov Identifier: NCT03573310; October 2021).

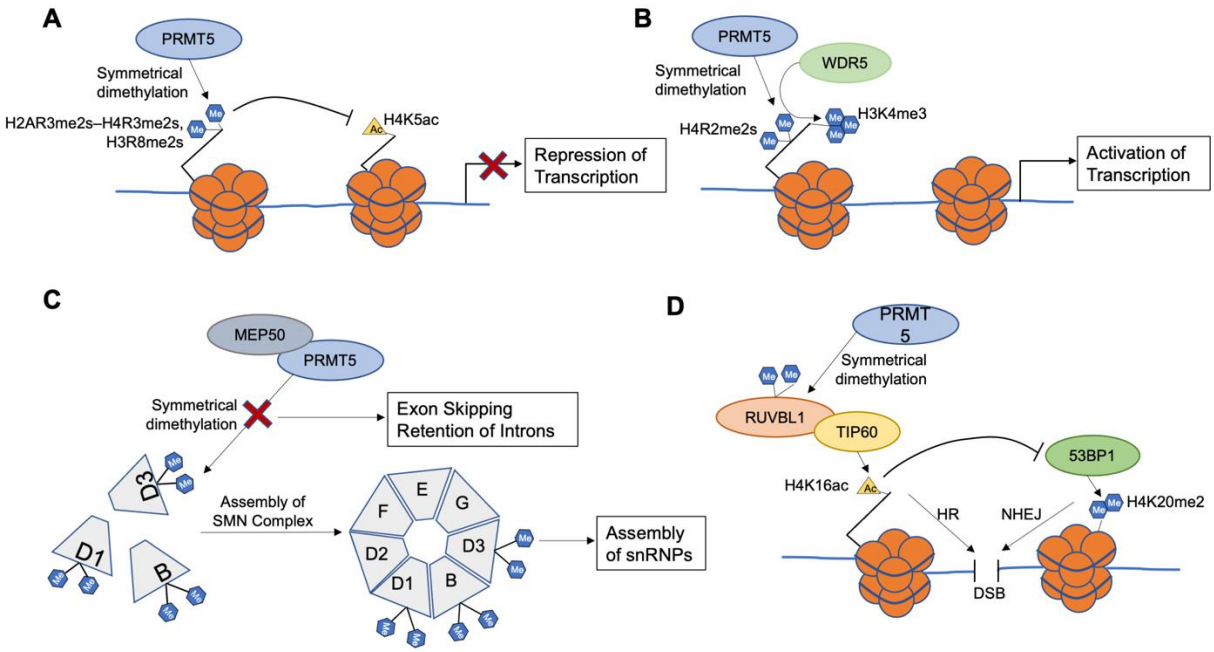

Figure 2: Functions of PRMT5

A) The symmetrical dimethylation of H2AR3 and H4R3 (H2AR3me2s–H4R3me2s) and the symmetrical dimethylation of H3R8 (H3R8me2s) by PRMT5 represses transcription by reducing the levels of acetylated H4K5 (H4K5ac). **B)** PRMT5 dimethylates H3R2 to increase WDR5 recruitment and H3K4 trimethylation, which activates transcription. **C)** PRMT5 builds a complex with MEP50, which symmetrically dimethylates the SM proteins to facilitate the assembly of small nuclear ribonucleoproteins (snRNPs). **D)** PRMT5 methylates RUVBL1 during double strand break repair (DSB) to activate TIP60α, which acetylates H4K16 (H4K16ac) to block recruitment of 53P1 to H4K20me2. This process favors DSB repair by homologous recombination (HR) over non-homologous end joining (NHEJ).

1.4. 3D-Cell culture models in cancer research

Research with cell culture has existed for more than 100 years with its beginning in the year 1907 [76]. While Harrison used embryonic tissue of frog embryos, the culturing of cells was extensively improved with cell lines originating from a wide variety of different species and human tissues. Deeper insights into various research fields including cell biology, tissue morphology, mechanisms of diseases, drug action, protein production, and the development of tissue engineering were possible due to the establishment of cell cultures [77,78]. Especially in the research of tumor biology, the optimization of therapy, and the finding of new treatment strategies proved the vast importance of cell culture systems [79].

2D cellular models are still the most common *in vitro* culturing approach, but 3D culture models have been gaining popularity in recent years. This is mainly because the 3D models offer several advantages over 2D models in terms of the representation of epithelial tissues *in vitro*, response to stimuli, drug metabolism, and protein synthesis [80]. Resembling the *in vivo* environment of a cell while being cultured *in vitro* is made possible due to a scaffold in which the cells are embedded. Hydrogels are used as a scaffold since they simulate the tissue-specific extracellular matrix of the cells and thereby mimic the physiological conditions of the cells *in vivo* [81]. The hydrogels can either be obtained from natural sources, for example Matrigel, or they are synthesized. Matrigel sustains many physiological cell functions, due to its natural source from Engelbreth-Holm-Swarm mouse sarcoma cells, which results in a high viability and controlled proliferation and differentiation of the cells [81]. Although the natural source has these advantages, there are also disadvantages of batch-to-batch variability which can alter drug responses in pharmacological studies [81]. Synthetic, unnatural hydrogels can also mimic the biological properties of the extracellular matrix and have the advantage of reproducibility due to consistency between different batches. But in contrast to hydrogels from natural sources, unnatural synthetic hydrogels lack adhesive moieties of extracellular matrices [81].

An important point in the discovery of new drugs is the understanding of the interaction between cells and the extracellular matrix [82]. 2D cell models are unable to mimic the complex microenvironment of the tumor and are probably one reason why many new drugs fail in clinical trials [81,83]. Cells cultured in 3D can aid the transition from new drug discoveries into the clinic because of the following advantages compared to 2D models: First, 3D cell cultures can be obtained from a variety of different tumor entities, which enables the creation of biobanks with cell lines from different patients [84]. Second, cells cultured in 2D are often all in the same stage of the cell cycle whereas 3D models are often in different cell cycle stages like cells *in vivo* [80]. Third, all the cells in a 2D monolayer receive the same amount of nutrients and growth factors from the medium. The 2D cell are mainly actively proliferating cells since necrotic cells tend to detach from the surface and get washed out [85]. In a 3D organoid, the outer layer is highly exposed to the medium and consists of proliferating cells, whereas the inner cells receive fewer growth factors and oxygen. The cells in the center of the organoid tend to be in a quiescent state with a necrotic core in the middle. This cellular heterogeneity is much closer

to what we see in tumor tissues *in vivo* [85]. Most importantly, it has been shown that the response to a drug treatments in 3D cultures represents better the clinical findings, compared to 2D cultures [86–88]. These reasons highlight why 3D cultures are a superior approach and essential for the successful discovery of novel therapeutic targets in cancer therapy.

1.5. Aim of the thesis

This thesis aimed to find a novel strategy to therapeutically target pancreatic cancer. Therefore, the Schneider Laboratory (Klinikum rechts der Isar, Munich) conducted a large screen with 181 epigenetic drugs to find drugs that are especially potent in PDAC cells with a high MYC level. It was proposed that PDAC can only be clustered into different subgroups, when using the whole epigenomic orchestra [89]. With that in mind, the library of epigenetic drugs is a valid approach to find suitable drug candidates to target MYC-driven PDAC. One of the top hits was a PRMT5 inhibitor, which is in phase I clinical trials for solid cancers. This study aims to provide an in-depth analysis of the inhibitor response in PDAC subtypes throughout different human and murine cell models. For a better investigation of the treatment response, loss- and gain-of-function models of PDAC cell lines were established. Finally, the study aimed to discover the fate of cells after treatment with a PRMT5 inhibitor. Consequently, the mode of death and the metabolomic changes of the cells after drug treatment were investigated.

This study will shed new light on the impact of PRMT5 inhibition in PDAC and might in the long-term, help to improve treatment for patients with pancreatic cancer via personalized and targeted therapy options.

2. Material

Table 1: Technical equipment.

Instrument	Company
AS2000 Maxwell® 16 instrument	Promega, Walldorf, Germany
FC Multiscan	Thermo Fisher Scientific, Munich, Germany
FLUOstar® OPTIMA	BMG Labtech, Champigny-sur-Marne, France
MIKRO 220 R table centrifuge	Hettich, Kirchlengern, Germany
Mini-PROTEAN® Tetra Vertical, 1.5 mm	Bio-Rad, Munich, Germany
NB-203XL CO_2 Incubator	N-BIOTEK Co., Ltd., Gyeonggi-Do, Korea
Odyssey® Fc	Li-cor Biosciences GmbH, Bad Homburg vor der Höhe, Germany
Odyssey® Infrared Imaging System (RRID:SCR_013430)	Licor Biosciences GmbH, Bad Homburg, Germany
PERFECTION V370 PHOTO DIN A4 Photoscanner	Epson, Suwa, Japan
Rotina 380 R	Hettich, Kirchlengern, Germany
Seahorse XFe96 Analyzer	Agilent, CA, USA
StepOnePlus Real-Time PCR System (4376357)	Applied Biosystems, Munich, Germany
T100 Thermal Cycler	Bio-Rad, Munich, Germany
ThermoMixer® C	Eppendorf, Munich, Germany
Wet/Tank blotting system	Bio-Rad, Munich, Germany

Table 2: Kits.

Kit	Catalogue Number	Company
Caspase-Glo 3/7 Assay	G8091	Promega, Walldorf, Germany
CellTiter-Glo® Luminescent Cell Viability Assay	G7570	Promega, Walldorf, Germany
Glucose Uptake-Glo Assay	J1342	Promega, Walldorf, Germany
GoTaq® qPCR Master Mix	A6101	Promega, Walldorf, Germany
Maxwell® 16 LEV simplyRNA Purification Kits	AS1280	Promega, Walldorf, Germany
NucleoSpin Plasmid, Mini kit	740588.250	Macherey-Nagel GmbH, Düren, Germany
NucleoSpin Plasmid Transfection-grade	740490.10	Macherey-Nagel GmbH, Düren, Germany
QIAampt DNA Mini Kit	51306	Qiagen, Hilden, Germany
RNeasy Mini Kit	74106	Qiagen, Hilden, Germany

Seahorse XF Cell Mito Stress Test	103015-100	Agilent Technologies, CA, USA
Seahorse XF Glycolysis Stress Test	103020-100	Agilent Technologies, CA, USA

Table 3: Compounds and reagents.

Compounds/Reagents	**Catalogue Number**	**Company**
24-well Polypropylene Microplates, clear, Corning®	142475	Thermo Fisher Scientific, Munich, Germany
384-well White/Clear Bottom Polystyrene Microplates, Corning®	3765	Thermo Fisher Scientific, Munich, Germany
80% Ethanol	N-33635	Brüggemann Alcohol, Heilbronn, Germany
96-well Polypropylene Microplates, clear, Corning®	3343	Thermo Fisher Scientific, Munich, Germany
ACK Lysing Buffer	A1049201	Thermo Fisher Scientific, Munich, Germany
Albumin	11930.03	Serva, Rosenheim, Germany
Bradford Reagent	39222.01	Serva, Rosenheim, Germany
BsmBI-v2 restriction enzyme	R0739	New England Biolabs., Frankfurt a. Main, Germany
Cell Recovery Solution, 100 mL Corning®	354253	Thermo Fisher Scientific, Munich, Germany
Cell Scraper	83.1830	Starstedt, Nümbrecht, Germany
Cellstar Cell culture bottle	660175	Greiner BIO-ONE, Kremsmünster, Austria
CELLSTAR® Polypropylen Tubes	227261	Greiner BIO-ONE, Kremsmünster, Austria
cOmplete™, Mini, EDTA-free Protease Inhibitor Cocktail	11836170001	Roche Diagnostics GmbH, Basel, Swiss
Costar® TC-Treated Multiple Well Plates 24-well, Corning®	CLS3527	Sigma-Aldrich, Munich, Germany
Costar® TC-Treated Multiple Well Plates 6-well, Corning®	CLS3516	Thermo Fisher Scientific, Munich, Germany
Crystal violet	C6158	Sigma-Aldrich, Munich, Germany
DMSO	A3672	AppliChem, Darmstadt, Germany
dNTP-Mix	331550	Biozym Scientific GmbH, Hessisch Oldendorf, Germany
Dulbecco´s Modified Eagle´s Medium	D5030	Sigma-Aldrich, Munich, Germany

Advanced DMEM	1249102	Life Technologies, Darmstadt, Germany
Dulbecco´s PBS	D8537- 500 mL	Sigma-Aldrich, Munich, Germany
EDTA (Versen) 1% (w/v) in PBS w/o CA^{2+}	L 2113	Biochrom GmbH, Berlin, Germany
Eppendorf Safe-Lock Tubes, 1.5 mL	0030120086	Eppendorf, Munich, Germany
Eppendorf Safe-Lock Tubes, 2mL	0030120094	Eppendorf, Munich, Germany
Ethidium promide solution	E1510	Sigma-Aldrich, Munich, Germany
Falcon® Round-Bottom Polystyrene Tubes	38055	STEMCELL Technologies, Cologne, Germany
Falcon™ Chambered Cell Culture Slides	10364551	Thermo Fisher Scientific, Munich, Germany
FBS Superior	S 0615	Merck, Darmstadt, Munich
Filtropur	20003477	Starstedt, Nümbrecht, Germany
Gel Saver-Tip II	GSII054R	Kisker Biotech GmbH & Co. KG, Steinfurt, Germany
Geneticin	10131035	Thermo Fisher Scientific, Munich, Germany
GSK3368715	HY-128717	Medchem Express,USA
Hygromycin B	10687010	Thermo Fisher Scientific, Munich, Germany
Indisulam	HY-13650	Medchem Express,USA
JNJ-64619178	HY-101564	Medchem Express,USA
Lipofectamine 3000 Transfection Reagent	L3000001	Thermo Fisher Scientific, Munich, Germany
Matrigel®, Growth Factor Reduced (GFR) Basement Membrane Matrix, LDEV-free, Corning®	354230	Thermo Fisher Scientific, Munich, Germany
Mini-PROTEAN Comb	1653365	Bio-Rad, Munich, Germany
MTT	M5655	Sigma-Aldrich, Munich, Germany
Multiscribe Reverse Transcriptase	4308228	Thermo Fisher Scientific, Munich, Germany
Neubauer counting chamber	10490171	Thermo Fisher Scientific, Munich, Germany
Nitrocellulose Blotting Membrane	10600001	Bio-Rad, Munich, Germany
Nonfat-Dried Milk Bovine	M7409	GE Healthcare Life Science, Freiburg im Breisgau, Germany
Opti-MEM with GlutaMAX, Gibco	12559099	Thermo Fisher Scientific, Munich, Germany

Page RulerTM Prestained	26616	Thermo Fisher Scientific, Munich, Germany
PCR® MICROPLATE, Axygen	PCR-96-LP-AP-C	Thermo Fisher Scientific, Munich, Germany
Phosphatase-Inhibitor-mix I, powder	39050.03	Serva, Rosenheim, Germany
Platemax CyclerSeal Sealing Film, Axygen	PCR-TS	Thermo Fisher Scientific, Munich, Germany
Polybrene Infection / Transfection Reagent	TR-1003	Sigma-Aldrich, Munich, Germany
PureLink™ RNase A, 10 mL, Invitrogen	1772940	Thermo Fisher Scientific, Munich, Germany
Puromycin	ant-pr-1	Invivogen, San Diego, CA, USA
Random Hexamers	11034731001	Hoffmann-La Roche, Basel, Switzerland
Recovery Cell Culture Freezing Medium	12648010	Thermo Fisher Scientific, Munich, Germany
REDTaq® ReadyMix™ PCR Reaction Mix	R2523	Sigma-Aldrich, Munich, Germany
RNase Inhibitor	N8080119	Thermo Fisher Scientific, Waltham, Massachusetts, USA
RPMI 1640 Medium, GlutaMAX™ Supplement	61870036	Life Technologies, Darmstadt, Germany
Safe seal tube, 1.5 mL	72.706	Starstedt, Nümbrecht, Germany
SDS NA-salt in Pellets	20765.03	Serva, Rosenheim, Germany
Seahorse XF RPMI Medium, pH 7.4	103576-100	Agilent Technologies, USA
Seahorse XF Base Medium	102353-100	Agilent Technologies, USA
SGC707	HY-19715	MedChem Express, USA
T4 DNA Ligase	M0202S	New England Biolabs., Frankfurt a. Main, Germany
T4 DNA Ligase Reaction Buffer	B0202S	New England Biolabs., Frankfurt a. Main, Germany
TaqMan RT Buffer 10x	4486220	Thermo Fisher Scientific, Waltham, Massachusetts, USA
tissue-culture treated culture dishes, Corning®	CLS430599	Thermo Fisher Scientific, Munich, Germany
TrypLE™ Express Enzyme (1x), 100 mL	12604013	Thermo Fisher Scientific, Munich, Germany
Tween® 20	9127.2	Carl Roth, Karlsruhe, Germany
Zeocin	ant-zn-1	Invivogen, San Diego, CA, USA

Table 4: Plasmids and bacteria

Plasmid/ sgRNA / Bacteria	**Catalouge number**	**Company**
lenti_dCas9-KRAB-MeCP2	122205	Addgene, Watertown, MA USA
lenti dCas9-VP64_Blast	61425	Addgene, Watertown, MA USA
lentiCRISPRv2 puro	98290	Addgene, Watertown, MA USA
lentiGuide-Puro	52963	Addgene, Watertown, MA USA
lenti MS2-p65-HSF1_Hygro	61426	Addgene, Watertown, MA USA
lenti sgRNA (MS2)_zeo backbone	61427	Addgene, Watertown, MA USA
One Shot™ Stbl3™ Chemically Competent *E. coli*	C737303	Thermo Fisher Scientific, Munich, Germany
pMD2.G	12259	Addgene, Watertown, MA USA
psPAX2	12260	Addgene, Watertown, MA USA

Table 5: sgRNA-inserts.

Name	**Sequence forward primer**	**Function**
CRISPRi-Myc1	5´-CACCGCGAAGCCCCCTATTCGCTC-3´	c-MYC downregulation with dCas9 System
CRISPRi-Myc2	5´-CACCGTTAGATAAAGCCCCGAAAAC-3´	c-MYC downregulation with dCas9 System
CRISPRi-Myc3	5´-CACCGCGCTCCGGATCTCCCTTCCC-3´	c-MYC downregulation with dCas9 System
hsMyc-3	5´-CACCGCTGTAGTAATTCCAGCGAG -3´	c-MYC downregulation with dCas9 System
hsMyc-4	5´-CACCGGAATAGGGGGCTTCGCCTC -3´	c-MYC downregulation with dCas9 System

MYC 1	5´-CACCGAGGGTGGGGAGGGTGGGGA-3´	c-MYC upregulation with dCas9 system
MYC 2	5´-CACCGTTCCCCCACGCCCTCTGCTT-3´	c-MYC upregulation with dCas9 system
Myc 3	5´-CACCGAACCCGGGAGGGGCGCTTA-3´	c-MYC upregulation with dCas9 system
Myc A	5´-CACCGAACCCGGGAGGGGCGCTTAT-3´	c-MYC upregulation with dCas9 system
Myc B	5´-CACCGACCCTCGCATTATAAAGGGC-3´	c-MYC upregulation with dCas9 system
PRMT5i	5´-CACCGAGCCGCGTGTCCAGCGGGA-3´	PRMT5 downregulation with dCas9 system

Table 6: Ingredients of medium for patient-derived organoid culture.

Product	**Catalogue Number**	**Final conc.**	**Company**
3,3,5-Triiodo-L- thyronine	T2877	5 nM	Sigma-Aldrich, Munich, Germany
A83-01	72022	0,5 µM	STEMCELL Technologies, Cologne, Germany
Bovine Pituitary Extract	P1476	25 µg/ml	Sigma-Aldrich, Munich, Germany
Cholera toxin	C8052	100 ng/ml	Sigma-Aldrich, Munich, Germany
D-Glucose	G8270	5 mg/mL	Sigma-Aldrich, Munich, Germany
Dexamethasone	D1756	1 µM	Sigma-Aldrich, Munich, Germany
DMEM/F12-500 mL	11330032	-	Thermo Fisher Scientific, Munich, Germany
ITS + premix, Corning®	10070791	0.5% (w/v)	Thermo Fisher Scientific, Munich, Germany

Neuregulin	100-03	100 ng/ml	Pepro Tech, Hamburg, Germany
Nicotinamide	N3376	10 mM	Sigma-Aldrich, Munich, Germany
Nu-Serum IV, Corning®	355100	5% (v/v)	Thermo Fisher Scientific, Munich, Germany
Penicillin/Streptomycin	15140-122	1% (v/v)	Thermo Fisher Scientific, Munich, Germany
Primocin	Ant-pm-1	100 µg/ml	Invivogen, San Diego, CA, USA
Rock inhibitor Y-27632	72304	10 µM	STEMCELL Technologies, Cologne, Germany

Table 7: Primary and secondary antibodies.

Antibody	**Catalogue Number**	**RRID**	**Dilution**	**Source**	**Company**
β-ACTIN	A5316	AB_476743	1:10,000	mouse, monoclonal	Sigma-Aldrich, Darmstadt, Germany
Anti-mouse IgG (H+L) (DyLight™ 680 Conjugate)	5470	AB_10696895	1:10,000	mouse	Cell Signaling, Danvers, MA, USA
Anti-mouse IgG (H+L) (DyLight™ 800 4X PEG Conjugate)	5257	AB_10693543	1:10,000	mouse	Cell Signaling, Danvers, MA, USA
Anti-rabbit IgG (H+L) (DyLight™ 680 Conjugate)	5366	AB_10693812	1:10,000	rabbit	Cell Signaling, Danvers, MA, USA
Anti-rabbit IgG (H+L) (DyLight™ 800 4X PEG Conjugate)	5151	AB_10697505	1:10,000	rabbit	Cell Signaling, Danvers, MA, USA
Aurora Kinase B	3094S	AB_10695307	1:1,000	rabbit	Cell Signaling, Danvers, MA, USA
BRD4	13440	AB_2687578	1:1,000	rabbit	Cell Signaling, Danvers, MA, USA
c-MYC	9402	AB_2151827	1:1,000	rabbit, polyclonal	Cell Signaling, Danvers, USA

Cleaved PARP	51-9000017		1:1,000	mouse	BD Pharmingen, San Diego, California, USA
E-Cadherin	3195	AB_2291471	1:1,000	rabbit	Cell Signaling, Danvers, MA, USA
MTAP	4158	AB_1904054	1:1,000	rabbit	Cell Signaling, Danvers, MA, USA
PRMT1	2449	AB_2237696	1:1,000	rabbit	Cell Signaling, Danvers, MA, USA
PRMT5	79998S	AB_2799945	1:1,000	rabbit	Cell Signaling, Danvers, MA, USA
Snail1	3879	AB_2255011	1:1,000	rabbit	Cell Signaling, Danvers, MA, USA
TPX2	NB500-179	AB_10002747	1:1,000	rabbit polyclonal	Novus Biologicals, CO, USA
Vimentin	5741	AB_10695459	1:1,000	rabbit	Cell Signaling, Danvers, MA, USA

Table 8: Buffers, gels, and solutions.

Name	**Ingredients**
Freezing Medium	Dulbecco´s Modified Eagles Medium, high glucose 10% (v/v) FCS 10% (v/v) DMSO
KCM Buffer (5x)	0.5 M KCl 0.15 M $MCaCl_2$ 0.25 mL $MgCl_2$
Laemmli Buffer (5x)	250 mM Tris-HCl (pH 6.8) 4% (w/v) SDS 40% (v/v) Glycerol 0.05% (w/v) Bromphenolblue add 5% (v/v) β-Mercaptoethanol before usage
LB-Agar	4% (w/v) LB-Agar powder, (Luria/Miller) X.969.2, Carl Roth, Karlsruhe, Germany 100 µM (v/v) Ampicillin
LB-Medium	2.5% (v/v) LB-Medium powder, (Luria/Miller) X968.1, Carl Roth, Karlsruhe, Germany 50 µM Ampicillin

PBS (1x)	137 mM Sodium chloride 270 µM Kalium chloride 4.0 mM Disodium phosphate
Resolving gel (10%)	390 mM Tris-HCl, pH 8.8 10% (v/v) Acrylamide 0.1% (v/v) SDS 0.05% (v/v) APS 0.05% (v/v) Temed
Resolving gel (15%)	300 mM Tris-HCl, pH 8.8 15% (v/v) Acrylamide 0.1% (v/v) SDS 0.05% (v/v) APS 0.05% (v/v) Temed
Resolving gel (7.5%)	390 mM Tris-HCl, pH 8.8 7.5% (v/v) Acrylamide 0.1% (v/v) SDS 0.05% (v/v) APS 0.05% (v/v) Temed
RIPA Buffer	150 mM $NaCl_2$ 1% (w/v) NP40 0.5% (w/v) Sodium Deoxychlorate (DOC) 0.1% (w/v) SDS 50 mM Tris-HCl, pH 8
Running Buffer (1x)	192 mM Glycine 25 mM TRIS 3.47 mM SDS
SDS Lysis Buffer	2% (w/v) SDS 40 mM Tris-HCl, pH 7.6
Stacking gel (4.4%)	125 mM Tris-HCl, pH 6.8 4.4% (v/v) Acrylamide 0.1% (v/v) SDS 0.05% (v/v) APS 0.2% (v/v) Temed
TBS Buffer	100 mM Tris 150 mM NaCl adjusted to pH 8.0
TE Buffer	1 mM Tris-HCl (pH 8.0) 0.5 M EDTA
Transfer Buffer (1x)	192 mM Glycine 25 mM TRIS 20% (v/v) Methanol

Table 9: 2D cell lines.

Cell line	Source	Disease	Medium	RRID number
HEK293FT	Human	Embryonic kidney	DMEM	CVCL_6911
DANG	human	Pancreatic adenocarcinoma	RMPI	CVCL_0243
HPAC	human	Pancreatic adenocarcinoma	DMEM	CVCL_3517
HupT3	human	Pancreatic adenocarcinoma	RPMI	CVCL_1299
Panc-1	human	Ducts, epithelioid carcinoma	DMEM	CVCL_0480
PATU8988S	human	Pancreatic adenocarcinoma	DMEM	CVCL_1846
PATU8988T	human	Pancreatic adenocarcinoma	DMEM	CVCL_1847
PSN1	human	Pancreatic adenocarcinoma	RMPI	CVCL_1644
B211	human	Pancreatic adenocarcinoma	RPMI Glutamax	
B290	Human	Pancreatic adenocarcinoma	RPMI Glutamax	
huPDAC11	human	Pancreatic adenocarcinoma	RPMI Glutamax	
huPDAC3	human	Pancreatic adenocarcinoma	RPMI Glutamax	
huPDAC1	human	Ducts, epithelioid carcinoma	RPMI Glutamax	
huPDAC7	human	Pancreatic adenocarcinoma	RPMI Glutamax	
huPDAC17	human	Pancreatic adenocarcinoma	RPMI Glutamax	
PDC40	human	Pancreatic adenocarcinoma	RPMI Glutamax	
PDC49	human	Pancreatic adenocarcinoma	RPMI Glutamax	
PDC56	human	Pancreatic adenocarcinoma	RPMI Glutamax	
PDC117	human	Pancreatic adenocarcinoma	RPMI Glutamax	
PDC148	Human	Pancreatic adenocarcinoma	RPMI Glutamax	
Pacaad119	human	Ducts, epithelioid carcinoma	Advanced DMEM	
Pacaad137	human	Pancreatic adenocarcinoma	Advanced DMEM	
Pacaad159	human	Pancreatic adenocarcinoma	Advanced DMEM	

Pacaad161	human	Pancreatic adenocarcinoma	Advanced DMEM
Pacaad165	human	Pancreatic adenocarcinoma	Advanced DMEM
MW1955	Murine	Pancreatic adenocarcinoma	DMEM

Table 10: Software.

Software	**Company**
Adobe Illustrator CC 2018	Adobe Inc., San José, CA, USA
FlowJo 8.8.6	FlowJo, Becton Dickinson, Franklin Heights, NJ, USA
GraphPad Prism Software v5/8	GraphPad Software, San Diego, CA, USA
ImageJ	NIH, Bethesda, MD, USA
Image Studio Lite Software (RRID:SCR_013715)	LiCor Biosciences, Bad Homburg, Germany
Microsoft Office 2010	Microsoft, Redmond, WA, USA
NanoDrop ND-1000 3.1	NanoDrop, Informer Technologies, Inc.,
R software	R Core Team, GNU GPL
StepOne Software V2.3	Thermo Fisher Scientific, Munich, Germany

3. Methods

3.1. Cell lines, mycoplasma contamination, authentication

Depending on the cell line, human pancreatic cancer cell lines were cultured in Dulbecco's Modified Eagle's Medium–high glucose (#D5796, Sigma-Aldrich, Darmstadt, Germany) or RPMI GlutaMAX® (#61870036, Life Technologies, Darmstadt, Germany) medium with 10% (v/v) fetal calf serum (FCS) (#TMS-013-B, Merck Millipore, Berlin, Germany) and 1% (v/v) Penicillin/Streptomycin (#15140122, Life Technologies, Darmstadt, Germany). DMEM: HEK293FT (RRID:CVCL_6911) PANC-1 (RRID:CVCL_0480), PaTu8988T (RRID:CVCL_1847), PaTu8988S (RRID: CVCL_1846); RPMI: DanG (RRID: CVCL_0243), HPAC (RRID:CVCL_3517), PSN1 (RRID:CVCL_1644), HupT3 (RRID:CVL_1299). Authentication was performed regularly (10/2021) by Multiplexion (Multiplexion GmbH, Heidelberg, Germany) or Microsynth (Microsynth AG, Balgach, Switzerland). The murine pancreatic cancer cell line MW1955 was established from $Kras^{G12D}$-driven mouse models of pancreatic cancer. The murine cell line MW1955 was generated with the dual recombinase System[90] with the aim, to generate a murine PDAC cell line where the floxed *Myc* alleles[91] can be deleted by a tamoxifen activatable Cre (CRE^{ERT2}). The cell line has the following genotype: *Pdx1-Flp*; *FSF-Kras*$^{G12D/+}$; *FSF-R26*$^{CAG\text{-}CreERT2/+}$; *Myc*$^{lox/lox}$. Additionally, the dTAG-System was transduced in this cell line according to the publication by Nabet et al [92]. Briefly, a vector containing the $FKBP12^{F36V}$-Myc fusion protein was transduced into the cell and in the following called MW1955-MYC-dTAG. The cell line MW1955-dTAG-MYC expresses the endogenous *Myc* and the exogenous *Myc-FKBP12*^{F36V} fusion gene. To establish an additional cell line, which expresses only the exogenous fusion protein, the cell line was treated with 4-hydroxytamoxifen. This treatment activates the Cre recombinase which results in a deletion of the floxed *Myc* exons. The cells were seeded as single cells in a 96-well plate with murine cell culture medium. Successful deletion of the endogenous Myc was tested on a PCR with the following primers: myc-del-fwd: 5´-TCGCGCCCCTGAATTGCTAGGAA-3´; myc-del-rev: 5´-TGCCCAGATAGGGAGCTGTGATACTT-3´. The cell line MW1955-empty-dTAG has only a vector consisting of the gene $FKBP12^{F36V}$.

The murine cell lines were cultured in high glucose DMEM medium (Sigma-Aldrich, Darmstadt, Germany) with 10% (v/v) FCS (Merck Millipore, Berlin, Germany) and 1% (v/v) Penicillin/Streptomycin (Life Technologies, Darmstadt, Germany).
All cell lines were split in the same way, described in the following: The cell lines were washed with Dulbecco's phosphate-buffered saline (PBS) (Sigma-Aldrich, Darmstadt, Germany) and detached from the flask and plates using EDTA (1% in PBS w/o Ca^{2+} w/o Mg^{2+}; #L2113, Biochrom, Darmstadt, Germany) diluted 1:20 in PBS.
Regular contamination tests for mycoplasma were done by PCR. Therefore, cells were seeded in 6-well plates in 3ml of their respective medium without antibiotics. After one week, 2ml of the medium was transferred in an Eppendorf tube and centrifuged at RT at 250xg for 2 minutes. The supernatant was pipetted into a fresh tube and centrifuged again for 10 minutes at RT at 20000xg. The supernatant was aspirated, and the pellet was resuspended in the remaining liquid. The pellet was then heat-inactivated at 95°C for 3minutes. 2µl was used as a template in the following PCR (PCR mix (1x):15µl Red-Taq Premix (Sigma-Aldrich), 2µl 5`Primer dilution (10µl of each 5`Primer (10µM) + 30µl H2O), 2µl 3`Primer dilution (10µl of each 3`Primer (10µM) + 70µl H2O), 9µl H2O). The following primers were used: 5`Primer 1: 5`C G C C T G A G T A G T A C G T T C G C 3`; 5`Primer 2: 5`C G C C T G A G T A G T A C G T A C G C 3`; 5`Primer 3: 5` T G C C T G G G T A G T A C A T T C G C 3`; 5`Primer 4: 5` T G C C T G A G T A G T A C A T T C G C 3`; 5`Primer 5: 5`C G C C T G A G T A G T A T G C T C G C 3`; 5`Primer 6: 5`C A C C T G A G T A G T A T G C T C G C 3`; 5`Primer 7: 5`C G C C T G G G T A G T A C A T T C G C 3`; 3`Primer 1: 5`G C G G T G T G T A C A A G A C C C G A 3`; 3`Primer 2: 5`G C G G T G T G T A C A A A A C C C G A 3`; 3`Primer 3: 5`G C G G T G T G T A C A A A C C C C G A 3`. The PCR protocol was as followed: 95°C 15 minutes; (94°C for 1 minute, 60°C for1 minute, 74°C for 1 minute) x40; 72°C 10 minutes. The PCR product was loaded on a 2% agarose gel and separated via gel electrophoresis for 1 hour at 100V. Visualization was performed by using the UVsolo TS Imaging System (Biometra, Analytik Jena AG, Jena, Germany).

3.2. Human primary PDAC organoid culture

The primary human PDAC 3D organoid models were established and analyzed in accordance with the declaration of Helsinki and were approved by the local ethical

committee TUM, Klinikum rechts der Isar and LMU, Klinikum der Universität München (Project 207/15, 946/07, 330/19S, 80/17S, and 17-648). Written informed consent from the patients for research use were obtained before the investigation. The PDAC 3D organoid lines LMU1, LMU2, LMU3, and LMU13 were a gift from the research groups from Prof. Dr. Julia Mayerle and Dr. Georg Beyer (LMU, Klinikum der Universität München) Clinical parameters of the 3D lines are depicted in Stable4.

3.2.1. Generation of organoids

Primary patient derived PDAC 3D organoids were generated from primary pancreatic cancer. The cells or tissues for the establishment of the organoid lines were obtained from fine needle aspiration/biopsies (FNA/B) or surgical resected cancers. The isolation process was performed shortly after receiving the sample on ice (less than 20 minutes). The isolation process started by washing the sample with PBS. After a centrifugation step (5 minutes, 1000 rpm, 4°C), the supernatant was aspirated, and the sample was transferred to a cell culture plastic dish to mechanical dissect the specimen into small pieces with a scalpel. FNA/B samples were transferred into a 15-ml Falcon tube filled with 5 ml PBS. Surgical samples needed an additional digestion step and were transferred into a 15-ml Falcon tube filled with 5 ml of digestion buffer (Advanced DMEM-F12 (#12634010 Thermo Fisher Scientific, Massachusetts, USA), 1 M Hepes, 1 x Glutamax Supplement (#35050061, Thermo Fisher Scientific, Massachusetts, USA), 1 x Primocin (#ant-pm-2, Invivogen), 6 mg/ml Collagenase II (#17101-015 Thermo Fisher), 2.5% Fetal Calf Serum (#TMS-013-B, Merck-Millipore, Berlin, Germany). The surgical sample was then digested for 1h in a rotating mixer with 30 rpm. To allow sedimentation of the debris, the Falcon tube was placed upright for 10 seconds. The supernatant was transferred in a new 15-ml Falcon tube to avoid carryover of the debris. FNA/Bs and surgical specimen were then centrifuged for 5 minutes at 1000 rpm and 4°C. To lyse the red blood cells, the supernatant was discarded, and the tissue pellet was resuspended in 3 ml red blood cell lysis buffer (#A1049201, ACK Lysis Buffer from Thermo Fisher Scientific, Massachusetts, USA) for 3 to 10 minutes at room temperature. The incubation time depended on the amount of red blood cells in the sample. After a washing step in PBS and following centrifugation (5 minutes, 1000 rpm, 4°C), the samples were digested in 3 ml TrypLE (#12604039, Thermo Fisher

Scientific, Massachusetts, USA) for 3 – 5 minutes at 37°C. Afterward, an additional washing and centrifugation step was performed. Then, the supernatant was discarded, and the cell pellet was dissolved in Matrigel (#354230, Corning Life Sciences, Corning, NY 14831 USA) and plated on a prewarmed 24-well plate (depending on the sample size 2 – 8 wells on a 24 well plate with 50 µl Matrigel/well). To allow stiffening of the Matrigel, 500 µl of PDO culture medium was added to each well after incubation in the incubator for 10 minutes.

3.2.2. Passaging of the organoids

To passage the organoids, the media in the 24-well plates with the organoids was aspirated and 250 µl of Cell Recovery Solution (#11543560, Fisher Scientific) was added to each well. To allow a good recovery of the organoids, the PBS needs to be ice cold to liquefy the Matrigel. The Matrigel with the organoids and Cell Recovery solution was resuspended by adding 1 ml of ice-cold PBS w/o Ca^{2+} w/o Mg^{2+} (Sigma Life Sciences), supplemented with 0.1% BSA (#11930, Serva, Heidelberg, Germany and pipetting the solution up and down with a p1000 pipette. The resuspended solution was then transferred into a 15-ml falcon tube and centrifuged at 1000 rpm at 4°C for 5 minutes. Afterward, the supernatant was aspirated till 2 ml are remaining. The organoid cell pellet was further disrupted by resuspending the pellet in these 2 ml PBS by pipetting up and down. Afterward, the falcon tube was filled with 6 ml ice-cold PBS and centrifuged at 1000 rpm at 4°C for 5 minutes. The supernatant was again discarded, and the cell pellet was resuspended in 50 µl/well of Matrigel. The amount of Matrigel depends on the planned number of wells for the subsequent organoid culture and was decided individually for every cell line. In general, the splitting ratio ranges from 1:1 to 1:3. The medium was changed twice a week.

3.2.3. Detection of KRAS mutations

For this thesis, only KRAS mutated organoids were used for experiments. KRAS mutations (see Stable 4) were determined by Sanger Sequencing. By using the DNA/RNA Micro Kit (#80284, Qiagen, Germany), the organoid DNA was isolated and then amplified by performing a PCR with the Q5® High-Fidelity DNA Polymerase (#M0491S, New England Biolab) with the following primers hKRAS_ex2_flank_Fw: 5`G G T A C T G G T G G A G T A T T T G A T A G T G 3`

and hKRAS_ex2_flank_Rv 5`G G T C C T G C A C C A G T A A T A T G C A 3`. The purified PCR products were sent Eurofins (Ebersberg, Germany) for sequencing. The sequencing results were analyzed via Snapgene Viewer (Version 6.0.2) and the sequences were compared with the wildtype human KRAS gene sequence to find mutations.

3.2.4. Pharmacotyping of organoids

Pharmacotyping of organoids was conducted in between passage 5-17 in organoids which could re-grew after a freeze and thaw cycle and according to the protocol recently used in the publication by Orben et al. [97]. To perform pharmacotyping, the organoids were embedded in 50 µl of Matrigel and cultured with 500 µl of PDO culture media (DMEM-F12 (#11320033, Thermo Fisher), 5mg/ml D-Glucose (#G8270, Sigma-Aldrich), 0.5% ITS Premix (#354350, Fisher Scientific), 5 nM 3,3,5-Triiodo-L-Thyronine (#T0821, Sigma Aldrich), 1 µM Dexamethason (#D1756, Sigma Aldrich), 100 ng/ml Cholera Toxin (#C9903, Sigma Aldrich), 1% Pen-Strep (Thermo Fisher), 5% NU-Serum IV (#355500, Fisher Scientific), 25 µg/ml Bovine Pituitary Extract (#P1167, Sigma Aldrich), 10 mM Nicotinamide (#N3376, Sigma Aldrich), 100 µg/ml Primocin (#ant-pm05, Invivogen), 0.5 µm A83-01 (#2939, Tocris), 10% RSPO1-conditioned medium Primocin (#ant-pm05, Invivogen), 0.5 µm A83-01 (#2939, Tocris), 10% RSPO1-conditioned medium (R-spondin-1 overexpressing cell line HEK293FT, provided by the Hubrecht Institute (Uppsalalaan 8, 3584 CT Utrecht, Netherlands), 100 ng/ml Recombinant Human Heregulin-1 (#100-03, Peprotech)) in a 24-well plate. The media in the 24-well plates with the organoids was aspirated and 250 µl of Cell Recovery Solution ((#11543560, Fisher Scientific) was added to each well with organoids. Afterwards, 1 ml of ice-cold PBS w/o Ca^{2+} w/o Mg^{2+} (Sigma Life Sciences), supplemented with 0.1% BSA (Serva, Heidelberg, Germany) was added to each well and the mixture was resuspended by pipetting up and down with a p1000 pipette. The Liquid was transferred into a 15-ml falcon tube and centrifuged at 1000 rpm at 4°C for 5 min. After the centrifugation, the supernatant was aspirated, and 2 ml ice-cold PBS was added to the organoid cell pellet. The cell pellet was now resuspended in the PBS and then, 6 ml of ice-cold PBS was additionally added to the falcon and then centrifuged at 1000 rpm at 4°C for 5 min. After centrifugation, the supernatant was again aspirated to resuspend the cell pellet with the freshly added 1 ml of TrypLE. Subsequently, the falcon was

incubated at 37°C for 1 min. To stop further digestion, 7 ml of warm DMEM-F12 were added and the falcon tube was centrifuged at 1000 rpm at 4°C for 5 min. After aspiration of the supernatant, the cell pellet was resuspended in 1 ml of warm PDO culture Media supplemented with 10 µM Rho Kinase Inhibitor (#TB1254-GMP, Y-27632, Tocris).

After all these steps, the organoid cells were now present as single cells and were counted in a disposable Hemocytometer (#MDH-2N1-50PK, Merck, Germany). After counting, Tthe cells were diluted to get a final cell concentration of 500 cells/well in 20 µl drug screen solution (2 µl Matrigel + 18 µl medium growth medium + 10 µM Y-27632). The pharmacotyping of the diluted cells was performed in a 384-well plate, therefore, 20 µl of the diluted cell solution was added in each well (#CLS3765, Corning Life Sciences). To prevent evaporation 50 µL of PBS was added to all empty wells on the 384-well plate and then, the plate was centrifuged for 10 seconds at 500 rpm. After the centrifugation, the plate was placed at 37°C and 5% CO_2. The drugs were added after 24 hours of incubation to each well which contained organoids. The drugs were diluted, so that 4 µl could be added to reach the appropriate concentration. For the control wells and the single treatment wells, 8 µl and 4 µl of PDO Medium with DMSO were added, respectively. For the combination treatment, 4 µl of each drug were added. The plate was then centrifuged for 5 seconds at 500 rpm and incubated at 37°C and 5% CO_2 till the treatment ends. After a treatment period of three to six days (depending on the drugs), 5 µl CellTiter-Glo® Luminescent Cell Viability reagent (#G7573, Promega, Fitchburg, Wisconsin, USA) was added to each well. After 10 minutes of gentle shaking at 300 rpm and 20 minutes of incubation at room temperature, luminescence was measured with a FLUOstar OPTIMA microplate reader (BMG Labtech GmbH).

3.2.5. Long-term treatment of organoids

Organoids were seeded in a dome of 50 µl Matrigel. One well per concentration was seeded in a 24-well plate. The cell number was tested for each line individually but was between 25.000 – 50.000 cells per well. On the next day, 20 nM JNJ-64619178 or DMSO as vehicle-control were added in 100 µl PDO-medium. The medium was changed after additional 6 days and drugs were added freshly afterwards. To end the experiment, 125 µl CellTiter-Glo® was added to each well after 14 days. After

15 minutes, the plate was placed on a shaker and was shaken shortly at 450 rpm and then incubated at room temperature. After 20 minutes, the supernatant was transferred into 3 wells of a clear-bottom 96-well plate (#3610, Corning Life Sciences, New York, USA). Luminescence was measured on a FLUOstar OPTIMA microplate reader (BMG Labtech GmbH).

3.3. Human patient derived PDAC 2D lines

The human patient derived PDAC 2D cell lines were established and analyzed in accordance with the declaration of Helsinki and were approved by the local ethical committee TUM, Klinikum rechts der Isar (330/19S, 5542/12). Written informed consent from the patients for research use was obtained before the investigation.
Generation and propagation of human primary 2D cell lines were conducted as described by Conradt and colleagues [93]. The lines PACADD-119, PACADD-135, PACADD-137, PACADD-159, PACADD-161, and PACADD-165 were purchased from the Leibniz Institute DSMZ – German Collection of Microorganisms and Cell Cultures GmbH (Braunschweig, Germany). The human primary 2D lines were cultured in RPMI GlutaMAX® (#61870036, Life Technologies, Darmstadt, Germany) supplemented with 20% FCS and 1% Penicillin-Streptomycin (Merck, Sigma-Aldrich, Darmstadt, Germany) or Advanced DMEM (#12491023, Life Technologies, Darmstadt, Germany) + 20% FCS and 1% Penicillin-Streptomycin (Merck, Sigma-Aldrich, Darmstadt, Germany) according to table 9. For all experiments, the cell lines were used in-between passages 13-40.

3.4. Viability assay

The viability assays were performed on white, clear-bottom 96-well plates (#3610, Corning Life Sciences, New York, USA) by seeding 500 – 1,000 cells per well for a six days treatment or 1,000 – 2,000 cells per well for a treatment duration of three days (the accurate cell number depends on the cell line). Seeding was performed in 100µl of the cell line specific media indicated in table 9.
On the next day, the drugs were added in 20 µl medium, and the plate was placed back in the incubator at 37°C. To end the treatment, the plate was removed from the incubator to equilibrate to RT. Then, 25 µl CellTiter-Glo® reagent (Promega, #G7573) (buffer and substrate mixed 1:1) were added to each well. After 10 minutes

of gentle shaking at 300 rpm and 20 minutes of incubation at room temperature protected from light, luminescence was measured on a FLUOstar OPTIMA microplate reader with a gain of 1500 (BMG Labtech GmbH, Ortenberg, Germany).

3.5. GI_{50} and AUC calculations, Synergy ZIP-score calculation

The area-under-the-curve (AUC) and the half-maximal growth inhibitory (GI_{50}) concentration values (non-linear regression model) were calculated with GraphPad Prism 5 (RRID:SCR_002798, GraphPad Software, California, USA). The Synergyfinder platform (https://synergyfinder.fimm.fi) was used to determine synergism between the drugs. By using the synergyfinder platform, a Zero interaction potency (ZIP) model was applied to a dose-response matrix. The chosen readout was “viability” with the LL4 curve fitting and the ZIP method. All the following options were switched to “ON”: “Visualize dose-response data”, “Calculate synergy”, “Correction”, “Detect outliers”, and “Visualize synergy scores”.

3.6. Clonogenic assay

For the clonogenic assay, 1,000 – 4,000 cells (depending on the cell line) were seeded in 500 µl medium in 24-well plates. On the next day, the drugs were added in different concentrations in 50 µl of medium followed by culturing for one week in an incubator at 37°C and 5% CO_2. Subsequently, the medium was aspirated, and cells were washed with PBS. After the washing step, the cell colonies were stained with Crystal Violet (Sigma-Aldrich, Darmstadt, Germany) solution (2.5% (v/v) EtOH and 4% (w/v) Crystal Violet in H_2O) for 30 minutes on a shaker at RT. Afterwards, the wells were washed 3 times with tap water to remove crystal violet from the plastic and then dried at least overnight. Visualization of the stained colonies was performed by using a photo scanner (Seiko Epson K.K., Suwa, Nagano, Japan).

3.7. Western blotting

For the protein isolation, cells were seeded in 5ml of their respective medium in 10 cm cell culture dishes. On the next day, the cells were treated with the indicated drugs. For determination of basal protein expression, cells were harvested at 80% confluency. For preparing the whole cell lysates, dishes were put on ice, the medium

was removed, and cells were washed two times with PBS. For determination of apoptosis markers, the supernatant was included by transferring the supernatant in a falcon tube. After the washing steps, the PBS was aspirated and 100 µl of RIPA lysis buffer supplemented with protease inhibitor and phosphatase inhibitor was added to the dishes. The cells were harvested by using a cell scraper and detaching the cells by scratching them from the plate. Afterwards, the RIPA buffer with the cells was transferred in an Eppendorf tube and the cells were lysed by incubation for ten minutes on ice. To remove cell debris, the samples were centrifuged for 10 min at 14,000 x g at 4°C. The supernatant, which contained the proteins, was collected in a new 1.5 ml Eppendorf tube and subsequently frozen at -80°C. Protein concentration was analyzed via the Bradford assay. Therefore, the samples were diluted in 5x Laemmli buffer and heated for 5 minutes at 95°C. Protein samples were loaded onto 7.5% - 15% polyacrylamide gels and separated using SDS-page gel electrophoresis at 80 – 100 V for 2 – 3 hours in running buffer. Afterwards, the proteins were transferred onto a nitrocellulose membrane using the Bio-Rad wet blot system with transfer buffer at 350 mA for 1.5 hours. The membranes were blocked for 45 min in 5% (w/v) skim milk in PBS on a shaker at room temperature and incubated overnight at 4°C with a primary antibody. On the next day, the membranes were washed three times with PBS supplemented with 0.1% Tween® 20 (PBS-T). After removing the PBS, a corresponding secondary antibody diluted in 5% skim milk in PBS was incubated with the membranes for 1 hour at room temperature. Finally, the secondary antibody was removed, and the membranes were washed again three times in PBS-T. Subsequently, the blots were visualized using an Odyssey® Infrared Imaging System. Quantification of the protein bands was performed by using the Image Studio Lite Software. Protein expression values were normalized to the expression of the housekeeping protein β-Actin. The final expression values were calculated out of 3 biological replicates.

3.8. Proteomics

3.8.1. Protein digestion and peptide desalting

Proteomics was performed as described in the recent publication by Orben et al. [97]. The protocol from the publication is repeated in the following. The cells were washed with PBS twice and then lysed with lysis buffer (2% SDS and 40 mM Tris-HCl). Afterwards, the cell lysate was heated at 95°C for 5 min. After heating, cells were

removed from the heating block and TFA was added to the cell lysate with a final concentration of 1% and incubated for 2 min. Afterwards, the pH value was adjusted to about 7.5 by adding 40% NMM solution. The protein concentration was measured by BCA method.

Protein digestion was performed following the single-pot solid-phase-enhanced sample preparation (SP3) protocol. First, adding dithiothreitol (DTT) reduced the disulfide bridge, and cysteines were alkylated with chloroacetamide (CAA) for 0.5h at 37 °C in the dark. Then, trypsin was added to the digestion buffer at an enzyme:protein ratio of 3:100 (w/w), and the digestion was performed overnight at 37 °C in a Thermo-Mixer at 1,000 rpm. On the next day, FA with a final concentration of 1% was added to the samples. The samples were desalted using the Oasis HLB 96-well Elution Plate (Waters, 30 µm). Peptides were eluted from HLB plate with a solution consisting of 70% ACNand0.1% FA solution. The elutes were frozen and dried in a SpeedVac centrifuge.

3.8.2. Off-line peptides fractionation

As a next step, the basic reverse phase fractionation was done with the reverse phase (RP-S) cartridges and the AssayMAP Bravo platform (Agilent Technologies). The cartridges were primed sequentially with 150 ul isopropanocan and solvent B which consists of80% acetronnitrile (ACN), 10 mM NH4FA in water, pH=10.0. The priming was done with a flow rate of 50 µl/min. Afterwards, the cartridges were washed with 100 µl of solvent A (25 mM NH4FA in water, pH=10.0) with a flow rate of 10 µl/min. To dissolve the peptides, a 100 µl of solvent A were used and loaded onto the cartridges with a flow rate of 5 µl/min. The flow-through (FT) was collected. The cartridges were washed with 50 µl of solvent A, the washing solution was collected in the flow-through. The peptide was eluted with 25 mM NH4FA (pH = 10.0) and had a gradual increase in ACN (5%, 10%, 15%, 20%, 25%, 30%, 80%). Finally, seven fractions with flow-through were combined into four fractions (5% + 25%, 10% + 30%, 15% + 80%, 20% + FT).

3.8.3. LC-MS/MS analysis

The Microflow LC-MS/MS system was set up with a modified vanish pump combined with a Q Exactive HF-X (Thermo Fisher Scientific) mass spectrometer. The dissolving of the peptides was done in 20 µl of 0.1% FA solution. 15 µl of the sample

were injected onto an Acclaim PepMap100 C18 column (Thermo Fisher Scientific, 2 µm, 1 mm ID x 150 mm, Cat. No. 164711) using solvent A (0.1% FA in water, 3% DMSO). The samples were separated by using a linear gradient of 3% - 28% solvent B (0.1% FA, 3% DMSO in acetonitrile) at a flow rate of 50 µl/min for 60 minutes.

3.8.4. Data processing and analysis

The raw MS data files were processed with MaxQuant v1.6.2.34 and compared against the human protein database, which contains 20,230 entries (downloaded 06/2017). The default MaxQuant parameters were used. Label-free quantification and match-between-run matching function was enabled. The result was further processed with Perseus v1.6.15.0. The intensity of all protein groups was uploaded to Perseus. The potential contaminates and reverse proteins were removed. A two samples t-test was used to compare the drug sensitive cell lines (lowest quartile (n=6) versus drug resistant cell lines (highest quartile (n=6. All significantly upregulated proteins were analyzed with the Enrichr web tool.

3.9. RNAseq

RNAseq was performed as described in the recent publication by Orben et al. [97]. The protocol from the publication is repeated in the following. To isolate the total RNA, the Maxwell® 16 LEV simply RNA Purification Kit and the RNeasy Mini Kit were used according to the manufacturer's instructions. In the final step, RNA was eluted into RNase-free water, which was provided by the kit, and subsequently, concentration was measured via a NanoDrop.

RNA sequencing was performed at the Sequencing Core Unit of the TranslaTUM, Technical University Munich (TUM). Preparation of the library for bulk-sequencing of poly(A)-RNA was done as described [94]. Briefly, the barcoded cDNA of each sample was generated with a Maxima RT polymerase (Thermo Fisher) using oligo-dT primer containing barcodes, unique molecular identifiers (UMIs) and an adaptor. Via a template switch oligo (TSO), the ends of the cDNA were extended. The full-length cDNA was amplified with primers binding to the TSO-site and the adaptor. The cDNA was fragmented with the NEB UltraII FS kit. After end repair and A-tailing a TruSeq adapter was ligated, and 3'-end-fragments were amplified by using primers with Illumina P5 and P7 overhangs. In comparison to Parekh et al. [94], the

P5 and P7 sites were exchanged to allow sequencing of the cDNA in read1 and barcodes and UMIs in read2 to achieve a better cluster recognition. Sequencing of the library was performed on a NextSeq 500 (Illumina) with 67 cycles for the cDNA in read1 and 16 cycles for the barcodes and UMIs in read2. By using the published Drop-seq pipeline (v1.0) to generate sample- and gene-wise UMI tables, the data was processed [95]. Reference genome (GRCm38 or GRCh38) was used for alignment. Transcript and gene definitions were used according to the GENCODE Version M25. RNA-seq analysis was performed with R-Studio (R version 4.0.2 (2020-06-22), open-source license) and DEseq2. Genes with sum (read counts) < 5 were removed and the remaining counts were normalized and transformed using regularized log transformation (rlog) implemented in the DEseq2 package. GSEA was performed by using the rlog normalized matrix was with the GeneTrail 3.0 web tool with default setting. To find pathways which are associated with sensitive and resistant PDOs, the GI_{50} values of the JNJ-64619178 treated organoid lines were separated into quartiles and differentially expressed genes (most sensitive (n=6) versus least sensitive quartile (n=6)) were calculated using the DEseq2 package. To find pathways associated with the $FKBP12^{F36V}$-Myc fusion protein, four biological replicates of MW1955-empty-dTAG and MW1955-Myc-dTAG were compared and differential expressed genes were calculated using the DEseq2 package. The CRISPR-cell lines were compared the same way as the dTAG-models, but only out of three biological replicates. Briefly, replicates were collapsed and genes with sum (read counts) < n (number of Samples) were removed. The remaining counts were used to calculate differential expressed genes using LFC-shrink and apeglm.

The log fold change was used as a rank to perform a pre-ranked GSEA via the GeneTrail 3.0 web tool. Expression datasets for JNJ-64619178 HPAC-MYC-CRISPRa can be accessed via ENA: PRJEB43040.

The correlation between the GI_{50} values of the PRMT5i treated PDOs and the gene expression based on RNA-seq was performed as followed: the gene expression values (rlog transformed matrix) and the IC50 values of the human Organoids were correlated by pearson correlation in RStudio (Version 1.4.1717) using the function rcorr of the package Hmisc (Version 4.6-0) (https://CRAN.R-project.org/package=Hmisc).

3.10. CRISPR activation (CRISPRa) / CRISPR interference (CRISPRi)

3.10.1. sgRNA cloning

Oligonucleotides specific to the target sequence can be found in table 5. For the single guide RNA (sgRNA) cloning, the primers were first annealed by adding 1 µl of the forward and reverse Primer (100 µM), 1 µl 10x T4 DNA Ligase Buffer, and 7 ul H_2O together in a 1.5 ml Eppendorf Tube. After heating the solution for 5 minutes at 95°C on a heating block, the vial was removed and slowly cooled down for 30 minutes at room temperature. Subsequent cloning was performed with a 1:50 dilution of the annealed primers. The MYC-CRISPRa-oligos were cloned into the vector lenti_sgRNA(MS2)_zeo backbone (RRID:Addgene_61427) and the PRMT5-CRISPRi-oligos were cloned into the lentiGuide-Puro vector (RRID:Addgene_52963). The cloning was performed by adding the following components together in an Eppendorf tube: 1 µl vector (90 ng/µl), 1 µl annealed & diluted oligonucleotide, 2 µl 10x T4 DNA-Ligase Buffer, 1 µl T4 DNA Ligase, 1 µl BsmBI restriction enzyme and 14 µl H_2O. The mixture was incubated in a thermocycler with the following program: 10 cycles of (37°C for 5 minutes, 16°C for 10 minutes), 55°C for 5 minutes, 80°C for 5 minutes.

Vectors were transformed into *E.coli Stbl3* bacteria and selected on LB-Agar plates with 100 µg/ml Ampicillin. The next day, single bacteria colonies were picked from the LB-Agar plate and amplified in LB-Medium supplemented with 100 µg/ml of Ampicillin. The plasmid was extracted and isolated from the bacteria with the NucleoSpin Plasmid, Mini Kit for Plasmid DNA according to the manufacture's protocol. The successful insertion of the vectors inside the plasmids was tested by sanger sequencing.

3.10.2. Lentivirus cell production

For the lentivirus cell production, $1x10^6$ HEK293FT cells (RRID:CVCL_6911) were seeded in a 10 cm dish in DMEM + 10% FBS. The next day, the medium was removed, and fresh medium was added. In addition, 10 µl of a Plasmid mix (1.25µg psPAX2, 0.75 µg pMD2, and 2 µg of the lenti-vector, filled to 10 µl with H_2O) and

the transfection mix (18 µl Lipofectamin, 280 µl Optimem) were mixed. After an incubation for 5 minutes at room temperature it was added dropwise to the medium. On the next day, the medium was aspirated and new DMEM + 30% FBS was added. On the following day, the medium was again aspirated and collected in a 15 ml Falcon tube. DMEM + 30% FBS was then added to the plate. On the last day, the medium was aspirated and pooled with the medium from the previous day, filtered, and the lentivirus-containing medium was stored at -80°C.

3.10.3. Lentiviral cell transduction

For the lentiviral cell transduction, 100,000 – 150,000 HEK293FT cells were seeded in two wells of a 6-well plate for 24 hours. 1 ml of the lentivirus containing medium was added to the cells together with 8 µg/ml Polybrene. After 8 hours, 1 ml of DMEM with 10% FBS was added, and the plates were cultured overnight at 37°C and 5% CO_2. On the next day, the medium was refreshed. On the following day, a selection reagent specific to the inserted vector was added to the cells. The concentration of the respective reagents was as followed: 2 µg/ml Puromycin, 300 µg/ml zeocin, 400 µg/ml Geneticin, and 800 µg/ml Hygromycin B. The cell line PaTu8988T PRMT5-CRISPRi was transduced with plenti_dCas9-KRAB-MeCP2 (RRID: Addgene_122205) and plentiGuide-Puro-sgRNA-PRMT5 (Addgene: #164637). The cell line HPAC-MYC-CRISPRa was transduced with plenti-dCAS-VP64_Blast (RRID:Addgene_61425), plenti_MS2-P65-HSF1_Hygro (RRID:Addgene_61426) and plenti_sgRNA(MS2)_zeo_sgRNA-MYC (Addgene: #164636).

3.11. Seahorse analysis – Mito- and Glyco-stress test

The Seahorse assay was performed by seeding 1000 – 2000 cells per well in quadruplets in 80 ul of the respective cell line medium with 10% FCS in a Seahorse cell culture plate. The wells at the four edges were left empty. For normalization at the later analysis, a 96 well plate was prepared the same way and all steps were performed the same way to measure Hoechst staining. On the next day, 20 nM JNJ-64619178 or DMSO for the control wells were added in 20 µl of medium. One day prior to the final measurement, the cartridge was hydrated by adding 200 µl H_2O to each well. Furthermore, the RPMI and DMEM Seahorse medium was prepared by adding 2 mM Glutamine and 1 mM Pyruvate and adjusting the pH to 7.4. For the

Mito Stress test, 25 mM D-glucose was added in addition to the others. The cartridge and the calibration solution were incubated overnight at 37°C and 0% CO_2.
The measurement was performed 72 h after adding the drugs. The medium in the Seahorse plate was changed to 180 µl Seahorse medium one hour before the measurement. The H_2O in the cartridge was changed to 200 µl of prewarmed calibration solution. Both plates were incubated for 1 hour at 37°C and 0% CO_2. The loading of the Seahorse plate ports was as followed: For the mito stress test: Port A) 20 µl of 20 µg/ml Oligomycin; Port B) 22 µl of 10 uM FCCP and 50 mM Pyruvat; Port C) 25 µl of 25 µM Rotenon and 25 µM Antimycin-A. The ports for the glycol stress test were loaded as followed: Port A) 20 µl of 100 mM Glucose; Port B) 22 µl of 20 ug/ml Oligomycin; Port C) 25 µl of 1 mM 2-desoxy-D-glucose. Analysis of the Seahorse plate was done in a Seahorse XFe96 Analyzer. The cells in the parallelly prepared 96-well plate were stained with 25 µl of 25 µM Hoechst-Staining and measured on a FLUOstar OPTIMA microplate reader with a gain of 1500 (BMG Labtech GmbH, Ortenberg, Germany). The ECAR and OCR values were calculated in relation to the cells with Hoechst-Staining to compensate for cell density. Calculation of the different parameters was done as described by the manufacturer (Download available at www.agilent.com).

3.12. Glucose uptake assay

To conduct the glucose uptake assay, 1000 – 2000 cells per well were seeded in 100 µl of the respective cell line medium with 10% FCS in white, clear-bottom 96-well plates (#3610, Corning Life Sciences, New York, USA). The next day, 20 µl of medium were added with JNJ-64619178 to receive a final concentration of 20 nM in the medium. The glucose uptake was measured after 72 hours of treatment, according to the Glucose Uptake Glo assay from Promega. First, the 2-deoxyglucose-6-phosphate (2DG6P) reagent was made by mixing the following components: 100 µl luciferase reagent, 0.5 µl reductase, 1 µl $NADP^+$ (20 mM), 2.5 µl Glucose-6-Phosphate Dehydrogenase (G6PDH) and 0.0625 µl reductase substrate. The 2DG6P reagent was then incubated for 1 hour at room temperature. During the incubation time, the cells in the plate were washed with 100 µl PBS after the medium of the wells was aspirated. Afterwards, 50 µl of 1 mM 2-deoxyglucose (2DG) was added to each well, briefly shaken, and incubated for 10 minutes. After adding 25 µl Stop buffer and gentle shaking for 5 seconds, 25 µl of Neutralization

buffer were added. Finally, 100 µl of the before-prepared 2DG6P reagent was added to each well and after 1 hour of incubation at room temperature, Glucose uptake was measured on a FLUOstar OPTIMA microplate reader with a gain of 1500 (BMG Labtech GmbH, Ortenberg, Germany).

3.13. Dataset analysis from cBioPortal and depmap portal

To analyze the link between gene expression and the survival of the patient, the publicly available datasets from the website cBioPortal were used. Accurately, the datasets for pancreatic adenocarcinoma from “TCGA, Firehose Legacy” and “TCGA, PanCancer Atlas” were used for the analysis. The 396 samples from the two datasets were queried by the gene *MYC*. The probability of overall survival between the cohorts with altered and unaltered protein expression was compared by a Kaplan-Meier curve.

To analyze the correlation of different genes to each other in different tumor entities, the publicly available dataset “Expression 21Q3 Public” from the website depmap portal was used. The correlation was performed between the indicated genes on the figures. The visualization of the data was performed either on R-studio with the ggplot package or on Graph-Pad Prism.

3.14. Statistics

All Experiments were conducted in the indicated number of biological replicates. The standard deviation is depicted as error bars. Statistical significance was investigated via the two-sided Student`s t-test. p-values were calculated with GraphPad Prism5 (RRID:SCR_002798, GraphPad Software, California, USA). For figures in which controls were normalized to 1, statistical testing was performed on non-normalized data taking the variation of controls into account. p-values are indicated by the respective number or asterisk (* = $p<0.05$, **= $p<0.01$). P values < 0.05 were considered as significant.

4. Results

4.1. Connection of *MYC* and *PRMT5* expression to survival

A recent study shows that PDAC patients with a high expression of the oncogene *MYC*, are linked to a worse survival outcome compared to patients with a normal *MYC* expression [96]. To confirm this, the publicly available expression datasets from cBioPortal were analyzed. In the analyzed studies, 369 patients were included with 46 patients having an altered *MYC* expression level. Strikingly, the patients with altered *MYC* expression had a significantly reduced overall survival of only 12.03 months compared to the control group with 20.83 months (Fig. 3A), pointing to an urgent need to find new treatment options for these patients. To unbiasedly define MYC-associated epigenetic vulnerabilities, a drug screen with an epigenetic drug library of cell lines with basal and deregulated MYC activity was performed in the Schneider laboratory (Technical University Munich, Klinikum rechts der Isar). The PRMT5 inhibitor GSK591 was defined as a novel hit to have increased activity in cells with a deregulated *MYC* expression [97]. To further elaborate on the importance of *PRMT5* in the context of MYC activity, the connection between the two genes was investigated. A significant positive correlation of *PRMT5* and *MYC* gene expression with a Pearson r-value of 0.65 was observed when analyzing conventional human PDAC cell lines from the dataset “Expression 21Q3 Public” on depmap portal (Fig. 3B). The analysis of the correlation of *MYC* and *PRMT5* across different tumor entities revealed that the highest correlation coefficient was detected in PDAC (Fig. 3C). The correlation coefficient for all tumor entities is listed in STable 1.

In a recent publication, the group of Mathew J. Garnett performed a CRISPR/Cas9 drop-out screen for different cancer types and genes [98]. The data of the screen revealed that 98% of the PDAC cell lines have significantly impaired fitness after genetic inactivation of *PRMT5* with an overall Loss of Fitness score below the mean of tested tumor entities. Moreover, impaired fitness could be observed across all 17 tested tissue types (Fig. 3D).

This corroborates that PRMT5 is a relevant therapeutic target in the context of PDAC and the expression of *PRMT5* correlates with the expression of *MYC* in different tumor entities and especially in PDAC.

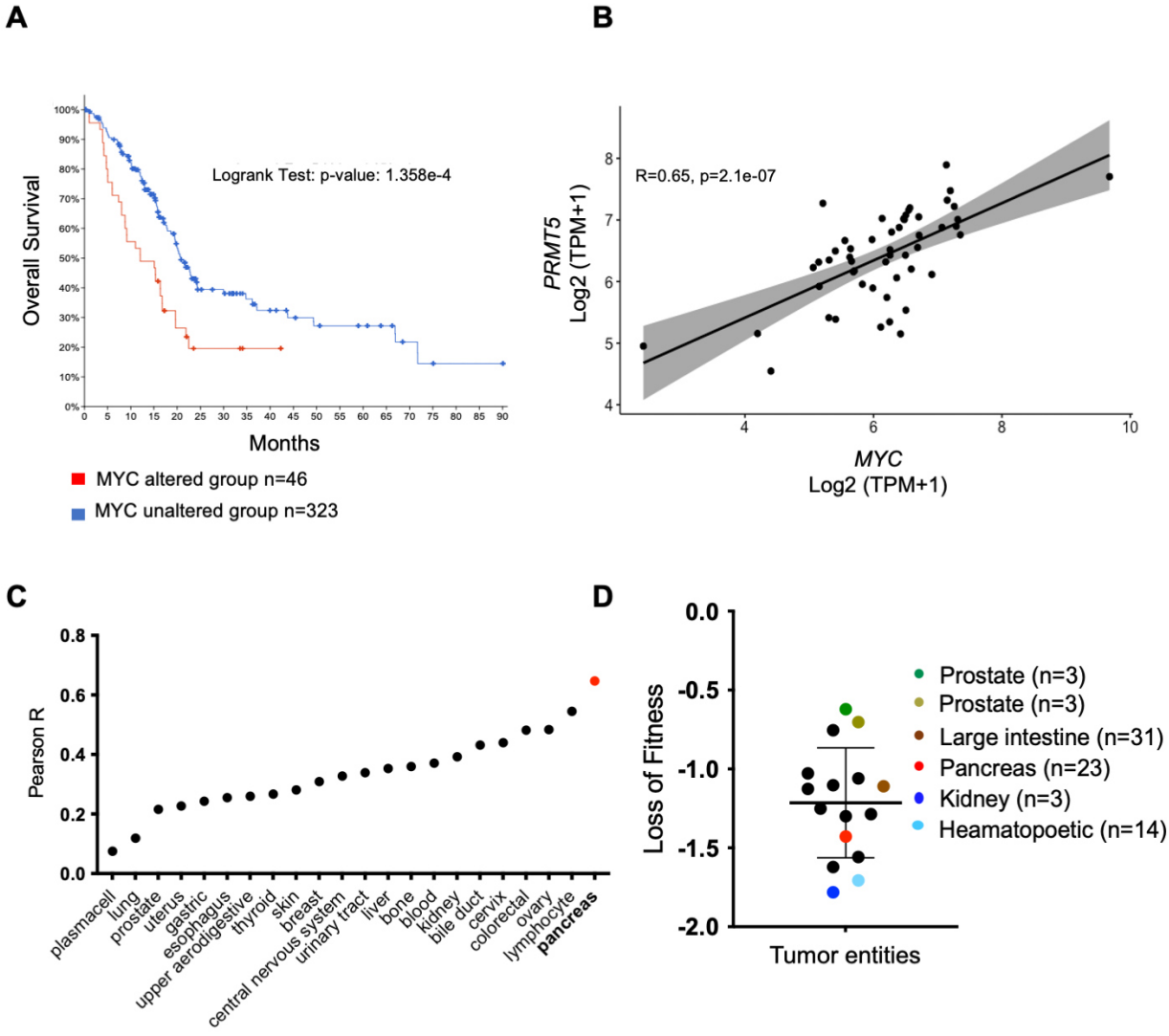

Figure 3: Connection of *MYC* and *PRMT5* across tumor entities

A) Overall survival difference between patients suffering from PDAC with altered *MYC* expression (46 patients; median survival 12.03 months; red line) and unaltered *MYC* expression (323 patients; median survival 20.83 months; blue line). Data from combined Pancreatic Adenocarcinoma studies extracted from cBioPortal. **B)** Depicted is the Pearson correlation coefficient and the linear regression between *MYC* and *PRMT5* mRNA expression in conventional human PDAC cell lines. Data were retrieved from the DepMap portal ("Expression 21Q3 Public") and includes n=52 cell lines. The Pearson correlation coefficient r and the p-value are indicated. **C)** The Pearson correlation coefficient R between *MYC* and *PRMT5* across different tumor entities in humans is illustrated. The data was retrieved and analyzed as in B). **D)** Results of a CIRPSR drop-out screen across tumor entities after *PRMT5* inactivation. Data were retrieved from the Project Score portal. For some tumor entities, the number of included cell lines is depicted. Pancreatic cell lines (red) show a loss of fitness below the mean. A score <0 is a statistically significant effect.

4.2. Correlation of *MYC* and *PRMT5* in different cell models

To strengthen the already seen correlation between *PRMT5* and *MYC*, the correlation of the two genes was assessed in primary patient-derived organoids. A significant Pearson correlation of R=0.5 (Fig. 4A) was calculated. A similar correlation could also be observed on protein level in low passaged human 2D cell lines from PDX-mice, with a Pearson correlation of R=0.71 (Fig. 4B)

These results point to a strong correlation between *MYC* and *PRMT5* across cell models.

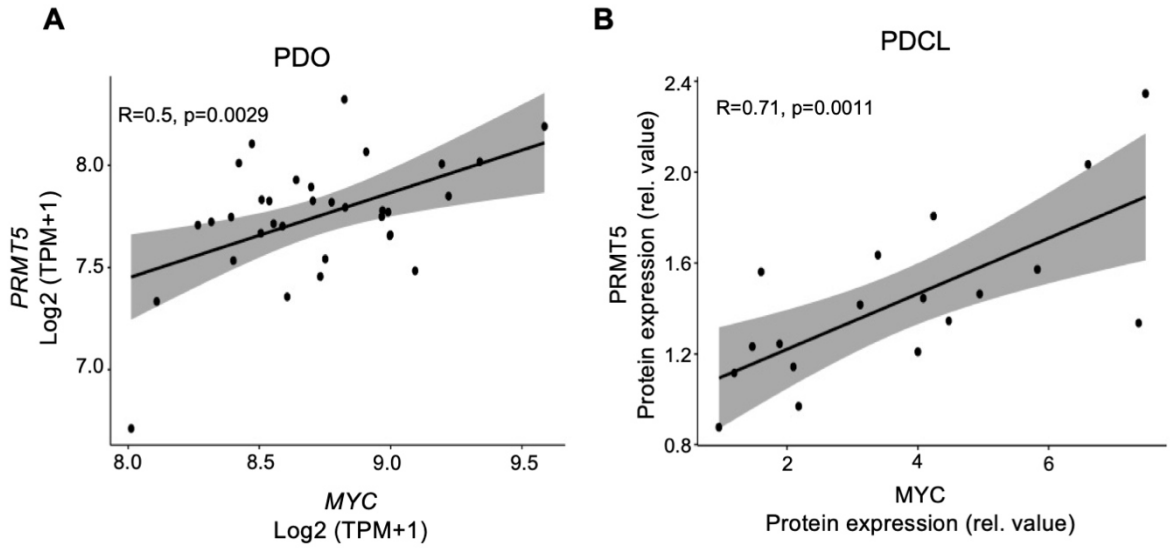

Figure 4: Correlation of *PRMT5* and *MYC* in patient-derived cell models

A) Depicted is the Pearson correlation coefficient and the linear regression in primary human PDAC organoids (PDO, n=33) between *MYC* and *PRMT5* mRNA expression. **B)** Depicted is the Pearson correlation coefficient and the linear regression between MYC and PRMT5 protein expression in patient derived PDAC cell lines (PDCL, n=18). Protein expression was assessed via western blot and indicated in the correlation as a relative value in relation to the housekeeping protein ß-ACTIN. The Pearson correlation coefficient R and the p-value are indicated.

4.3. Bi-directional control of MYC and PRMT5

To prove a direct connection between MYC and PRMT5, cell lines with a CRISPR activation (CRISPRa) complex were used. In this system, the strong transcriptional activator VP64, which consists of four tandem copies of the protein Herpes Simplex Viral Protein 16, is fused to an inactive Cas9 (dCas9). To receive a strong upregulation of the target gene, the Synergistic Activation Modulator (SAM) was cloned into the CRISPRa cells. The SAM vector consists of three transcriptional activation modulators, namely MS2, P65, and HSF1. At last, the sgRNA with an MS2 binding site was used with an insert to specifically bind to the target site from the gene of interest [99]. The single guide RNA (sgRNA) sequences can be found in table 5. The subsequent experiments were all performed with the sgRNA Myc2, due to the most effective MYC upregulation. For the control cell lines, single guide RNAs (sgRNAs) without a target sequence were used, which is called empty guide in the following. The two human PDAC cell lines HPAC-CRISPRa and PANC-1-CRISPRa showed an upregulation of MYC protein expression, with a 3.6-fold and 3.2-fold increase, respectively (Fig. 5A, B, and SFig. 2A). In addition, PRMT5 protein expression was upregulated 1.6-fold in HPAC-CRISPRa and 1.9-fold in PANC-1-CRISPRa (Fig. 5A and SFig. 2B). To investigate the connection of *MYC* and *PRMT5* at the RNA level, RNA-seq was performed with the CRISPRa cell lines. Analyzing the RNA-seq data of the PANC-1 and HPAC CRISPRa modified cell lines with a Gene set Enrichment Analysis (GSEA) revealed a significant upregulation of the Hallmark MYC TARGETS V1 and V2 in both cell lines. Depleted hallmark signatures in both CRISPRa cell lines were epithelial to mesenchymal transition, estrogen response early, and TNF alpha signaling via NFKB (Fig. 5C). The complete gene set enrichment analysis can be found in STable 2 and STable 3. To test the connection of MYC and PRMT5 reciprocally, a cell line modulated via the use of the CRISPR interference system (CRISPRi) was designed. Therefore, Patu8988T was transduced with a vector containing an inactive Cas9 fused with the repressor domain Krüppel associated Box (KRAB) and the repressive domain methyl CpG-binding protein 2 (MeCP2) [100]. Interestingly, PaTu8898T-CRISPRi transduced with

a guide targeting the *PRMT5* gene showed reduced levels of both MYC and PRMT5 on protein level (Fig. 5A and D).

Together, these data indicate a robust and dynamic bi-directional connection between MYC and PRMT5.

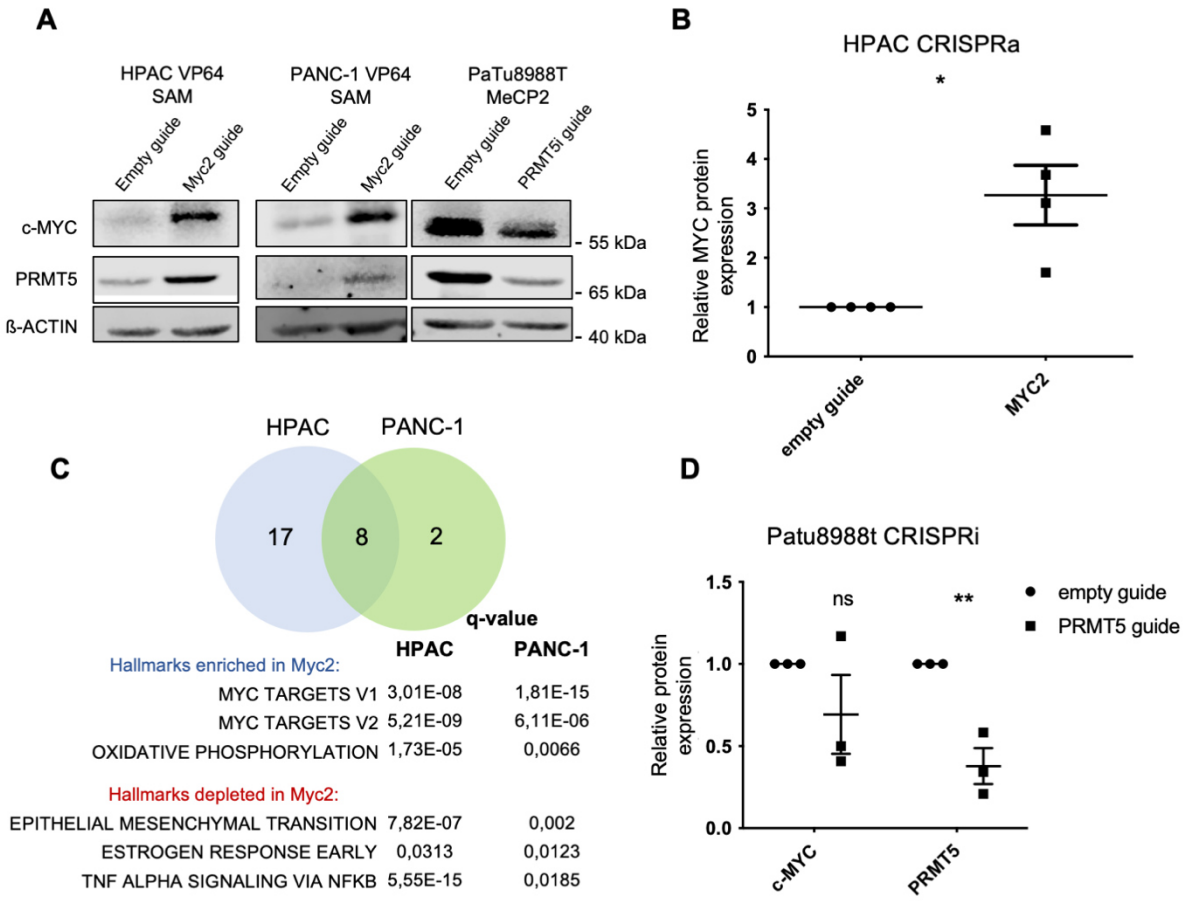

Figure 5: Characterization of CRISPR cell lines

A) MYC and PRMT5 protein expression of the CRISPR activation cell lines. ß-ACTIN served as a loading control. One representative experiment out of three (Patu8988t and PANC-1) or four (HPAC) are shown. **B)** Quantification of MYC and PRMT5 protein expression from HPAC cell lines (n=4). Protein Expression was normalized to the sgRNA empty guide. ** P-value of an unpaired t-test <0.01. **C)** RNA-seq mRNA expression between the empty guide and Myc2-guide of untreated HPAC and PANC-1 CRISPRa cells was analyzed with a GSEA and the HALLMARK signatures. The signatures modulated in both lines including their FDR q value are depicted. **D)** Quantification of MYC and PRMT5 protein expression from PaTu8988T (n=3). Protein expression was normalized to the sgRNA empty guide. * P-value of an unpaired t-test <0.01 was conducted on non-normalized data.

4.4. MYC expression controls PRMT5 inhibitor response

To further validate the results from the drug screen that the PRMT5i response is dependent on the MYC protein level, primary cell lines and cell models were treated with the PRMT5 inhibitor JNJ-64619178 in a seven-point drug dilution. The cellular ATP level as a surrogate for the drug response was measured. Primary 2D PDAC cell lines are a well-founded model to study drug responses in vitro and are characterized by a heterogenous background and genetic stability [101]. The primary human patient-derived cell lines (PDCL) show a heterogeneous treatment response, with a GI_{50} value ranging from 10 nM to 1000 nM. To investigate a potential connection between the drug response and the MYC protein expression, the cell lines were divided into two groups based on their GI_{50} value. The sensitive subgroup, consisting of cell lines with a GI_{50} value of <30 nM was compared with all other lines (Fig. 6A). The comparison shows that the PRMT5i sensitive subtype has a higher mean MYC protein expression (Fig. 6B). However, the data also show a subgroup of PRMT5 inhibitor resistant PDCLs which have a high MYC expression. To support the MYC effect in the PRMT5 inhibitor response, the MYC protein expression, determined by western blot, was correlated to the GI_{50} values, revealing a negative correlation between the two factors (Spearman r=-0.51, p=0.03) (SFig. 2C). The corresponding Western Blots can be found in SFig. 2D. This data demonstrates a connection between the MYC protein level and the drug response to the PRMT5 inhibitor in primary human cell models.

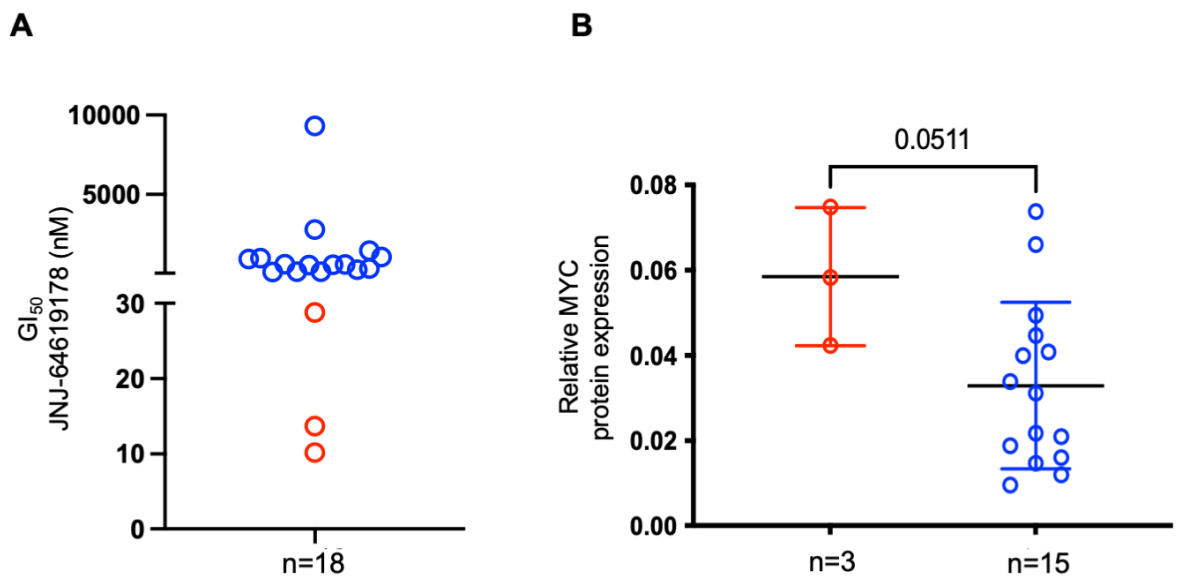

Figure 6: PRMT5i response in PDCLs

A) Viability of eighteen primary PDCLs was measured by Cell Titer Glo assay. Cells were treated for six days with JNJ-64619178. GI_{50} values were determined by analyzing three biological replicates, conducted as technical triplicates in a dosage range of 1 nm - 1000 nm. Red: sensitive lines, blue: resistant lines. **B)** MYC protein expression based on western blot analysis in PRMT5i sensitive and resistant PDCLs. The protein expression was calculated relative to the ß-actin protein expression. Shown is the mean protein expression from three replicates. P-value of an unpaired t-test is indicated.

4.5. PRMT5i response in cell lines transduced with the dTAG-MYC system

To further substantiate the role of MYC in the treatment response to PRMT5 inhibitors, *MYC* overexpression cell models were used. These overexpression models also help to cope with intertumoral heterogeneity of the drug response through direct control of the *MYC* gene expression. To create a cell model in which the *MYC* expression can be conditionally adapted, the degradation TAG system (dTAG) was used. The dTAG system is implemented into the cell, by transducing a vector that expresses a chimera protein consisting of the protein *FKBP12*^{F36V} fused to the protein of interest. This fusion protein is continuously expressed but can be degraded by adding dTAG-13. dTAG-13 consists of a cereblon-binding ligand, combined with a linker to an FKBP12^{F36V} ligand. The dTAG-13 can form a complex with the fusion protein and initiates thereby degradation of the fusion protein in the proteasome. Degradation is initiated with the help of dTAG-13, which is bridging the

fusion protein to the Cereblon E3 ligase complex to ubiquitinate the fusion protein. The *Myc* gene was fused to FKBP12^{F36V} and the fusion protein was inserted into the murine PDAC cell line MW1955, which has a Cre recombinase to delete the floxed exons 2 and 3 of the *Myc* gene [90]. In this study, this cell line is called MW1955-MYC-dTAG and expresses the endogenous *Myc* and the exogenous *Myc-FKBP12^{F36V}* fusion gene. Furthermore, an additional cell line was made by treating the cell line MW1955-MYC-dTAG with 4-hydroxytamoxifen. This treatment activates the Cre recombinase which results in a deletion of the floxed *Myc* exons. Consequently, this cell line does not express the endogenous *Myc* anymore but expresses only the exogenous *Myc-FKBP12^{F36V}* fusion gene and is called Clone 4 in this study. The PCR gel to confirm the successful deletion of endogenous *Myc* in clone 4 can be found in SFig. 3A. On the Western Blot, the band for the exogenous Myc-FKBP12^{F36V} fusion protein can be clearly distinguished from the endogenous Myc band due to its higher weight in kDa. Interestingly, the cells drastically shut down the endogenous Myc expression when producing exogenous Myc. However, the endogenous Myc protein expression increases again when the fusion protein is degraded by adding dTAG-13 (Fig. 7A). To see if the Myc fusion protein is functional, RNA-seq was performed to analyze the Hallmark gene set MYC TARGET GENES. The RNA-seq confirmed that the Myc from the fusion protein is functional due to the highly enriched HALLMARKs MYC TARGETS V1 and V2 in the cell line expressing the exogenous Myc-FKBP12^{F36V} fusion protein compared to the line expressing only the endogenous Myc protein (Fig. 7B). In addition, also the HALLMARK signatures connected to the pro-proliferative E2F-pathway and the G2/M-phase of the cell cycle were enriched, whereas HALLMARKS connected to the activation of STAT5 by IL2 and the early response to estrogen were depleted (Fig. 5B). In accordance with the results seen in the CRISPR cell lines, Prmt5 was also upregulated in the murine dTAG models when the *Myc* network was upregulated (SFig. 3B). *Myc* mRNA seemed to be downregulated in MW1955-MYC-dTAG when analyzing the rlog transformed matrix. However, the mRNA of the fusion protein *Myc-FKBP12^{F36V}* is probably not detected in the RNA-seq (SFig. 3B). RNAseq data for the knock-out clone (Clone 4) and the cells treated with dTAG-13 are not available. When treated with a seven-point drug dilution of the PRMT5i, the MYC-dTAG modified lines show a significant increase in the sensitivity compared to the control line with only the endogenous Myc protein (Fig. 7C and 7D). The mean

GI_{50} values of the respective MW1955 cell models are 426 nM for the empty-dTAG line, 34.3 for Clone 4, and 10.5 for the line MW-1955-MYC-dTAG (Fig. 7D). To investigate the reverse effect, if reducing Myc protein expression leads to resistance, 500 nM dTAG-13 in combination with the PRMT5i was given to the lines to degrade the Myc-FKBP12^{F36V} fusion protein. However, the effect was synergistic instead of making the lines more resistant (SFigure 3C and Fig. 7E). The findings observed in the CTG assay could also be confirmed in a clonogenic assay (SFig. 3C). To further examine the effect of a depletion of the fusion protein, the cells were treated with high doses of dTAG-13. The assumption was that the knockout clones without endogenous *Myc* gene will not survive if the exogenous Myc protein is completely degraded. However, high doses of dTAG-13 alone did not lead to a higher reduction of the GI_{50} value in the knockout clones compared to the cell line with endogenous and fusion Myc protein (Fig. 7F). This data shows that an upregulation of the Myc network due to the addition of the Myc-FKBP12^{F36V} fusion protein results in an increased sensitivity to PRMT5 inhibition in murine cell lines. In contrast to this, degradation of the fusion protein Myc-FKBP12^{F36V} results also in a synergistic effect in combination with the PRMT5i. Since the opposite was expected, this effect warrants further investigation, especially because the degradation of the fusion protein alone has only a mild effect on survival.

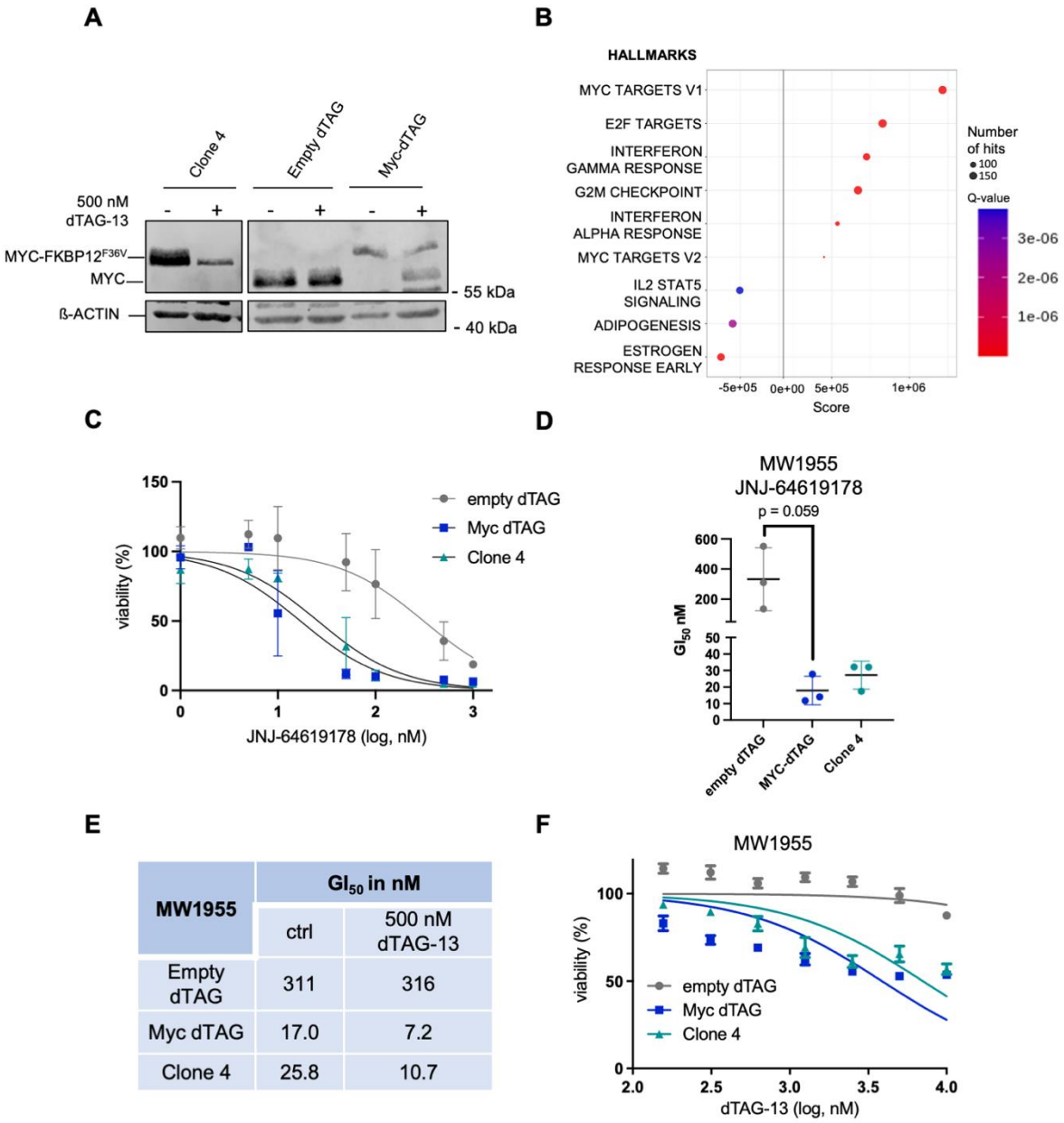

MW1955	GI_{50} in nM	
	ctrl	500 nM dTAG-13
Empty dTAG	311	316
Myc dTAG	17.0	7.2
Clone 4	25.8	10.7

Figure 7: PRMT5i response in cells transduced with the dTAG-system

A) MW1955 dTAG cell lines were treated with 500 nM dTAG-13 as indicated or were left as vehicle-treated controls for 24h. Western blotting demonstrated expression of MYC. ß-ACTIN served as loading control. One representative experiment out of 3 is shown. **B)** Differentially expressed genes measured by RNA-seq of the two cell lines MW1955 empty-dTAG and MW1955 MYC-dTAG were calculated. The log FC was used as a rank to perform a pre-ranked GSEA using the GeneTrail3 web tool. Depicted are the HALLMARK signatures with q-values <0.05. The q-value is color-coded and depicted. **C)** Dose-response curves (max. concentration of 1 µM) of indicated MW1955 cell lines after six days of treatment with JNJ-64619178. Viability was determined with Cell Titer Glo-assay. The experiment was conducted with three biological replicates. **D)** GI_{50} values of indicated MW1955 cell lines were determined as described in C). P-value of an unpaired t-test is indicated **E)** The table shows the GI_{50} values of indicated cell lines after JNJ-64619178 treatment as described in C), with and without the addition of 500 nM dTAG-13. **F)** Dose-response curves (max. concentration of 10 µM) of indicated MW1955 cell lines after three days of treatment with

dTAG-13. Viability was determined with Cell Titer Glo-assay. The experiment was conducted with three biological replicates.

4.6. Endogenous MYC regulation leads to changes in the PRMT5i drug response

In the above-described dTAG-model, an exogenous vector was used to achieve an upregulation of the MYC network. To investigate if the upregulation of the endogenous *MYC* gene has a similar effect, the CRISPR/Cas9 model was used. As in the dTAG model, the *MYC* overexpression from the endogenous *MYC* gene led to a higher sensitivity in the CTG measured drug response to JNJ-64619178, with a reduction from the GI_{50} value from 346.8 nM to 22.96 nM in the HPAC CRISPRa (Fig. 8A) and 648.2 nM to 251.7 nM in the PANC-1 CRISPRa cell line (Fig. 8B). Furthermore, the increased MYC protein expression resulted also in increased proliferation in the HPAC CRISPR cells (SFig. 4A). Direct targeting of the *MYC* gene with subsequent downregulation via dCas9 interference, and targeting *MYC* mRNA via Cas13 [102,103], were unsuccessful. Therefore, the regulation of the PRMT5i sensitivity in a loss-of-function model was addressed with the PRMT5 CRISPRi PaTu8988T cells, which downregulated the *PRMT5-MYC* module (Fig.5 C). The dose-response curve to JNJ-64619178 was right-shifted in this model with an increase of the mean GI_{50} from 184.6 nM to 512.6 nM in the lines from with the empty sgRNA compared to the *PRMT5* targeting sgRNA (Fig. 8C). The reduced PRMT5 protein expression in this model was not connected to an altered proliferation rate of the cells (SFig. 4B). The data of the CRISPR model further strengthens the conclusion that the regulation of *MYC* in human cell lines results in altered sensitivity to PRMT5 inhibition.

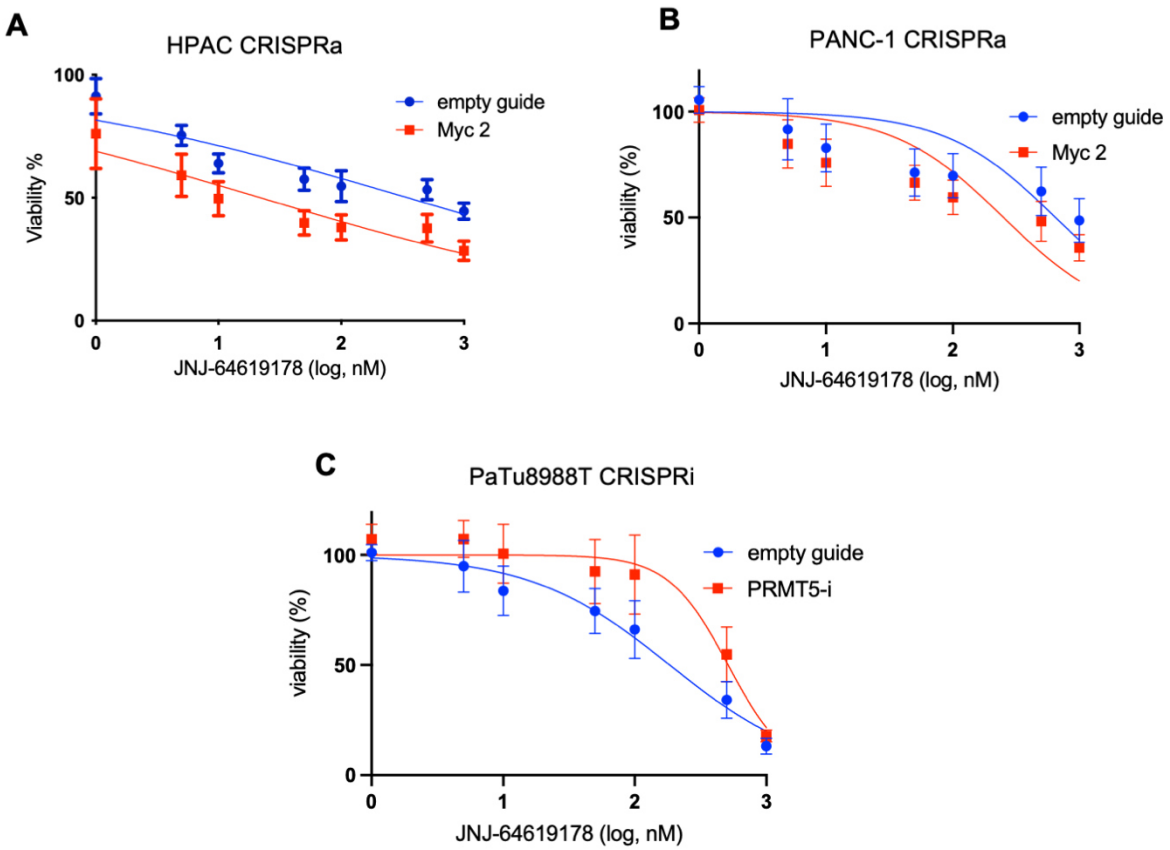

Figure 8: PRMT5i response in CRISPR cell lines

Dose-response curves (max. concentration of 1µM) of HPAC **A)**, PANC-1 **B)**, and PaTu8988T **C)** CRISPR cell lines after six days of treatment with JNJ-64619178. Viability was determined with Cell Titer Glo-assay. Cell lines with empty-guide sgRNA are marked in blue and cell lines with a guide targeting MYC (CRISPRa) and PRMT5 (CRISPRi) are marked in red. Number of biological replicates for each cell line is as followed: HPAC: n= 4; PANC-1: n= 5; PaTu8988T: n= 6.

4.7. Pharmacological loss of function by indirect targeting of MYC

In addition to the aim of developing an endogenous *MYC* knockdown via the CRISPR technology, a pharmacological loss-of-function model was employed. In this inducible approach, MYC can be targeted indirectly via a bromodomain and extra-terminal motif (BET) protein degrader ARV-771 [104] efficiently degrades BRD4 and MYC in a dose-dependent manner in DanG cells (Fig. 9A). This is consistent with the described function of BRD4 to activate *MYC* transcription to maintain homeostatic MYC protein levels [105]. At a concentration of 50 nM ARV-771, also PRMT5 protein levels are decreased to 55%, whereas MYC and BRD4 are decreased to 38% and 18%, respectively (Fig. 9A and 9B). The combination treatment with JNJ-64619178 shows that the ARV-771 mediated decrease in MYC protein levels was associated with reduced efficacy of the PRMT5 inhibitor (Fig. 9C and 9D). The area under the curve is significantly higher in the combination with 50 nM ARV-771 compared to the single treatment with JNJ-64619178 (Fig. 9D). In addition, the drug interaction was analyzed on the SynergyFinder 2.0 platform [106] with the Zero interaction potency (ZIP) model [107]. This analysis resulted in a negative overall ZIP synergy score of -16.9, which further implies an antagonistic interaction between ARV-771 and JNJ-64619178A (Fig. 9E).

Summarizing the PRMT5 inhibitor response in the different cell models it was shown that across species and models, deregulated *MYC* expression is associated with altered drug response. A high MYC protein level due to additional exogenous MYC or upregulation of endogenous MYC leads to increased sensitivity, whereas pharmacological knockdown of MYC leads to resistance.

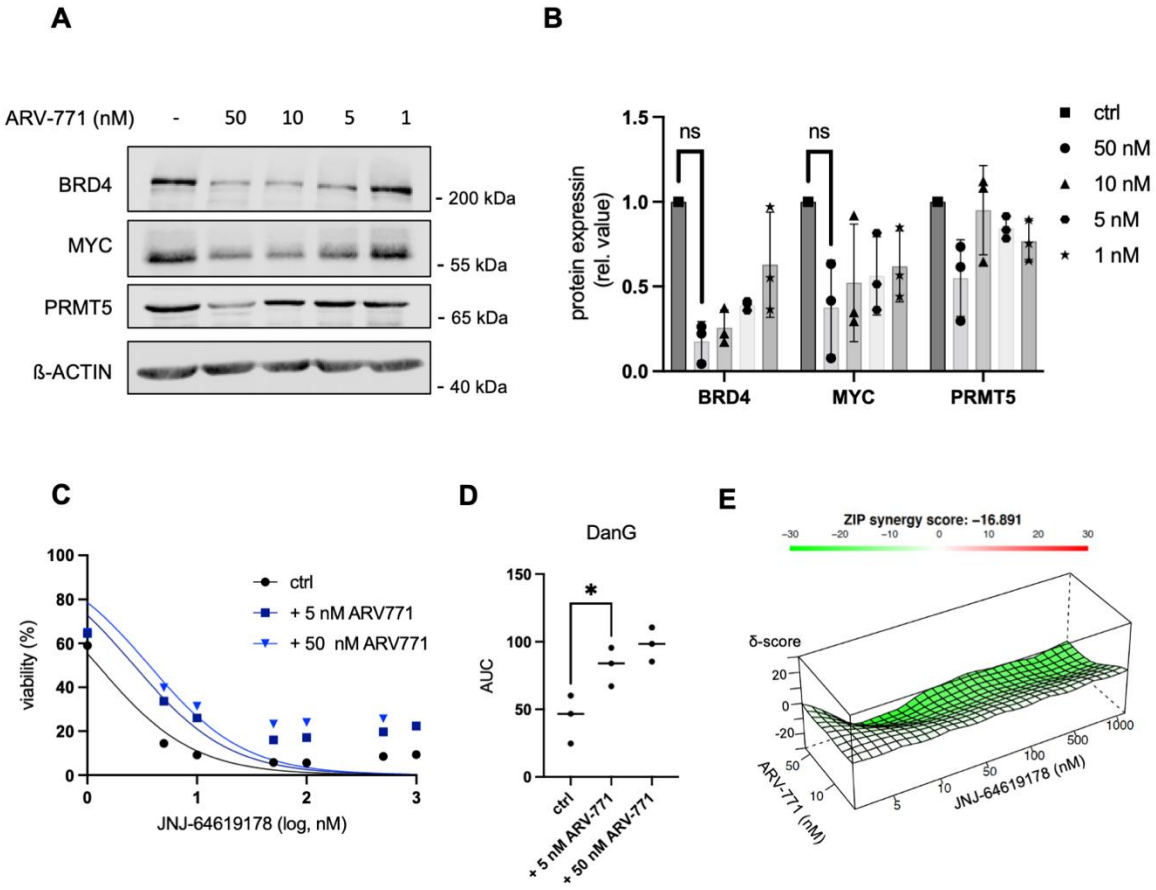

Figure 9: Pharmacological knock-down of MYC

A) DanG cells were treated with ARV-771 as indicated or were left as vehicle-treated controls for 72 hours. Western blotting demonstrated expression of BRD4, MYC, and PRMT5. ß-ACTIN served as loading control. One representative experiment out of 3 is shown. **B)** Protein expression based on western blot analysis from A) is depicted. Expression is normalized to vehicle-treated control. The Statistic was conducted as an unpaired two-sided t-test on non-normalized protein-expression data **C)** JNJ-64619178 dose-response curve of DanG cell, co-treated with vehicle control or ARV-771 as indicated. **D)** Area under the curve (AUC) values of dose-response curves from C) were determined. * p-value of unpaired t-test <0.05. **E)** Synergy map of JNJ-64619178 and ARV-771 co-treated DanG cells.

4.8. A PRMT5 inhibitor sensitive subtype in human PDAC organoids

Recent publications describe that the therapeutic profiles of patient-derived organoids paralleled patient outcomes. Therefore, patient-derived organoids (PDOs) are models which have the potential to predict the clinical behavior of PDAC in patients [108,109]. To investigate JNJ-64619178 response in this model, PDAC organoids were treated with the PRMT5i for 6 days with a nine-point drug dilution and the dose-response was measured via CTG assay. The 24 tested organoid lines showed a huge variability regarding the inhibitor response. Whereas the five most sensitive of them showed GI_{50} values in a single-digit nanomolar range, 7 lines showed a GI_{50} value of >500 nM (Fig. 10A). Overall, a PRMT5i sensitive subtype could be detected in the PDO model (Fig. 10A). The dose-response curves of three resistant and three sensitive organoid lines are depicted in Figure 10B. Investigation of selected organoids via western blot revealed, that the highest MYC protein expression belongs to one of the PRMT5 inhibitor sensitive organoid lines (Fig. 10C). However, the existence of PRMT5i resistant lines with high MYC protein expression could also be detected. To cope with different proliferation capabilities and to investigate the effect of a long-term exposure to a PRMT5 inhibitor, organoid cell lines were treated for two weeks with JNJ-64619178. The difference between the PRMT5 inhibitor sensitive and the resistant subgroups remained even after this prolonged treatment (Fig. 10D). In addition, also the morphological changes of the organoids due to PRMT5 inhibitor treatment were investigated. Organoids exposed to JNJ-64619178 had reduced growth and had a smaller, irregularly shaped morphology (Fig. 10E). This data demonstrates the existence of a highly PRMT5i responsive subtype also in a primary patient-derived model.

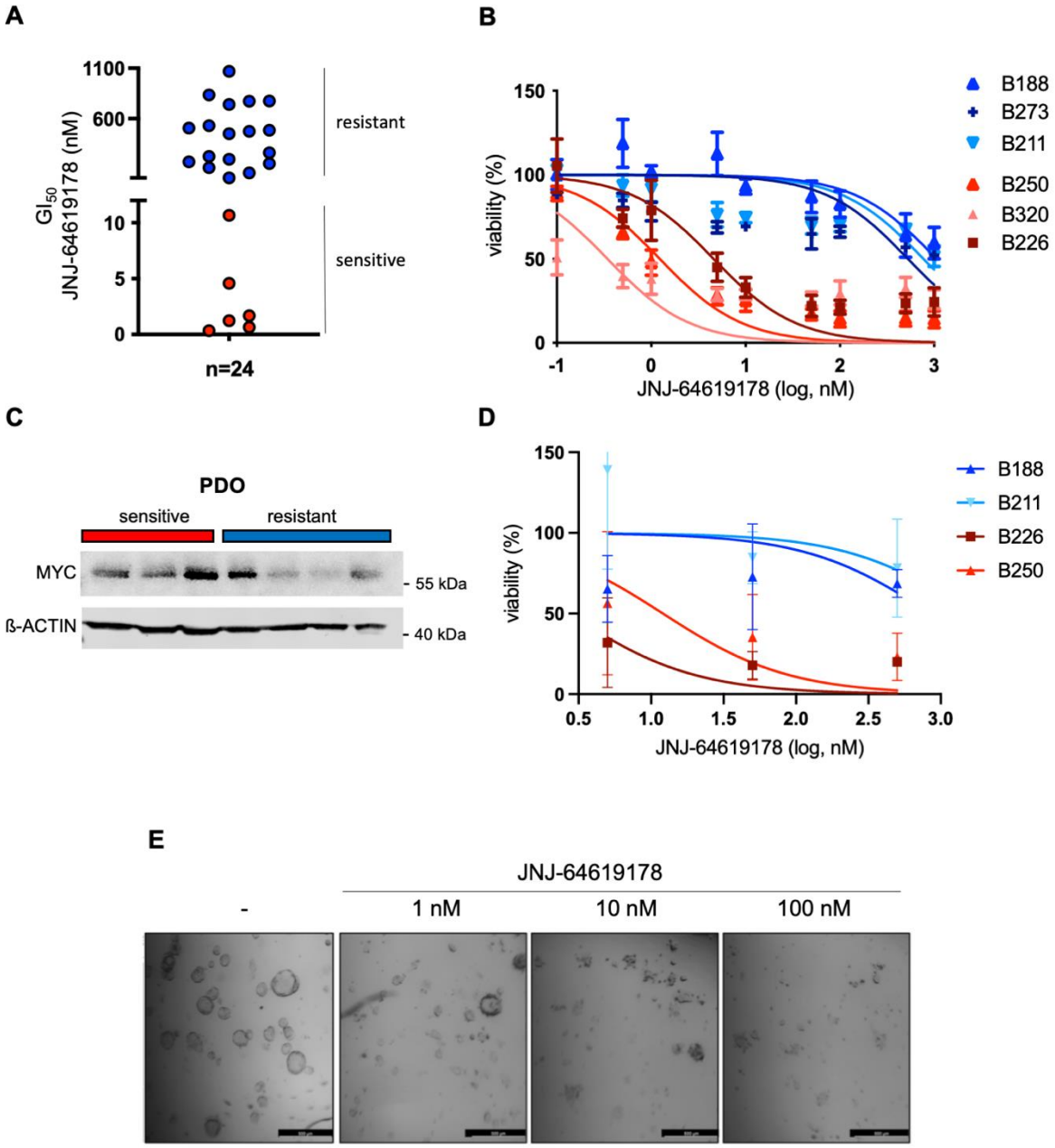

Figure 10: Treatment of PDOs with JNJ-64619178

A) JNJ-64619178 dose-response curves of twenty-four human organoids were determined as in B). GI_{50} values were calculated and are depicted. Red: sensitive organoids, Blue: resistant organoids. The PRMT5i sensitivity status is indicated and was determined by GI_{50} values, considering a GI_{50} <10 nM as sensitive and >500 nM as resistant. **B)** Dose-response curves (max. concentration of 1 µM) of three sensitive and three resistant human PDOs after six days of treatment with JNJ-64619178. Viability was determined with Cell Titer Glo-assay. Sensitive PDOs are marked in red, resistant PDOs are marked in blue. All experiments were made in 3 biological replicates **D)** Dose-response curves (max. concentration of 500 nM) of three sensitive and three resistant human PDOs after two weeks of treatment with JNJ-64619178. Viability was determined with Cell Titer Glo-assay. Sensitive PDOs are marked in red, resistant PDOs are marked in blue. **E)** Microscopy of a sensitive PDAC organoid treated with the indicated dose of JNJ-64619178 or left as a vehicle-treated control over six days. Scale bar = 500 µM.

4.9. Molecular classification of PRMT5i sensitive subtype

To further investigate which pathways are potential markers for a sensitive subgroup, the RNA-seq data of the organoid lines were analyzed with a GSEA. Therefore, the organoid lines were grouped based on their GI_{50} values into quartiles and the most resistant quartile was compared to the most sensitive one. The pre-Rank GSEA was performed by using a log-fold change as a rank. Additionally, full proteome data of the organoids were separated the same way as for the RNA-seq data and analyzed with the Enrichr web tool.

In both, RNA-seq and proteomics, the HALLMARKS MYC TARGETS V1, MYC TARGETS V2, and HALLMARKS DNA REPAIR are enriched (Fig. 11A and 11B). In addition, the GSEA of the RNA-seq data demonstrates a depletion of the HALLMARKS MITOTIC SPINDLE and HYPOXIA in the sensitive organoid lines (Fig. 11B). The strongest enriched HALLMARK signature in the RNA-seq data of the sensitive subgroup is OXIDATIVE PHOSPHORYLATION, whereas the HALLMARKS UNFOLDED PROTEIN RESPONSE and E2F TARGETS show significant enrichment in the proteomics data (Fig. 11A and 11B).

The deletion of the methylthioadenosine phosphorylase gene (*MTAP*), which is often co-deleted with *CDKN2A*, was linked to controlling sensitivity to PRMT5 inhibitors in pancreatic cancer organoids [110]. Despite that, five of our six sensitive organoid lines express high *MTAP* mRNA levels. Only the most sensitive line B320 has low levels of the genes *MTAP* and *CDKN2A* (Fig. 11C). It was described that a high ratio of the *CLNS1A/RIOK* gene expression is a sign of a PRMT5 inhibitor sensitive subgroup in malignant glioma [111]. However, a positive correlation between the *CLNS1A/RIOK* ratio and the GI_{50} response from the PRMT5i in our organoid models could not be detected (SFig. 1). To further elucidate drivers for the sensitivity against the PRMT5 inhibitor, a correlation of all genes from the RNAseq and the GI_{50} values of the organoid lines was performed. Genes that transcribe proteins involved in the assembly of the spliceosome (Serine/arginine-rich splicing factors 3 (SRSF3), SRSF4, survival of motor neuron 1(SMN1), and Survival Motor Neuron Domain Containing 1(SMNDC1)) or that are part of the spliceosome (Splicing Factor 3a Subunit 2 (SF3A2), and Crooked Neck Pre-mRNA Splicing Factor 1 (CRNKL1)) showed a negative correlation between the gene expression and the GI_{50} value of the inhibitor response (Fig. 11D). In conclusion, a PRMT5i sensitive subtype exists

in human primary organoid models, which is not connected to a co-deletion of *MTAP* and *CDKN2A*. This subtype demonstrates a link to a deregulated MYC network and a dependency on the splicing machinery.

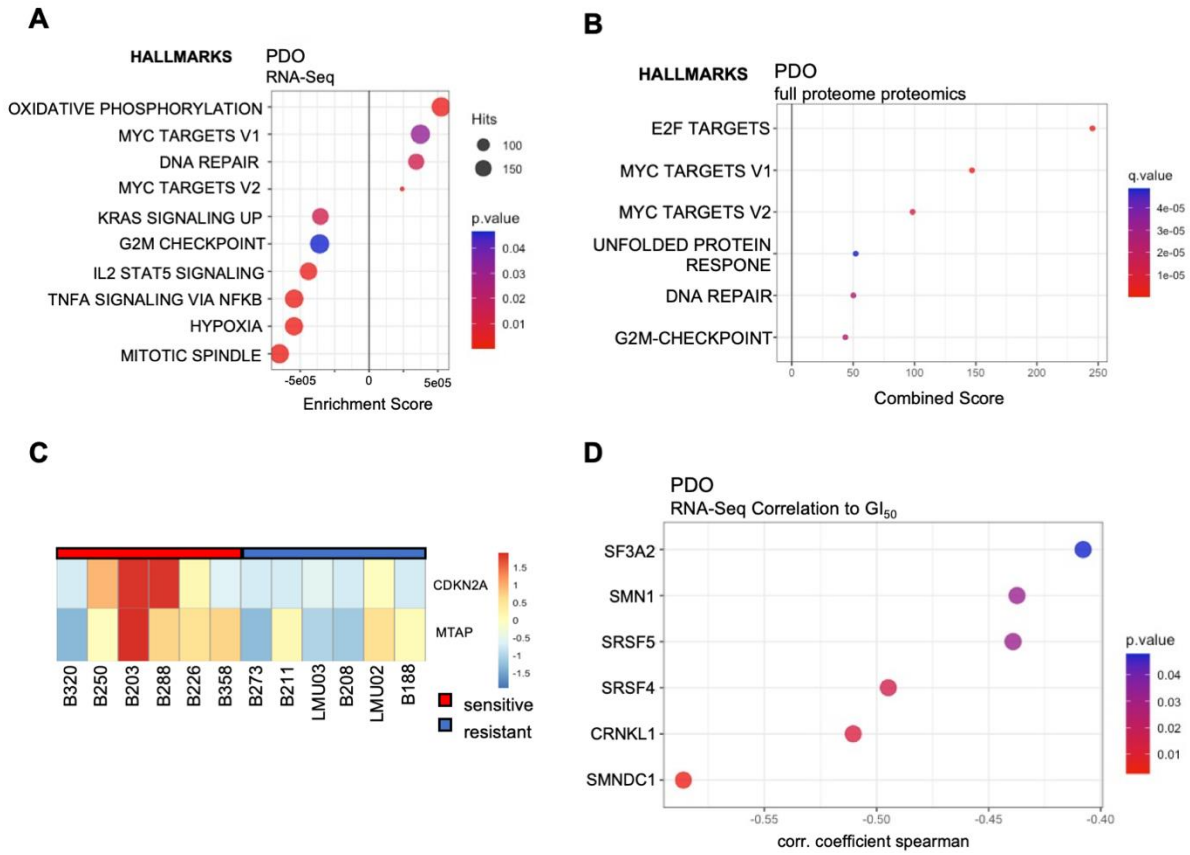

Figure 11: Characterization of PDO sensitive subtype

A) RNA-seq of the most sensitive (n=6) versus the most resistant quartile (n=6) of the organoid lines was used to determine differentially expressed genes. The log2fold change was used to perform a pre-ranked GSEA using the GeneTrail3 web tool. Depicted are the HALLMARK signatures with q values <0.05. The q-value is color-coded and depicted. **B)** Full proteome proteomics of the most sensitive (n=6) versus the most resistant quartile (n=6) of the organoid lines was used to determine differentially expressed proteins. All proteins upregulated in the sensitive PDOs were analyzed by using the Enrichr web tool. Depicted are the HALLMARK signatures with q values <0.05. The q-value is color-coded and depicted. C**)** mRNA expression based on an RNA-seq of the tested organoids and genes is illustrated in a heatmap. Subgroup is indicated as blue (resistant) and red (sensitive) **D)** The Correlation coefficient based on RNA-seq and the GI_{50} values of the 24 tested organoids from A). The q-value is color-coded and depicted.

4.10. Multi-targeting of PRMTs

To investigate if a multi-layer buffering system of the different PRMTs contributes to the heterogeneity seen in the response to the treatment with PRMT5 inhibitors, the correlation of *MYC* gene expression to other PRMTs was analyzed. Not only *PRMT5* (Fig. 4A) but also *PRMT1* and *PRMT3* have a significant positive correlation to *MYC* as determined by the RNA-seq of the PDOs (Fig. 12A). This suggests that the multi-layer buffering system may be more vulnerable when targeted by more than one PRMT inhibitor. Therefore, the human PDAC cell line HupT3 was challenged with a combination of PRMT inhibitors. The PRMT3 inhibitor SGC707 in combination with the already tested PRMT5i resulted only in a mild synergistic drug response with an overall ZIP synergy score of 4.67 (Fig. 12B). However, the class I PRMT inhibitor GSK3368715, which targets PRMT1, PRMT3, PRMT4, PRMT6, and PRMT8 shows a stronger synergistic effect in combination with JNJ-64619178. Precisely, the overall ZIP synergy score between these two drugs is 15.8 (Fig. 12C). To visualize the synergistic effect in a dose-response curve, HupT3 was treated in a seven-point dilution of JNJ-64619178 in combination with either 50 nM GSK3368715 or 50 nM SGC707 (Fig. 12D). As expected, the combination of JNJ-64619178 and GSK3368715 results in a synergistic effect with a reduction of the area under the curve value (Fig. 12E). Thus, multitargeting of several PRMTs could boost the efficacy of PRMT5 inhibition, which needs to be considered for clinical testing.

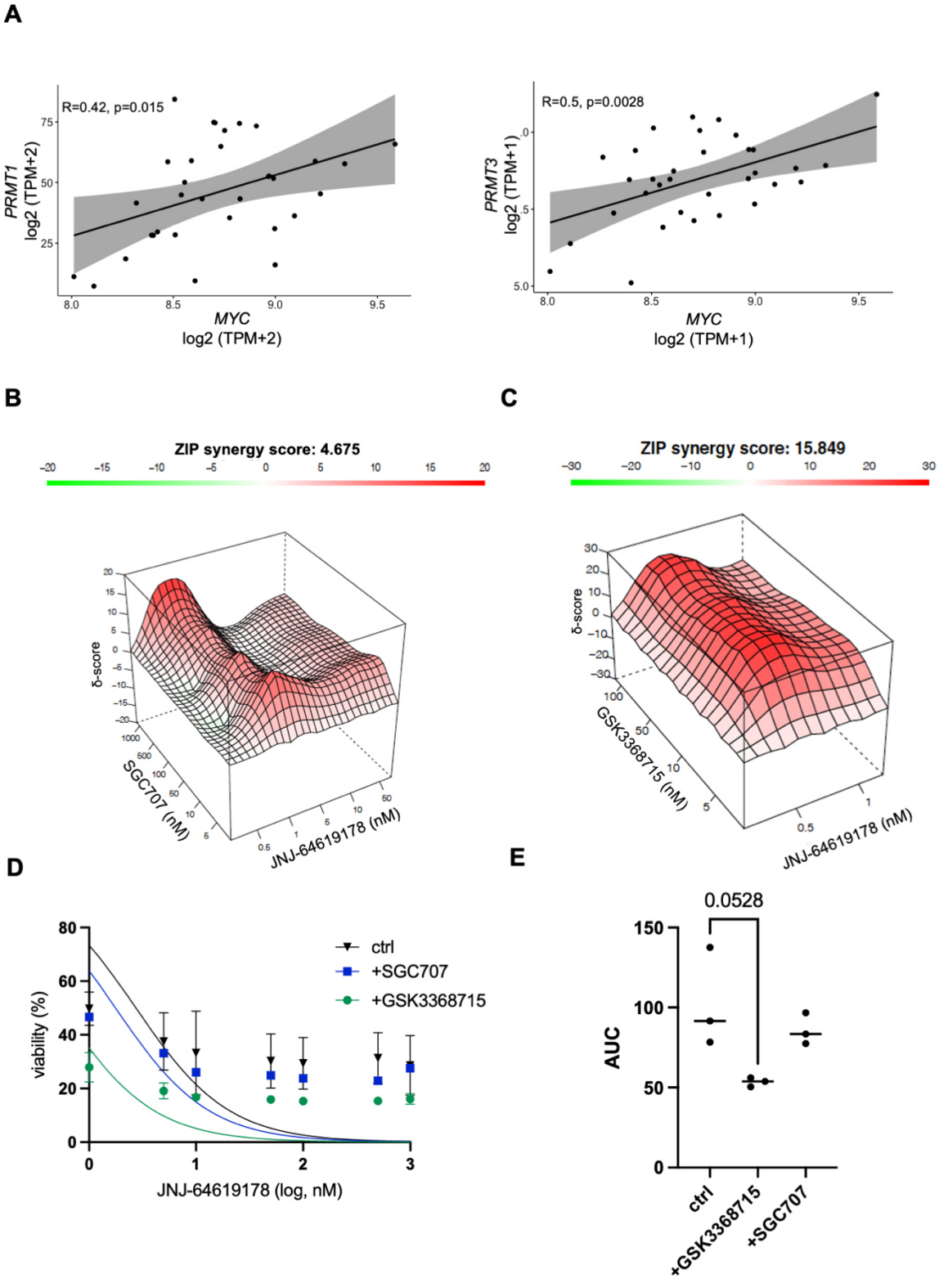
A
R=0.42, p=0.015
PRMT1
log2 (TPM+2)
MYC
log2 (TPM+2)
R=0.5, p=0.0028
PRMT3
log2 (TPM+1)
MYC
log2 (TPM+1)
B
ZIP synergy score: 4.675
δ-score
SGC707 (nM)
JNJ-64619178 (nM)
C
ZIP synergy score: 15.849
δ-score
GSK3368715 (nM)
JNJ-64619178 (nM)
D
viability (%)
ctrl
+SGC707
+GSK3368715
JNJ-64619178 (log, nM)
E
0.0528
AUC
ctrl
+GSK3368715
+SGC707

Figure 12: Multitargeting of PRMTs

A) Depicted is the Pearson correlation coefficient and the linear regression in primary human PDAC organoids (PDO, n=33) between *MYC* and *PRMT1* or *PRMT3* mRNA expression based on RNA-seq. **B)** Synergy map of JNJ-64619178 and SGC707 co-treated HupT3 cells. The experiment was conducted in three biological replicates **C)** Synergy map of JNJ-64619178 and SGC707 co-treated HupT3 cells. The experiment was conducted in three biological replicates. **D)** JNJ-64619178 dose response curve (max. concentration 1 µM) of HupT3 cells, co-treated with vehicle control, GSK3368715 or SGC707 as indicated. The experiment was conducted in three biological replicates. **E)** Area under the curve (AUC) values of dose-response curves from D) were determined. The p-value of an unpaired t-test is indicated.

4.11. Control of glycolysis by PRMT5

A recent publication describes a connection of PRMT5 with the aerobic glycolysis in PDAC cells [112]. High PRMT5 was connected to increased aerobic glycolysis, which could point to a vulnerability that can be targeted with PRMT5 inhibitors. To further investigate glycolysis under treatment with a PRMT5 inhibitor, a functional analysis for measuring the energetic metabolism of the treated cells was performed. The Seahorse assay uses the measured oxygen consumption rate (OCR) and extracellular acidification rate (ECAR) of live cells as surrogates for mitochondrial respiration and glycolysis. For this assay, two human PDAC cell lines characterized by a low *MYC* RNA expression (Panc1 and HPAC) and two with a high *MYC* RNA expression (DanG and PSN1) were grouped into *MYC* low, and *MYC* high, respectively (Fig. 13A). The measurement of the oxygen consumption rate revealed a reduced basal mitochondrial respiration, ATP-linked respiration, and maximal respiratory capacity in both groups after treatment with 20 nM JNJ-64619178. However, no substantial difference could be seen between the two groups (Fig. 13B). The analysis of the ECAR showed that the *MYC* high cell lines had a drastically reduced glycolysis, whereas the glycolytic rate in the two cell lines with the low *MYC* expression did not change after treatment with JNJ-64619178. The total glycolytic capacity and the glycolytic reserve were reduced in both groups to a similar level (Fig. 13C).

The data of the Seahorse assay presumed, that glycolysis is strongly altered after inhibition of PRMT5, but only in cells with a high *MYC* expression. To confirm this finding, a glucose uptake assay was performed in the same setting. The group with the low *MYC* expression had a reduction of the glucose uptake of 6%, whereas the group with the high *MYC* expression showed a reduction of more than 40% (Fig.

12D). The reduction of the glycolytic activity was also observed in RNA-seq data of DanG and PSN1 cell lines, which show a depletion of the HALLMARK signature GLYCOLYSIS after treatment with JNJ-64619178 [97]. The decreased rate of glycolysis under PRMT5 inhibitor treatment points to a dependency on glycolysis in cell lines with increased *MYC* expression.

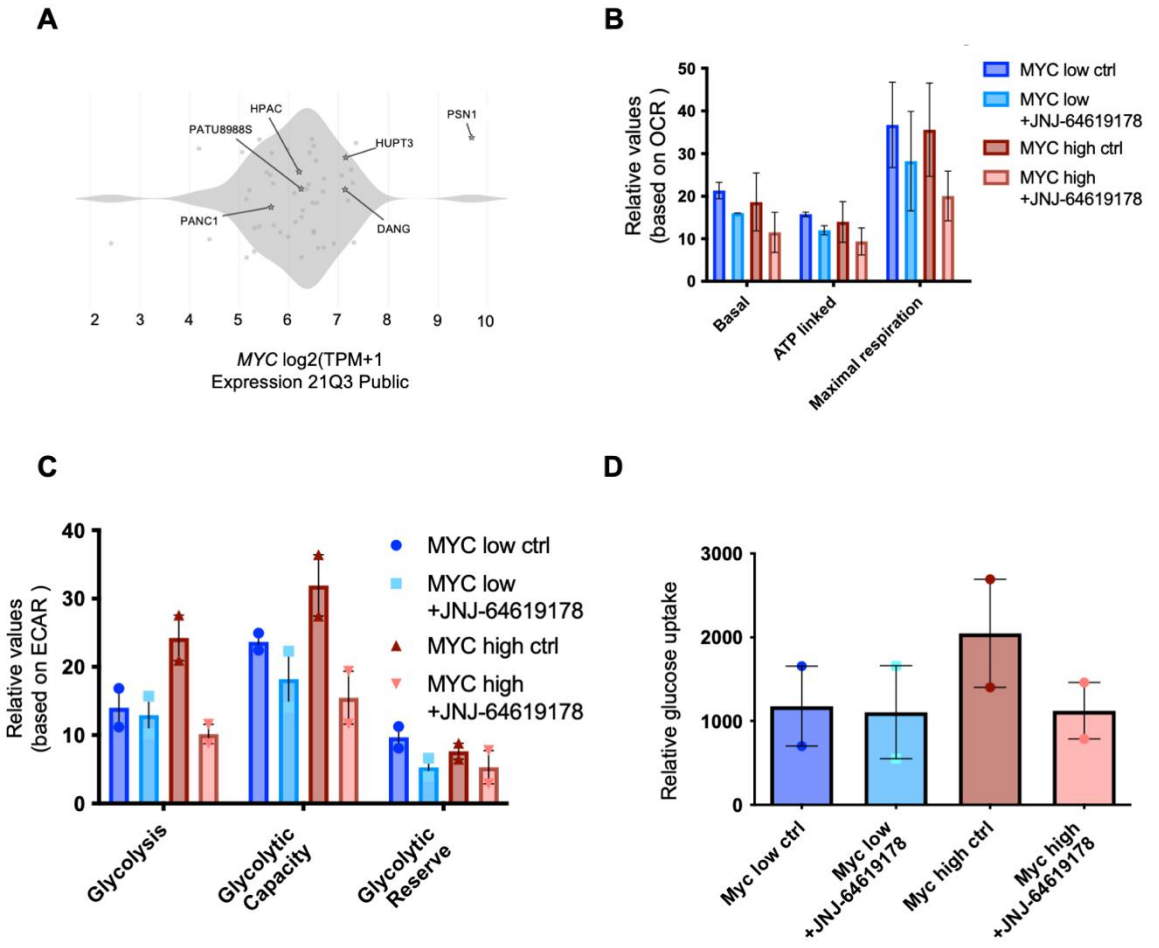

Figure 13: Metabolic analysis of PDAC cell lines

A) *MYC* expression of indicated human PDAC cell lines based on the RNA expression of the "21Q3 Public dataset" from depmap portal. **B)** Cell lines with low *MYC* expression (Panc1 and HPAC) and with high *MYC* expression (DanG and PSN1) were treated with 20 nM JNJ-64619178 or vehicle control for 3 days and OCR values were measured via the Seahorse assay in the Seahorse XF96 analyzer. The experiment was conducted in three biological replicates. **C)** Cell lines with low *MYC* expression (Panc1 and HPAC) and with high *MYC* expression (DanG and PSN1) were treated with 20 nM JNJ-64619178 or vehicle control for 3 days and ECAR values were measured via the Seahorse assay in the Seahorse XF96 analyzer. The experiment was conducted in three biological replicates. **D)** Promega glucose uptake assay of two *MYC* high (DanG and PSN1) and two *MYC* low (HPAC and Panc1) cell lines after 3 days treatment with 20 nM JNJ-64619178 or vehicle control. The experiment was conducted in three biological replicates.

4.12. PRMT5i induced apoptosis is dependent on MYC expression

After validation that PRMT5i triggers a MYC-associated vulnerability, the underlying mechanism and the effect on the cell fate were investigated. It was shown that PRMT5 inhibition induces a DNA-damage response and accumulation of DNA-DSB in PDAC cell lines, measured by immunofluorescence detection of γ-H2AX [113]. DNA-DSBs are also proposed to trigger apoptosis, which can be measured via the cleavage of the caspase substrate PARP [114]. A recent publication from the Schneider laboratory (Technical University Munich, Klinikum rechst der Isar), measured the cleavage of PARP in different PDAC cell lines with a heterogenous MYC protein expression. Interestingly, only the two cell lines with an increased MYC expression (PSN1 and DanG) showed cleavage of PARP after 3 days of treatment with 20 nM of JNJ-64619178 [97], supporting the lethal interaction between MYC and PRMT5. To support the assumption that a high MYC protein expression is connected to PRMT5i induced apoptosis, DanG cells were treated with JNJ-64619178 and the BET degrader ARV-771. In this setting, the downregulation of the MYC level by ARV-771 significantly reduced JNJ-64619178-mediated cleavage of PARP to 20 %, compared to treatment with the PRMT5 inhibitor alone (Fig. 14A and 14B). With the cleavage of PARP, it could be shown that JNJ-64619178 induces apoptosis in PDAC cell lines, especially in cell lines with a high *MYC* expression. Furthermore, reduction of the MYC protein level results in decreased levels of cleaved PARP, supporting the relevance of MYC in the induction of apoptosis after treatment.

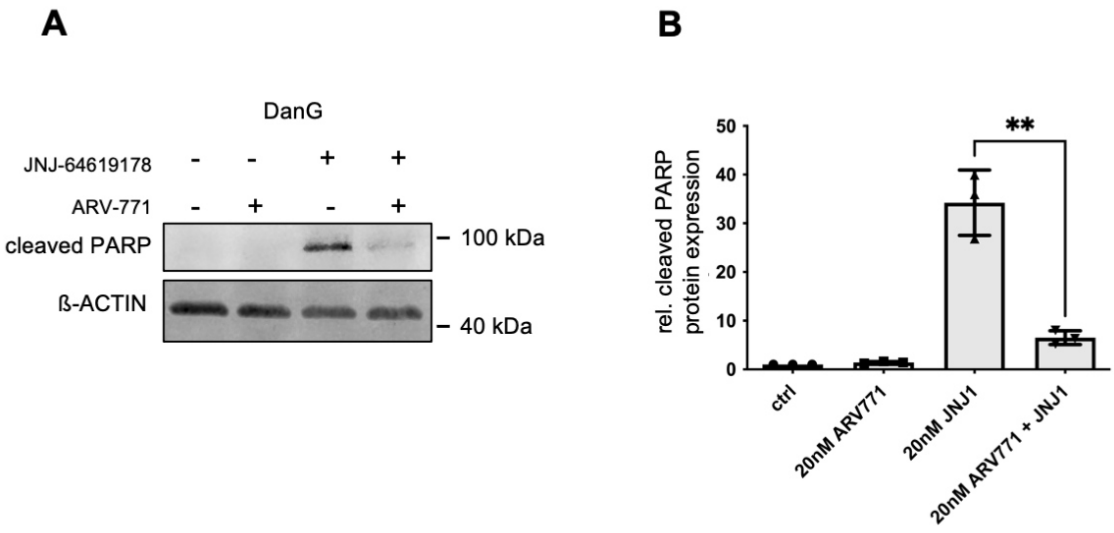

Figure 14: Induction of apoptosis after treatment with JNJ-64619178

A) Cleaved PARP western blot analysis of the DanG cell line, which was treated for three days with either 20 nM JNJ-64619178, 20 nM ARV-771, a combination of the two, or was left as vehicle-treated control as indicated. ß-ACTIN served as a loading control. One representative experiment out of three replicates is depicted. **B)** Quantification of the cleaved PARP protein expression based on three independent experiments from A). **p-value of an unpaired t-test with a p-value of <0.005.

4.13. Inhibition of PRMT5 impacts cell cycle progression and mitosis

It was described that signatures connected to the G2/M-phase of the cell cycle, mitosis, and the E2F pathway are enriched after inhibition of PRMT5 [97]. To validate the finding of an altered G2/M-phase of the cell cycle, the mitotic marker genes targeting protein for Xklp2 (TPX2), which functions in the assembly of the mitotic spindle, and the mitotic spindle regulator Aurora Kinase B (AURKB) were investigated via Western Blot. Whereas TPX2 was upregulated after treatment with JNJ-64619178 (Fig. 15 B), the mitotic regulator AURKB was downregulated after treatment (Fig. 15A). The downregulation of AURKB after PRMT5 inhibition is in line with a recent finding by Braun et al. [111]. This cell cycle regulation was seen irrespectively of the MYC status.

A well-established function of PRMT5 is to assure splicing fidelity in cells. Cells with oncogenic MYC activation have a high mRNA burden [115] and could therefore rely on an active PRMT5 to orchestrate the splicing of the high mRNA load. To see if the PRMT5 blockade leads to an additional MYC-associated vulnerability due to the reduced splicing fidelity, a combination treatment of JNJ-64619178 and Indisulam

was tested. Indisulam treatment results in rapid proteasomal degradation of RBM39, a pre-mRNA splicing factor, resulting in aberrant pre-mRNA splicing [116]. The combination showed a high synergistic effect in the human PDAC cell line DanG resulting in an overall ZIP synergy score of 15.36 after 6 days of treatment (Fig. 15C). Taken together, this data shows that the cell cycle is altered after treatment with JNJ-64619178 irrespectively of the MYC protein level. However, only in cells with overexpression of *MYC*, which are highly dependent on a functioning cell cycle and splicing machinery, the cell fate is switched to apoptosis.

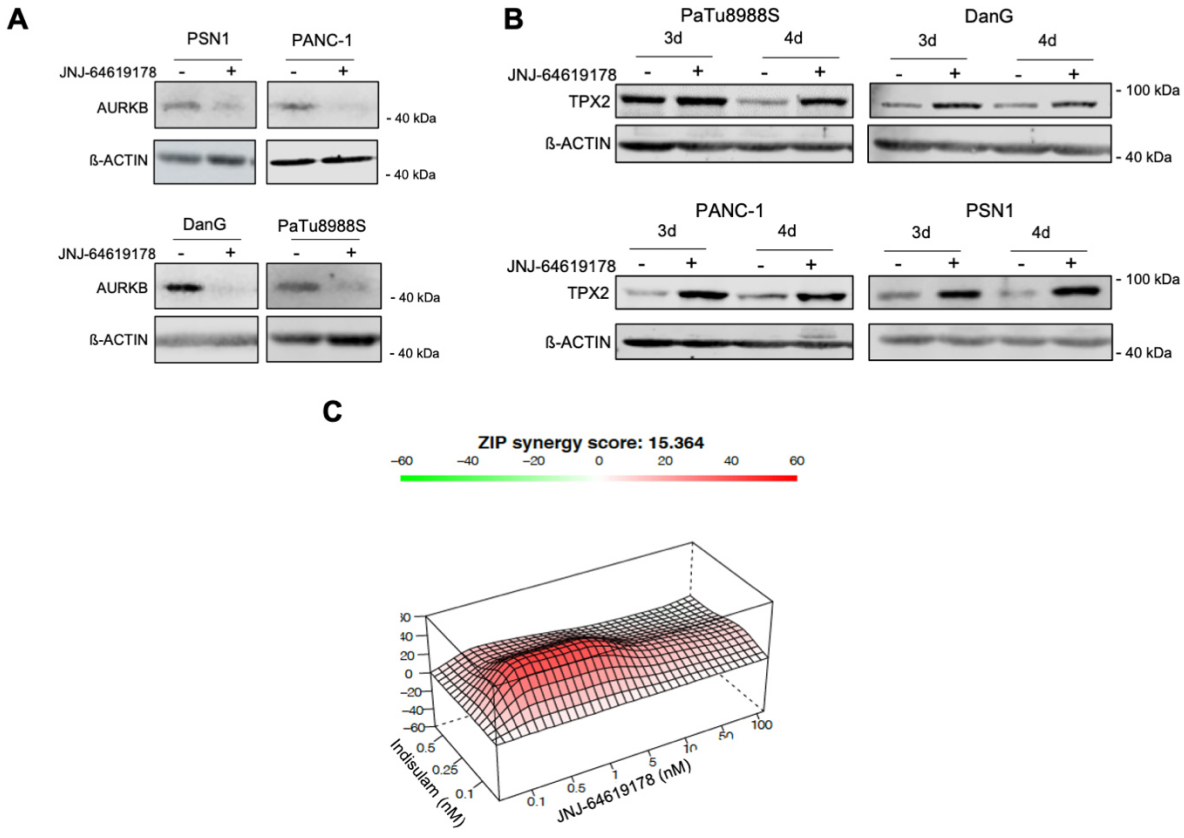

Figure 15: Characterization of PRMT5i response in PDAC cell lines

A) Aurora kinase B (AURKB) western blot analysis of indicated cell lines, which were treated for four days with 20 nM JNJ-64619178 or were left as a vehicle-treated control. ß-ACTIN served as a loading control. One representative experiment out of two replicates is depicted. **B)** TPX2 western blot analysis of indicated cell lines, which were treated for three and four days with 20 nM JNJ-64619178 or were left as a vehicle-treated control. ß-ACTIN served as a loading control. One representative experiment out of two replicates is depicted. **C)** Synergy map of JNJ-64619178 Indisulam co-treated DanG cells.

5. Discussion

This thesis provides a detailed characterization of how a PRMT5 inhibitor can trigger an MYC-associated epigenetic vulnerability in PDAC cell models, by exploiting the synthetic dosage lethality of *MYC*-deregulated cancer cells. This is especially relevant since PDAC is one of the most lethal cancer types and current standard of care treatment approaches remain often unsuccessful. Therefore, new therapeutic strategies are needed, particularly for the aggressive PDAC subgroup with a high *MYC* expression.

Protein arginine methyltransferases cluster into three classes, based on their mode of methylating proteins. PRMT5 belongs to the group of type II PRMTs, together with the protein PRMT9. In PDAC, a high expression of *PRMT5* is connected to glycolysis [112] and EMT [117]. These two processes are connected with the basal-like subtype of PDAC, which is also characterized by an aggressive clinical behavior [35]. In addition, PDACs with high *PRMT5* and high *MYC* gene expression, which is also seen in the basal-like subtype, have a worse clinical prognosis [35]. Consistently, *PRMT5* and *MYC* show a high correlation in different tumor entities, with the highest correlation in PDAC. This indicates that PRMT5 is an interesting target in the aggressive pancreatic cancer subtype, with upregulated MYC levels. So far, there are only a few subgroup-specific treatment options except for platin-based therapy with subsequent PARP-inhibitor treatment in PDAC patients with a gBRCA1/2 mutation. The other subgroup consists of patients with a high microsatellite instability, which show a good treatment response from therapy with immune-checkpoint inhibitors like PD-1 antibodies. The lack of therapeutic targets in PDAC supports the importance of research on novel, targeted therapies for this tumor indication.

Recently, PRMT5 inhibitors are in the focus of research groups to find new treatment strategies in the fight against cancer, which led to the entering of the PRMT5 inhibitors JNJ-64619178 (NCT03573310), PF-06939999 (NCT03854227), GSK3326595 (NCT02783300) in clinical phase testing for solid cancers and hematological cancer. It was demonstrated that a subgroup of pancreatic cancers exists, which are sensitive to the inhibition of PRMT5. A PRMT5 inhibitor sensitive subtype in primary patient-derived PDAC organoids could also be observed in the here presented study. Recently, sensitive subtypes were connected to an

underlying *MTAP* deletion [118], the *CLNS1A/RIOK1* expression ratio, or the addiction to the splicing machinery [111]. These connections will be discussed in the following.
MTAP deletion is often found in PDAC as a co-deletion due to the proximity to *CDKN2A*, one of the most frequently deleted tumor suppressor genes. The deletion of *MTAP* leads to the accumulation of MTA, which decreases the activity of PRMT5 by competing with the activation cofactor SAM [119]. This MTA-driven PRMT5 inhibition promotes an increased sensitivity to further PRMT5 reductions. However, the authors mention that the *MTAP* status alone is not sufficient to distinguish PRMT5i sensitive cell lines. The correlation of *MTAP* deletion and the PRMT5 inhibitor response could not be observed in the demonstrated organoid models, in which 5 of the 6 most sensitive lines are *MTAP*-proficient. The missing correlation between the *MTAP* deletion status and the JNJ-64619178 treatment response in the here presented study can be explained by the mode of action of the inhibitor. JNJ-64619178 binds simultaneously and with a high affinity to the S-adenosylmethionin- and substrate-pocket and inhibits therefore the formation of PRMT5-MTA complexes [120].
Braun et al. described a predictive biomarker for the identification of PRMT5 inhibitor sensitive subtypes in malignant glioma. A high ratio of the gene expression of *CLNS1A/RIOK1* correlates in this publication with a sensitive subtype. The underlying mechanism is a directing of the PRMT5 activity by CLNS1A towards the methylation of components of the spliceosome [111]. The *CLNS1A/RIOK1* gene expression ratio did not correlate to the GI_{50} values of the tested PDO lines, nor was the ratio higher in the sensitive subtype compared to the resistant ones. However, there is a huge heterogeneity between different tumor tissue origins, and it is not expected that a predictive biomarker in one tumor type is a valid biomarker in other tumor types. Nevertheless, the strong dependency on splicing, which is reinforced by the *CLNS1A/RIOK1* ratio, could also be seen in the here presented PDO models. A correlation of all genes to the drug response of JNJ-64619178 revealed that many genes involved in the spliceosome activity are negatively correlated. This correlation suggests that the PRMT5 activity could be skewed to spliceosomal targets in the sensitive subtype and that the inhibition of PRMT5 could have a larger impact on cells that depend on the splicing machinery. However, this assumption needs further clarification.

A recent study found evidence that MYC regulates the constitutive splicing machinery, including PRMT5, in the *Eμ-myc* lymphoma model [121]. It was proposed that MYC overexpression leads to increased total mRNA burden in the cell, which results in a dependency of the cells on the PRMT5 orchestrated splicing fidelity. The here presented study shows a strong connection between PRMT5 and MYC. The induction of *MYC* expression in conditional models leads to an upregulation of PRMT5 on the RNA and protein levels. Furthermore, the effect could also be observed vice versa when inhibiting *PRMT5* expression. It could be demonstrated that an upregulation of the *MYC* expression in the conditional and CRISPR modified cell lines leads to a higher sensitivity to the PRMT5 inhibitor JNJ-64619178. This supports the assumption that the increased RNA burden after *MYC* activation leads to a dependency on the PRMT5 regulated splicing fidelity. This notion is strengthened by the finding that a pharmacological knockdown of MYC leads to resistance against PRMT5 inhibition.

The impact of MYC on the splicing machinery was also recently described in an unbiased drug screen in human mammary epithelial cells which could upregulate the MYC activity via the MYC-ER system [122]. BUD31, a spliceosome component, was found to be synthetically lethal with MYC. Furthermore, this study could show that the partial inhibition of the spliceosome leads to global intron retention and death in MYC-hyperactivated cells [122]. This further indicates that cancer cells with an upregulated MYC network have a dependency on the splicing machinery. Since one core function of PRMT5 is the regulation of the splicing fidelity, the high levels of MYC contribute to the sensitivity of PDAC cell lines to PRMT5 inhibitor treatment. In short, pre-mRNA splicing could be necessary for tumor cell lines to tolerate oncogenic MYC levels.

Upregulation of the MYC network could also be observed in the patient-derived organoids. Both, RNA-seq and proteomics data analysis revealed enriched HALLMARKS for MYC target genes. This finding underscores the assumption that high MYC levels are an important characteristic, which renders PDAC cells sensitive to PRMT5 inhibition. In addition, the HALLMARK signature DNA REPAIR was upregulated in the sensitive subgroup. DNA repair pathways maintain genetic stability by detecting DNA double-strand breaks, chromosomal translocation and deletions, and can correct some of those alterations [123]. Normally, PDAC is characterized by genomic instability, which is also one of the enabling processes

from the hallmarks of cancer, which were described by Hanahan and Weinberg [124]. However, the high expression of *PRMT5* in the sensitive subtype and its function in the DNA damage response could lead to this upregulated DNA repair signature compared to the resistant organoid lines. In addition, the high MYC level in the cells leads to a high proliferation rate and cellular stress. Therefore, the DNA damage response could be upregulated in an attempt to cope with the MYC-induced cellular stress. The enriched HALLMARK OXIDATIVE PHOSPHORYLATION and the depleted HALLMARK HYPOXIA are signs that the sensitive subgroup uses oxygen to generate ATP for energy. Interestingly, the PRMT5 inhibitor-sensitive 2D cell lines were characterized by a high glycolytic activity, which is a sign for the basal-like PDAC subtype. The reason for an enriched oxidative phosphorylation signature in the sensitive organoid lines needs to be further investigated in subsequent studies. But it demonstrates that the metabolic network of cancer cells is a complex matter and cannot always be pinned down to one subgroup based on the expression of just a few genes.

As already mentioned, the blockade of PRMT5 reduces the splicing fidelity of cells. The reduced splicing fidelity and blockade of PRMT5 also prevent the removal of detained introns in the mitotic spindle regulator AURKB [111]. Interestingly, AURKB depletion by the inhibitor VX-680 was found to be synthetic lethal in cells overexpressing MYC [125]. A depletion of AURKB was also found in this study after treatment with 20 nM JNJ-64619178. Absent PRMT5, a recent review summarizes how increased expression of MYC leads to mitotic alterations and vulnerabilities in PDAC [126]. Furthermore, it could be shown that a PRMT5 inhibition leads to splicing defects and alters cell cycle progression in hematopoietic and glioblastoma cells [67,127]. Together, it is worth considering that the connection of the increased PRMT5i sensitivity of PDAC cells with upregulated MYC levels comes from a contribution of the cell cycle and mitotic genes. This is strengthened by the finding, that the sensitive organoid subgroup has the HALLMARK signature E2F TARGETS enriched in the proteomics data.

Qin et al. described how high PRMT5 levels can upregulate glycolysis via the FBW7/cMYC axis. Furthermore, they could show that PRMT5-silenced PDAC cell lines and mouse models exhibit a decreased glycolytic capacity [112]. The glycolytic PDAC subtype, which correlates to the basal/squamous profile, is also the more aggressive tumor with higher resistance to chemotherapy [128]. Functional analysis of

the energetic metabolism via the Seahorse assay revealed that the tested cell lines with a high *MYC* expression have higher glycolytic activity compared to the lines with a low *MYC* expression. Furthermore, glycolysis is strongly altered under treatment with a PRMT5 inhibitor in PDAC cell lines with a high *MYC* expression. The effect could not be observed in cell lines with a low MYC expression [97]. The glucose uptake assay confirmed the observed impact of the PRMT5 inhibitor on glycolysis. The finding supports the notion that high levels of PRMT5 and MYC are linked to glycolysis and that this is associated with an additional vulnerability that can be targeted with PRMT5 inhibitors.

A positive correlation between the RNA expression of several *PRMTs* and *MYC* could be observed in the organoid repository. Such data might indicate a dependency of MYC-driven cancers on the protein arginine methyltransferase machinery. Inhibition of PRMT1 was described to block MYC-mediated transcription of several MYC target genes [129]. Indeed, targeting the type I PRMTs and PRMT5 simultaneously result in a strong synergistic effect in an MYC-deregulated PDAC cell line. Whether targeting this multi-layer buffering system is especially potent in cancer cells with high levels of MYC and if it contributes to the heterogeneity of the PRMT5 inhibitor response needs to be deciphered in future work.

6. Future Perspective

PDAC with deregulated levels of MYC has a very dismal prognosis with currently no curative treatment options except tumor resection. The data provided in this study gives a comprehensive characterization of the synthetic lethal relationship between MYC and PRMT5 in PDAC. These findings underscore the potential of PRMT5 inhibitors as a novel therapeutic option for PDAC patients with a deregulated MYC network.

Although PRMT5 is a promising target for inhibition in PDAC patients due to its effects in alternative splicing and glycolysis, the protein has various other roles. Therefore, an in-depth understanding of the molecular effects when inhibiting PRMT5 needs to be established and patient stratification based on the molecular context is of great importance. If this will be considered, PRMT5 inhibition could improve the therapeutic options in PDAC patients with MYC-driven cancers, especially due to an assumably lower therapy resistance compared to conventional chemotherapy.

VI. Appendix

Supplementary Table 1:
Correlation coefficient between *MYC* and *PRMT5* RNA expression in different tumor entities. Gene expression and analysis of the correlation between *MYC* and *PRMT5* of the different tumor entities was performed on the depmap portal web tool.

Group	Number of Points	Pearson	Spearman	Slope	Intercept	p-value
peripheral_nervous_system	29	-0,352	-0,374	-5,52E-02	6,68E+00	6,08E-02
eye	9	-0,231	-0,417	-5,27E-02	6,73E+00	5,50E-01
plasma_cell	30	0,075	0,13	3,54E-02	5,94E+00	6,93E-01
lung	205	0,119	0,141	3,67E-02	6,52E+00	8,80E-02
prostate	11	0,216	0,255	1,24E-01	5,72E+00	5,23E-01
uterus	40	0,227	0,262	1,19E-01	5,84E+00	1,60E-01
gastric	40	0,243	0,182	1,56E-01	5,72E+00	1,30E-01
esophagus	32	0,255	0,225	2,06E-01	5,20E+00	1,59E-01
upper_aerodigestive	54	0,26	0,233	1,93E-01	5,00E+00	5,79E-02
thyroid	17	0,267	0,333	9,63E-02	6,18E+00	3,01E-01
skin	83	0,281	0,264	1,24E-01	5,56E+00	9,99E-03
breast	61	0,309	0,209	1,87E-01	5,07E+00	1,55E-02
central_nervous_system	84	0,328	0,302	1,48E-01	5,58E+00	2,29E-03
urinary_tract	36	0,339	0,242	2,15E-01	5,17E+00	4,30E-02
liver	24	0,353	0,331	2,32E-01	5,19E+00	9,07E-02
bone	39	0,36	0,297	1,46E-01	5,81E+00	2,43E-02
blood	101	0,371	0,25	2,11E-01	4,69E+00	1,36E-04
kidney	38	0,392	0,215	4,02E-01	3,20E+00	1,48E-02
bile_duct	41	0,432	0,497	2,44E-01	4,85E+00	4,84E-03
cervix	17	0,44	0,463	2,48E-01	4,90E+00	7,69E-02
colorectal	70	0,482	0,47	2,61E-01	4,85E+00	2,40E-05
ovary	64	0,484	0,486	3,52E-01	4,37E+00	5,08E-05
lymphocyte	83	0,545	0,531	3,85E-01	3,53E+00	9,75E-08
pancreas	52	0,647	0,606	4,65E-01	3,55E+00	2,14E-07

Supplementary Table 2:
GSEA HALLMARKS of HPAC CRISPRa Myc2-guide cell line.

Type	Rank	Name	Number of hits	Score	Q-value
depleted	1	HALLMARK TNFA SIGNALING VIA NFKB	181	-878208	5,55E-15
enriched	2	HALLMARK MYC TARGETS V2	58	388325	5,21E-09
enriched	3	HALLMARK MYC TARGETS V1	200	697478	3,01E-08
depleted	4	HALLMARK INFLAMMATORY RESPONSE	131	-548575	7,18E-08
depleted	5	HALLMARK INTERFERON ALPHA RESPONSE	91	-451262	7,23E-08
depleted	5	HALLMARK MITOTIC SPINDLE	197	-667369	7,23E-08
depleted	7	HALLMARK EPITHELIAL MESENCHYMAL TRANSITION	164	-568867	7,82E-07
depleted	8	HALLMARK KRAS SIGNALING UP	139	-519737	8,78E-07
depleted	9	HALLMARK APOPTOSIS	138	-504649	1,88E-06
depleted	10	HALLMARK INTERFERON GAMMA RESPONSE	160	-505756	1,55E-05
depleted	11	HALLMARK IL6 JAK STAT3 SIGNALING	61	-308861	1,59E-05
enriched	12	HALLMARK OXIDATIVE PHOSPHORYLATION	197	555517	1,73E-05
depleted	13	HALLMARK G2M CHECKPOINT	197	-433209	3,70E-03
depleted	14	HALLMARK PROTEIN SECRETION	93	-292994	4,40E-03
depleted	15	HALLMARK TGF BETA SIGNALING	53	-217619	5,00E-03
depleted	16	HALLMARK ALLOGRAFT REJECTION	115	-316724	6,10E-03
depleted	17	HALLMARK COAGULATION	87	-270543	0,0074
depleted	18	HALLMARK HYPOXIA	176	-380578	0,0085
depleted	19	HALLMARK APICAL JUNCTION	165	-363616	0,0093
depleted	19	HALLMARK ESTROGEN RESPONSE LATE	173	-372151	0,0093
depleted	21	HALLMARK APICAL SURFACE	35	-157684	0,0174
depleted	22	HALLMARK IL2 STAT5 SIGNALING	161	-330281	0,0251
depleted	23	HALLMARK COMPLEMENT	143	-308771	0,0264
depleted	24	HALLMARK ESTROGEN RESPONSE EARLY	184	-343875	0,0313
enriched	25	HALLMARK MYOGENESIS	138	295240	0,0331

Supplementary Table 3:
GSEA HALLMARKS of PANC-1 CRISPRa Myc2-guide cell line.

Type	Rank	Name	Number of hits	Score	Q-value
enriched	1	HALLMARK MYC TARGETS V1	200	936888	1,81E-15
enriched	2	HALLMARK G2M CHECKPOINT	197	780599	1,18E-10
enriched	3	HALLMARK E2F TARGETS	200	773078	2,03E-10
enriched	4	HALLMARK MYC TARGETS V2	58	320865	6,11E-06
depleted	5	HALLMARK EPITHELIAL MESENCHYMAL TRANSITION	164	-430993	0,002
enriched	6	HALLMARK OXIDATIVE PHOSPHORYLATION	197	438169	0,0066
depleted	7	HALLMARK ESTROGEN RESPONSE EARLY	184	-404038	0,0123
depleted	8	HALLMARK COMPLEMENT	143	-345180	0,0155
depleted	8	HALLMARK INTERFERON GAMMA RESPONSE	160	-367255	0,0155
depleted	10	HALLMARK TNFA SIGNALING VIA NFKB	181	-380769	0,0185

Supplementary Table 4:
Clinical data PDOs.

Organoid	KRAS status	Source	Gender	Age at Diagnosis	p Staging	Grading
B121	G12D	FNB	male	70-80	cT2CN1M1	G2
B140	G12D	Surgery	female	70-80	pT2pN1(3/22)cM0Pn1L1R0	G2
B169	G12D	Surgery	male	70-80	pT2pN1cM0	G2
B188	G12D	FNB	male	60-70	ypT3ypN1(3/23)Pn1	-
B203	G12D	FNB	female	40-50	-	-
B208	G12D	Surgery	female	30-40	pT2pN+cM0L1V0R1G3 (primary tumor)	G3
B211	G12D	Surgery	male	60-70	ypT3ypN1(3/23)Pn1	-
B226	G12A	FNB	female	60-70	-	-
B250	G12D	Surgery	male	70-80	pT3pN1(1/35)Pn1	G2-3
B253	G12R	FNB	female	70-80	cT4C1cN0C1cM0C1	G2
B273	G12V	Surgery	male	50-60	pT3()C4pN1(1/42)C4cM0C1Pn1	G2
B283	G12D	FNB	male	60-70	ypT1a, ypN0(0/28), Pn1, RX	-
B288	G12V	Surgery	female	80-90	pT2 ( )C4 pN2 (6 /22) C4 cM0 C1 V1	G3
B290	G12V	Surgery	female	70-80	pT1c ( )C4 pN2 (4 /21) C4 cM0 C1 V0 L0	G2
B320	G12D	FNB	male	70-80	-	-
B339	G12D	Surgery	male	60-70	pT3, pN2 (24/33, ECE+), Pn1, V1, CRM	G2
B358	G12V	FNB	female	50-60	-	-
B379	G12D	FNB	male	70-80	pT2, pN1(1/40), Pn1, L1, V1, G2, R1, CRM+	G2
B413	G12V	FNB	male	80-90	-	-
B415	G12R	FNB	male	80-90	-	-
LMU-TM-PO_1.1	G12D	FNB	female	80-90	uT4NxM1	G2
LMU-TM-PO_2.1	G12R	FNB	male	70-80	uT4NxM1	G2
LMU-TM-PO_3.1	G12D	FNB	female	70-80	pT2pN1L0V0Pn1R1	G3
LMU-TM-PO_13.1	G12R	FNB	male	70-80	pT3pN1pM1L1VoPn1	G3

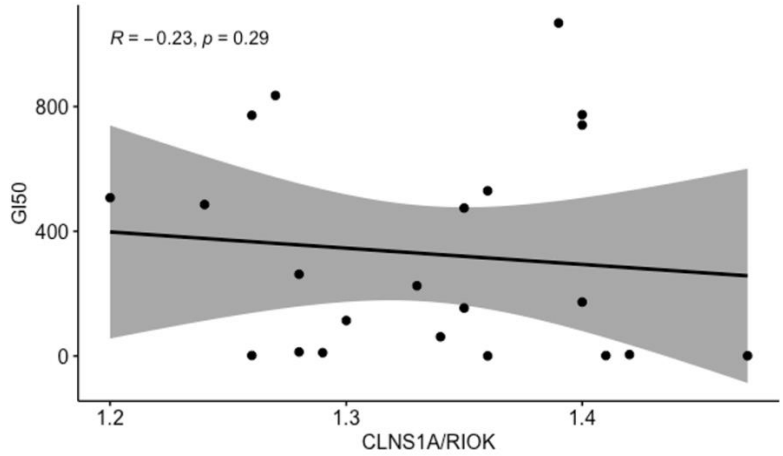

Supplementary Figure 1:

Correlation between the *CLNS1A/RIOK* ratio and the PRMT5i treatment response.

Depicted are the Pearson correlation coefficient and the linear regression in patient-derived organoids (PDO, n=24) between the GI_{50} values after six days of treatment with JNJ-64619178 (max. concentration 1 μM) and the CLNS1A/RIOK mRNA expression ratio based on RNA-seq.

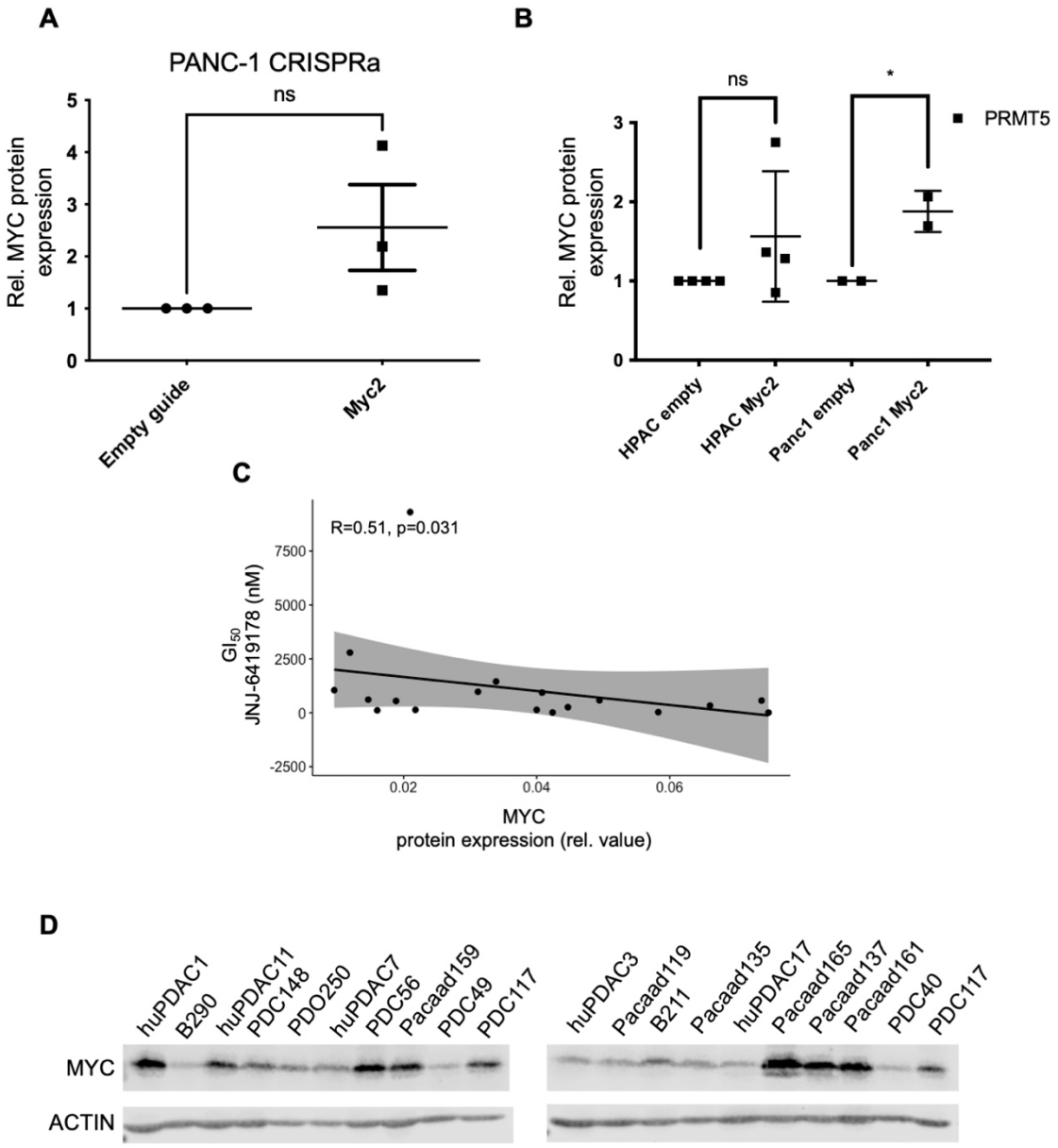

Supplementary Figure 2:

Expression profiles of different cell models.

A) Quantification of MYC protein expression from PANC-1 (n=3). Protein Expression was normalized to the sgRNA empty guide. **B)** Depicted is the Pearson correlation coefficient and the linear regression in patient-derived cell lines (PDCL n=18) between the GI_{50} values after six days of treatment with JNJ-64619178 (max. concentration 1 μM) and *MYC* mRNA expression based on RNA-seq. **C)** MYC protein expression of the 18 PDCLs. ß-ACTIN served as a loading control. One representative experiment out of three is shown.

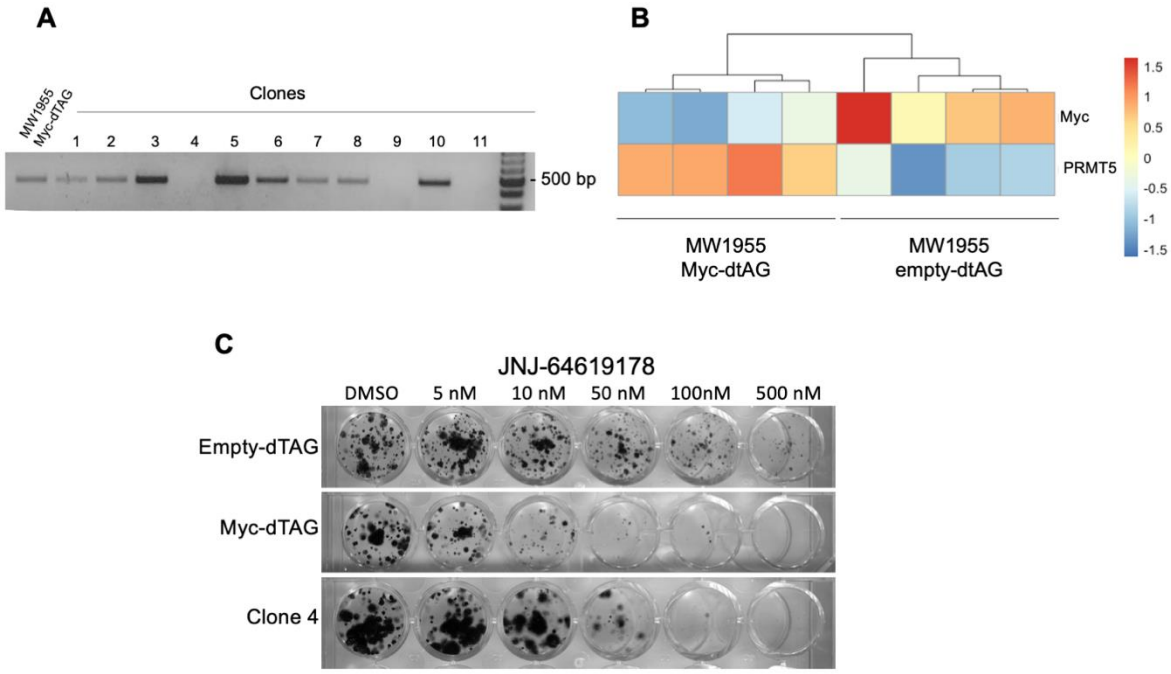

Supplementary Figure 3:

Characterization of the dTAG-system transduced cell lines.

A) PCR-Gel showing the PCR product of the endogenous *MYC* gene of different MW1955 dTAG-Myc clones. No band indicates a deletion of the endogenous *MYC*. **B)** Heatmap showing the *MYC* and *PRMT5* mRNA expression of indicated cell lines based on RNA-seq. **C)** Clonogenic growth assay of depicted JNJ-64619178 treated cell lines with the indicated concentrations. One representative experiment out of three is shown. DMSO was used as vehicle control.

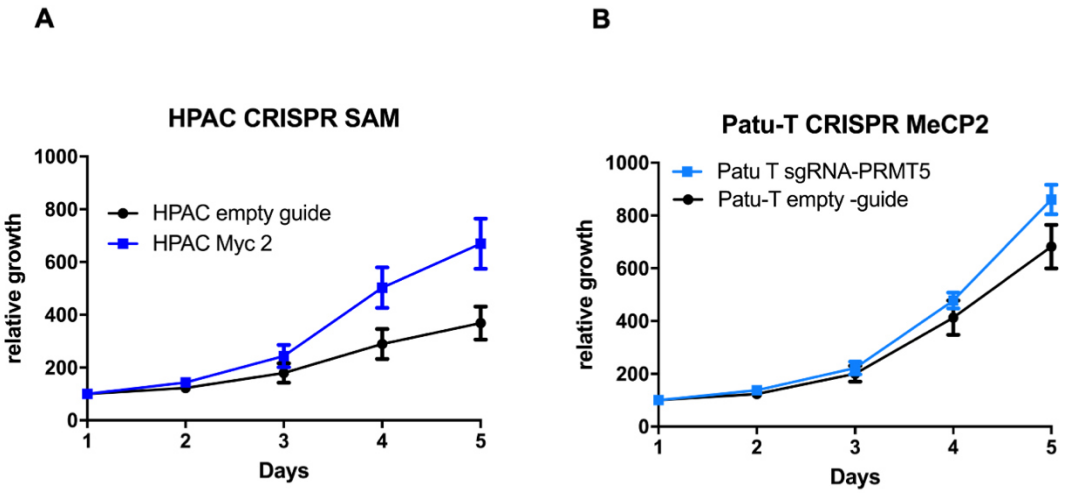

Supplementary Figure 4:

Growth curves of CRISPR cell lines.

Growth curves of **A)** HPAC-MYC-CRISPRa and **B)** PaTu8988T-PRMT5i-CRISPRi cell lines. The growth curves were analyzed from three biological replicates, conducted as three technical replicates. Growth was determined by measuring CTG as a marker for cell proliferation.

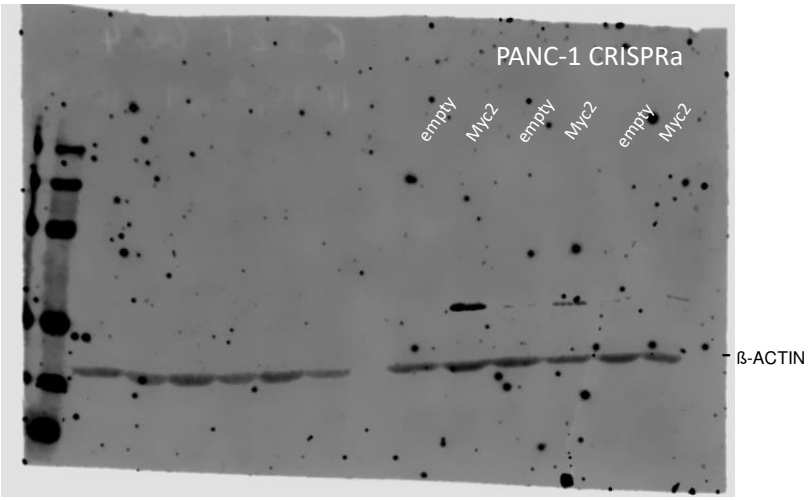

Western Blot 1-1 for Fig. 5A: PANC-1 CRISPRa. Antibody: ß-ACTIN.

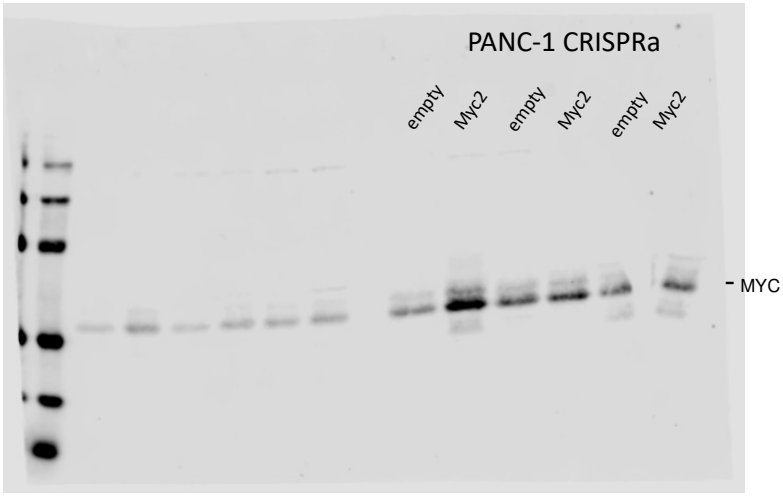

Western blot 1-2 for Fig. 5A: PANC-1 CRISPRa. Antibody: MYC.

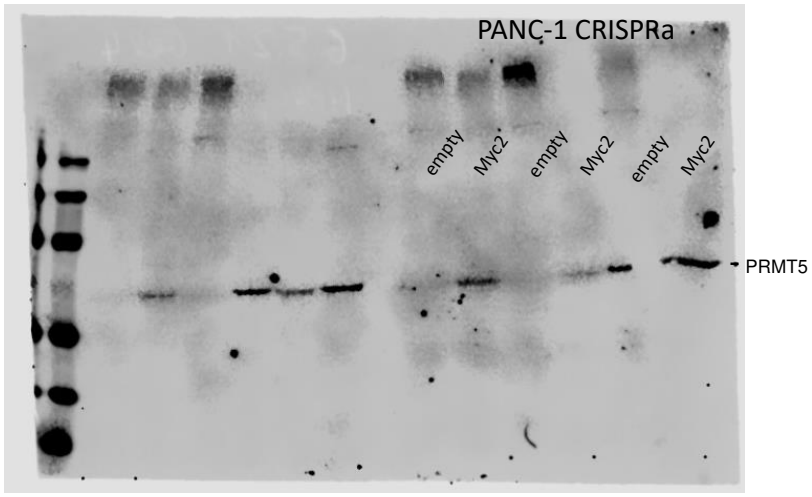

Western blot 1-3 for Fig. 5A: PANC-1 CRISPRa. Antibody: PRMT5.

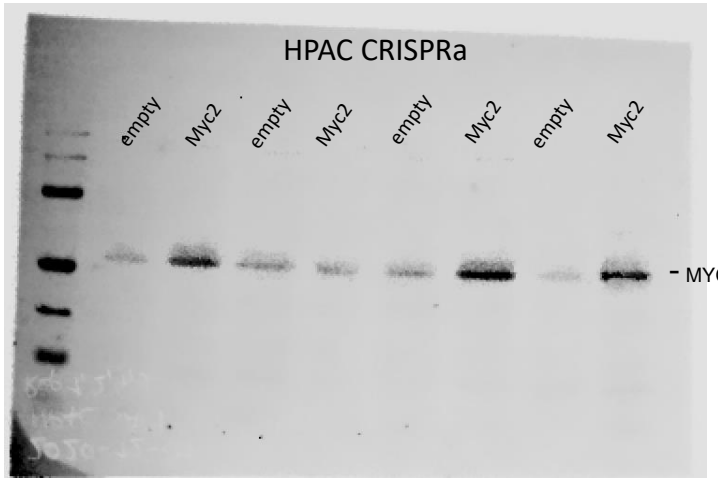

Western blot 2-1 for Fig. 5A: HPAC CRISPRa. Antibody: MYC.

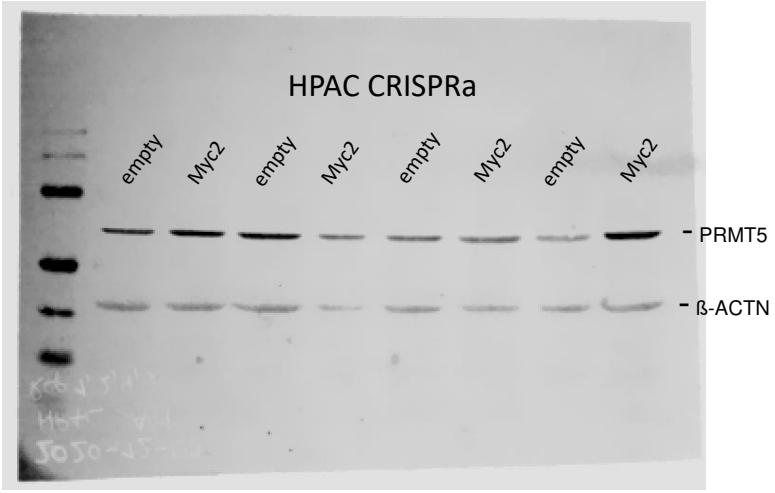

Western blot 2-2 for Fig. 5A: HPAC CRISPRa. Antibody: PRMT5 and ß-ACTIN.

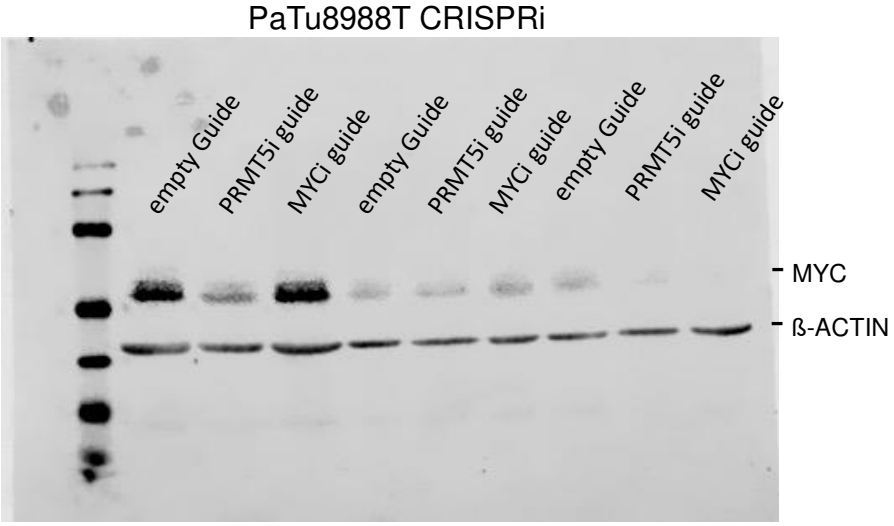

Western blot 3-1 for Fig. 5A: PaTu8988T CRISPRi. Antibody: MYC and ß-ACTIN.

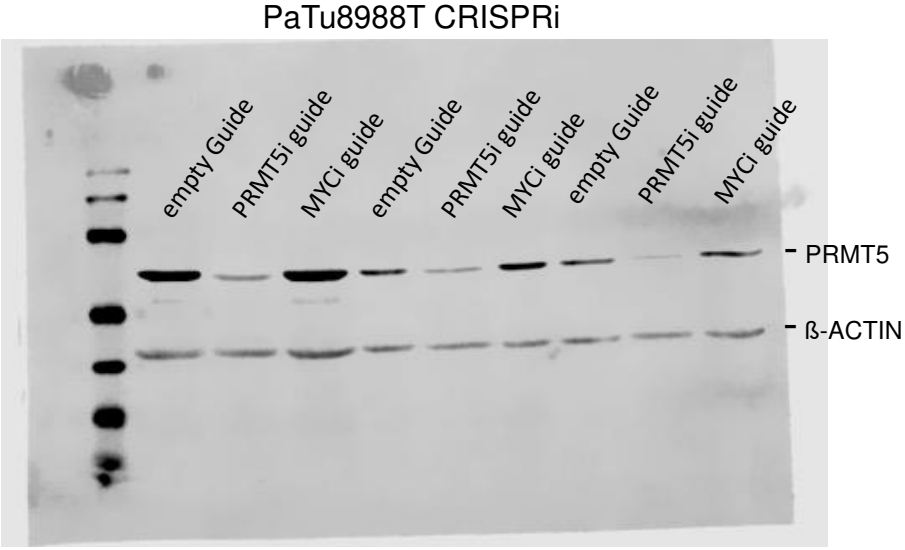

Western blot 3-2 for Fig. 5A: PaTu8988T CRISPRi. Antibody: PRMT5 and ß-ACTIN.

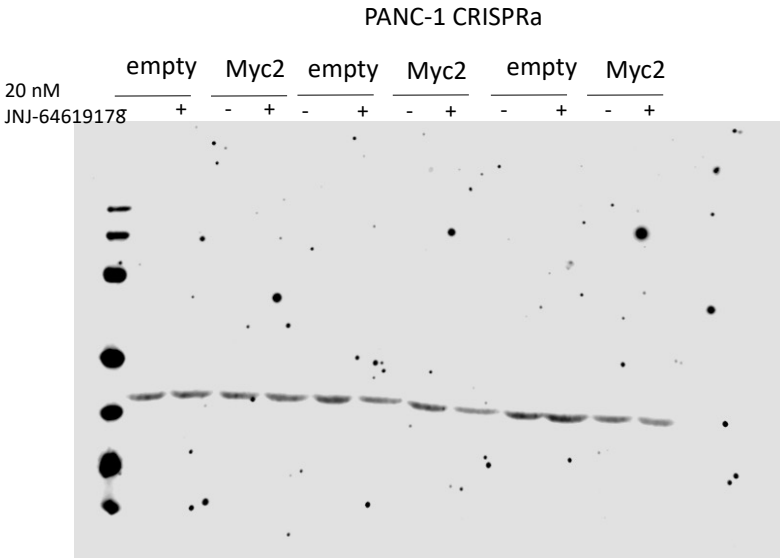

Western blot 4-1 for Fig. 14C: PANC-1 CRISPRa treated with 20 nM JNJ-64619178. Antibody: ß-ACTIN.

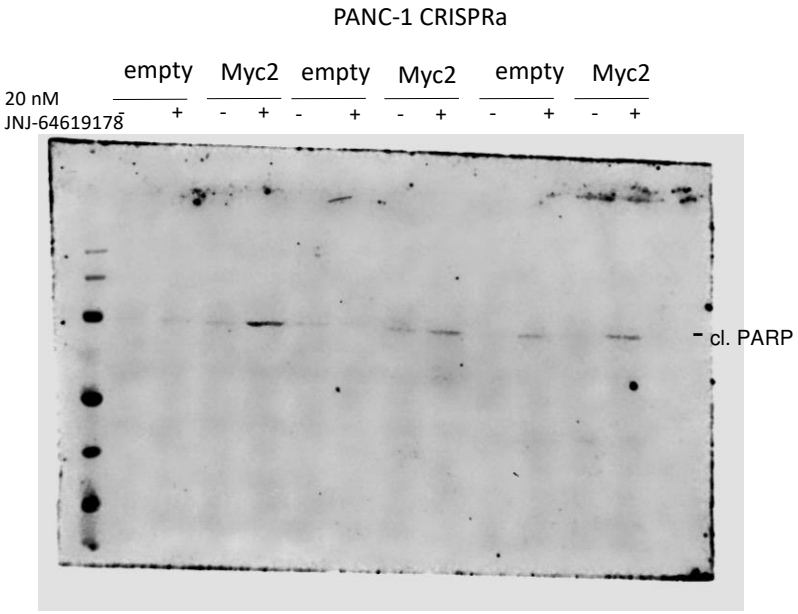

Western blot 4-2 for Fig. 14C: PANC-1 CRISPRa treated with 20 nM JNJ-64619178. Antibody: cleaved PARP.

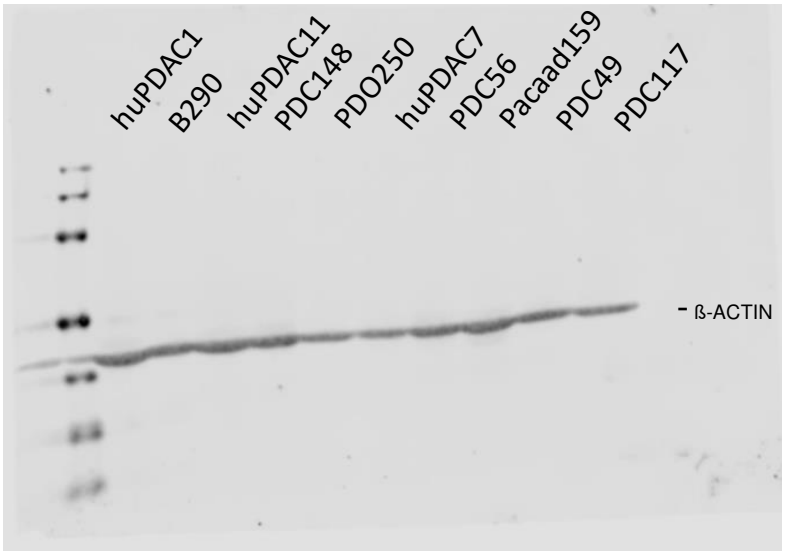

Western blot 5-1 for Fig. 6B: PDCLs. Antibody: ß-ACTIN.

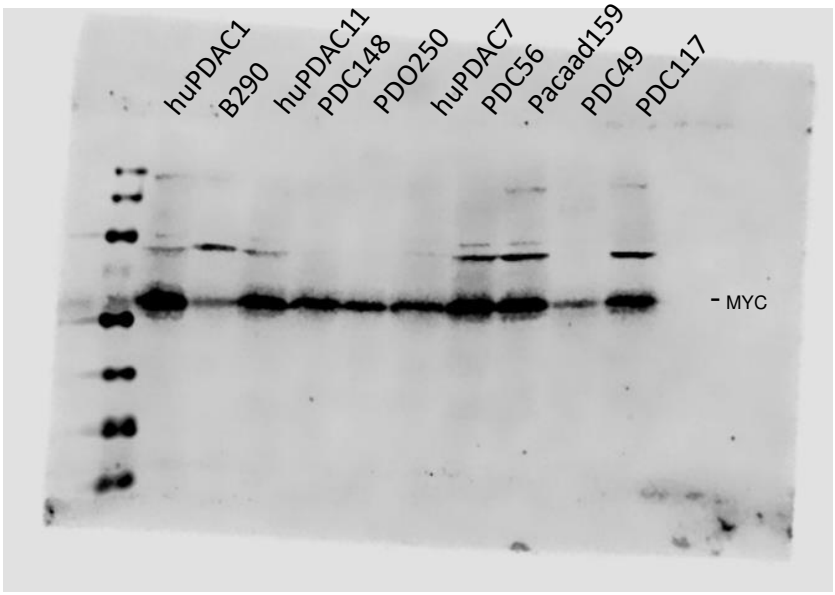

Western blot 5-2 for Fig. 6B: PDCLs. Antibody: MYC.

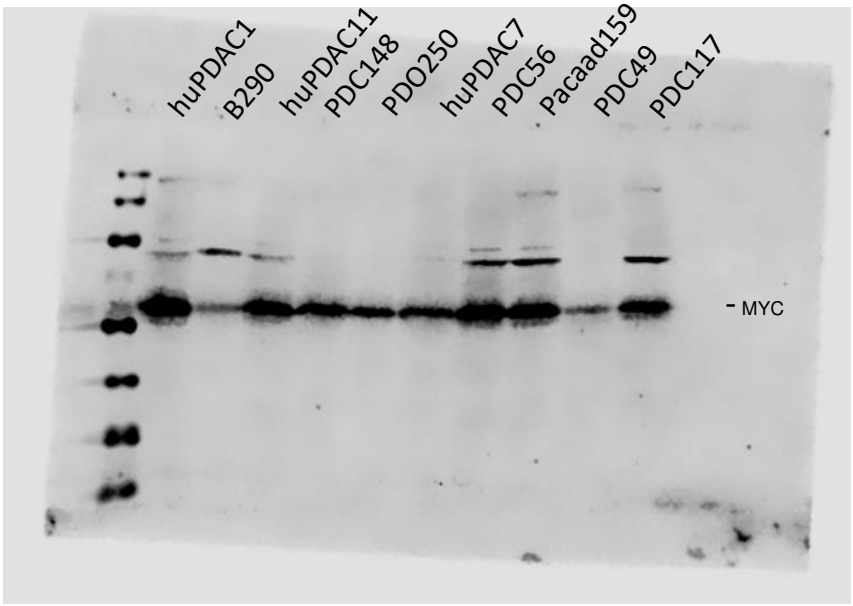

Western blot 6-1 for Fig. 6B: PDCLs. Antibody: ß-ACTIN.

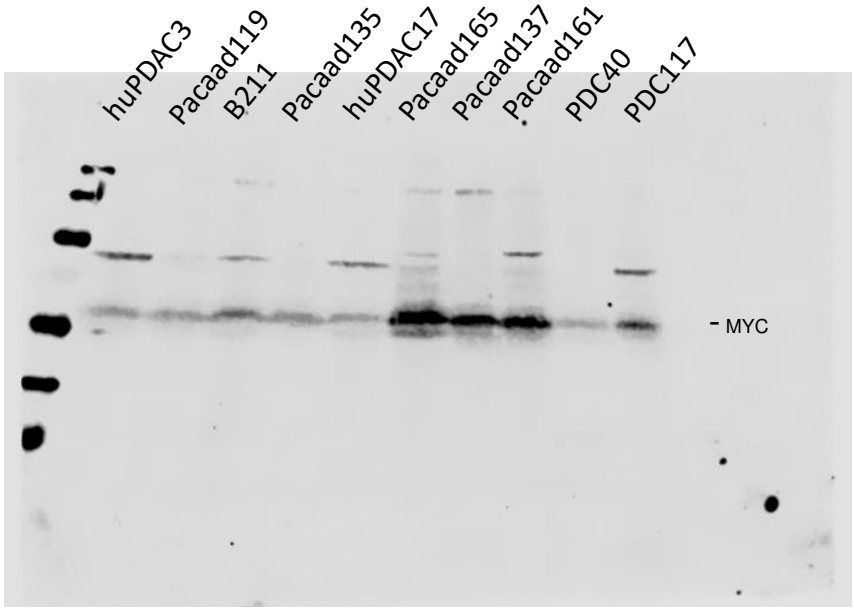

Western blot 6-2 for Fig. 6B: PDCLs. Antibody: MYC.

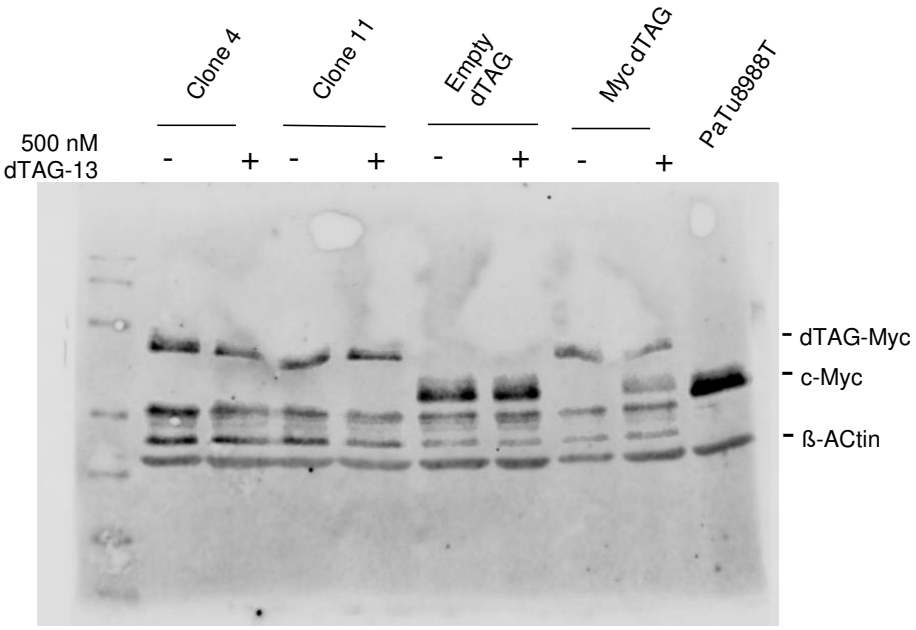

Western blot 7-1 for Fig. 7A: MW1955 cell line treated with 500 nM dTAG-13 or vehicle control. PaTu8988T as control for a line with high endogenous MYC expression. Antibodies: MYC and ß-ACTIN.

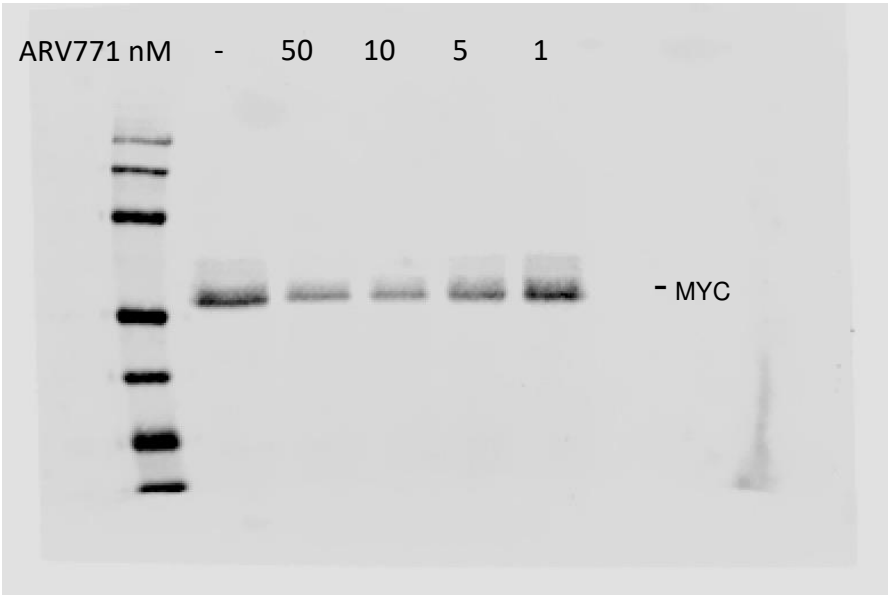

Western blot 8-1 for Fig. 9A: DanG treated for 72h with ARV-771 or vehicle control. Antibody: MYC.

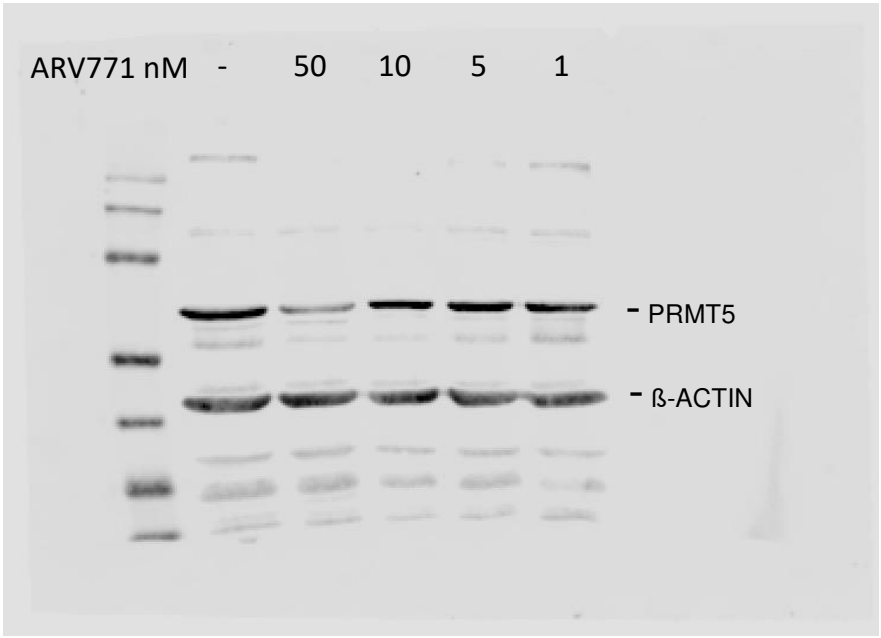

Western blot 8-2 for Fig. 9A: DanG treated for 72h with ARV-771 or vehicle control. Antibody: PRMT5 and ß-ACTIN.

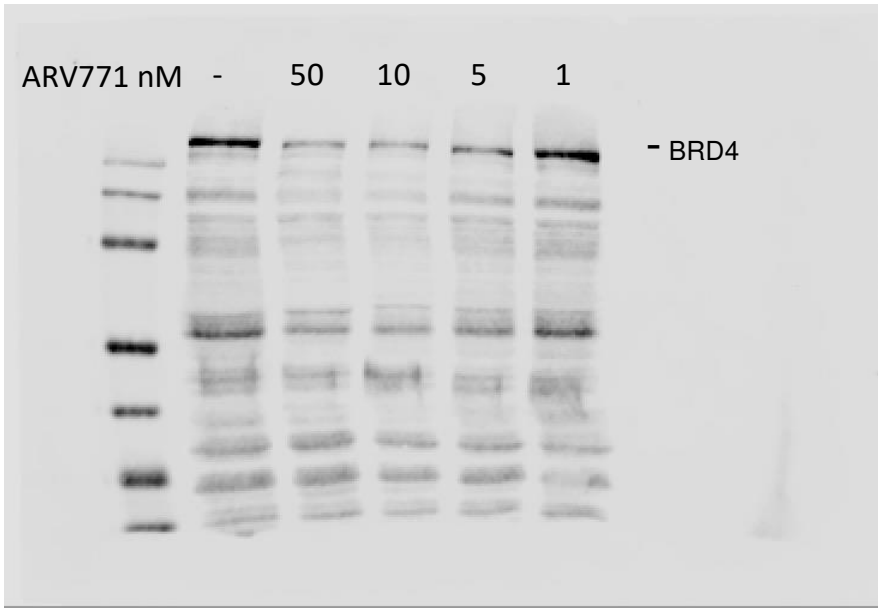

Western blot 8-3 for Fig. 9A: DanG treated for 72h with ARV-771 or vehicle control. Antibody: BRD4.

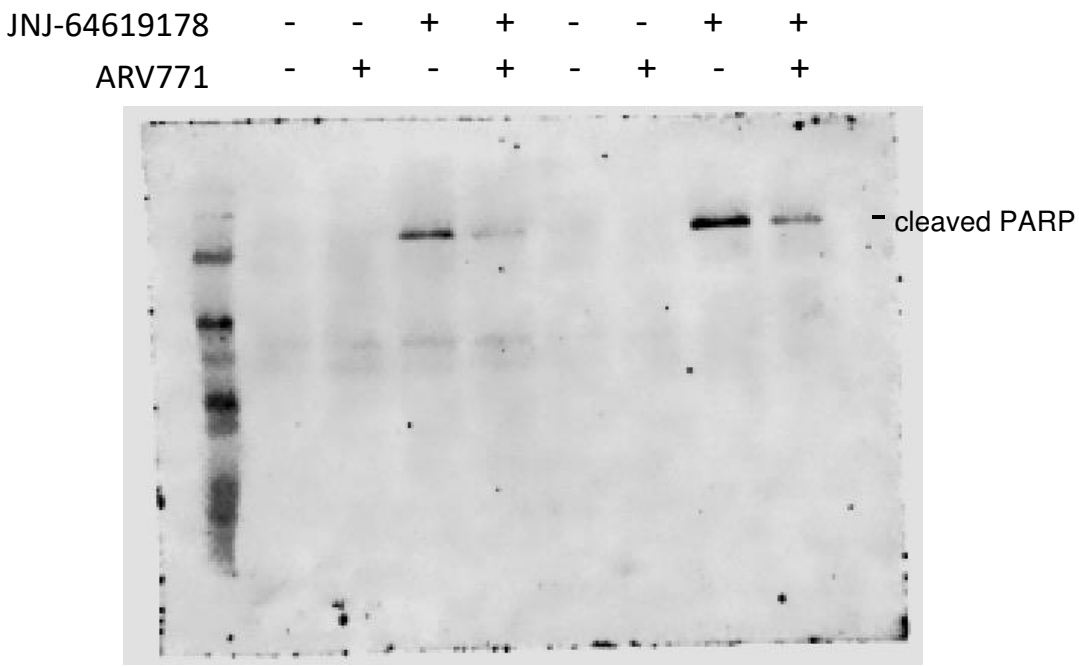

Western blot 9-1 for Fig. 14B: DanG treated for 4 days with 20 nM ARV-771, 20 nM JNJ-64619178 or vehicle control. Antibody: cleaved PARP.

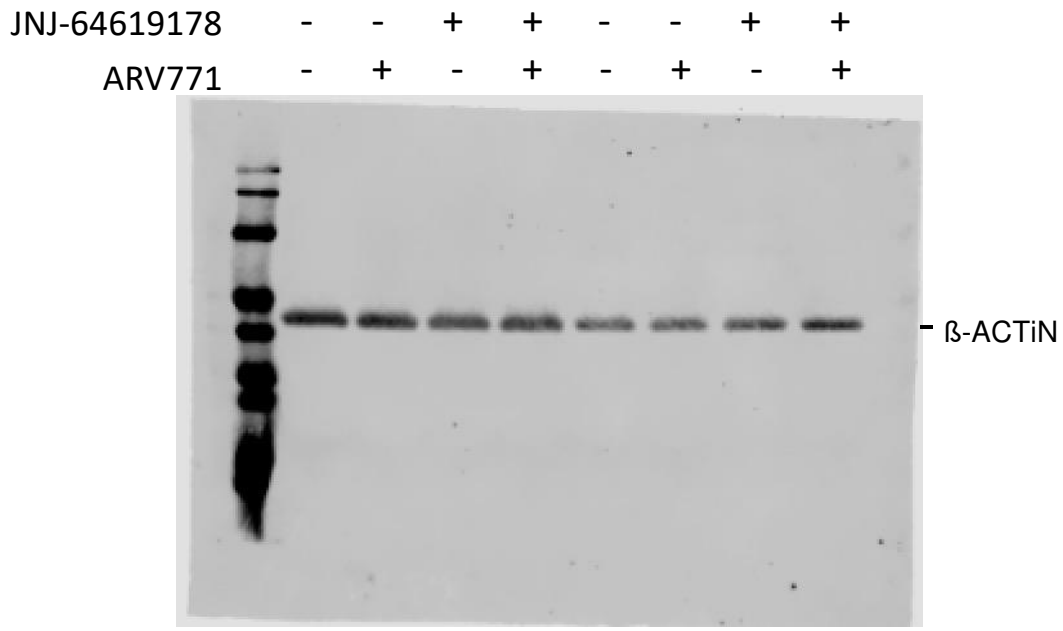

Western blot 9.2 for Fig. 14B: DanG treated for 4 days with 20 nM ARV-771, 20 nM JNJ-64619178 or vehicle control. Antibody: ß-ACTIN.

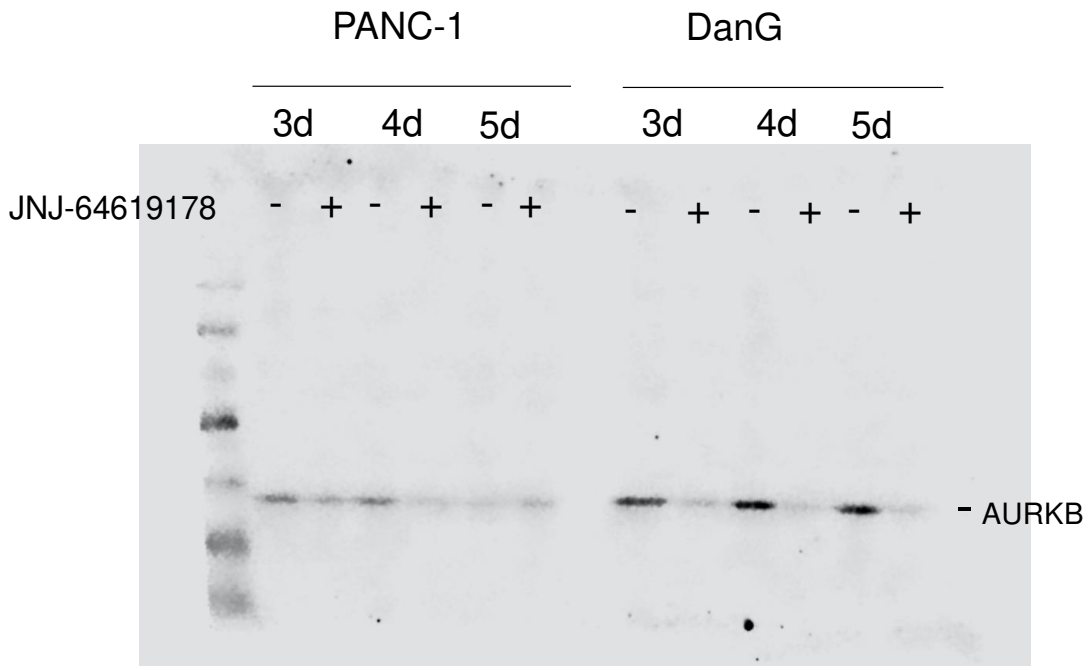

Western Blot 10-1 for Fig. 15B: PANC-1 and DanG cell lines treated with 20 nM JNJ-64619178 for the indicated time-period. Antibody: Aurora kinase B (AURKB).

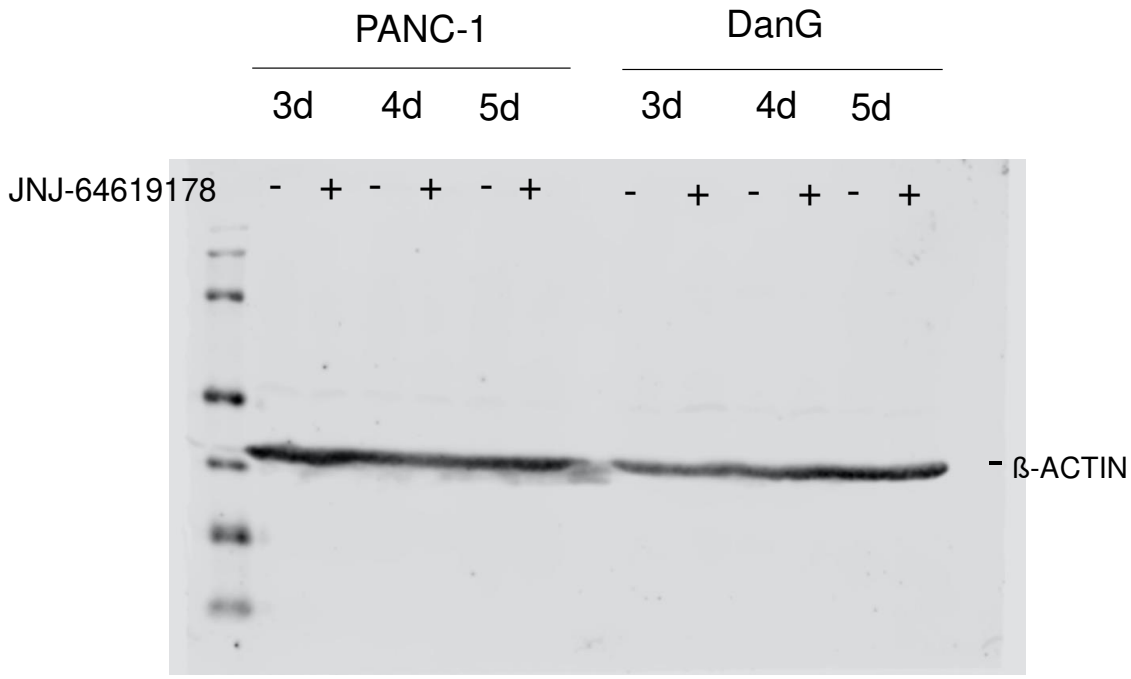

Western Blot 10-2 for Fig. 15B: PANC-1 and DanG cell lines treated with 20 nM JNJ-64619178 for the indicated time-period. Antibody: ß-ACTIN.

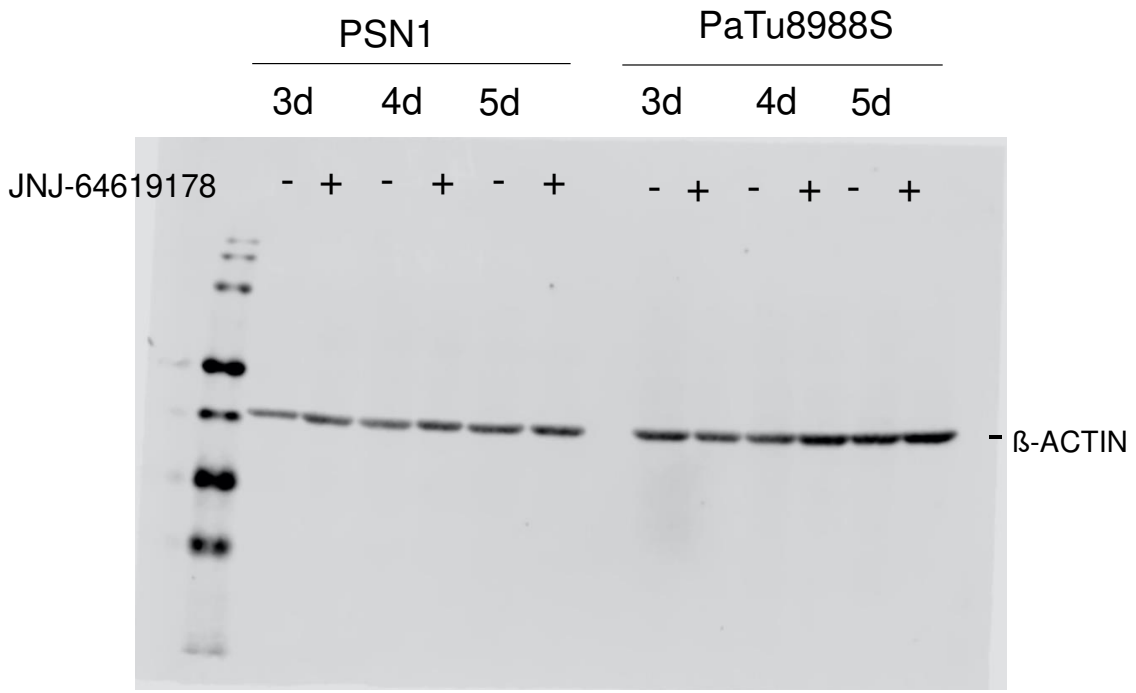

Western Blot 11-1 for Fig. 15B: PSN1 and PaTu8988S cell lines treated with 20 nM JNJ-64619178 for the indicated time-period. Antibody: ß-ACTIN.

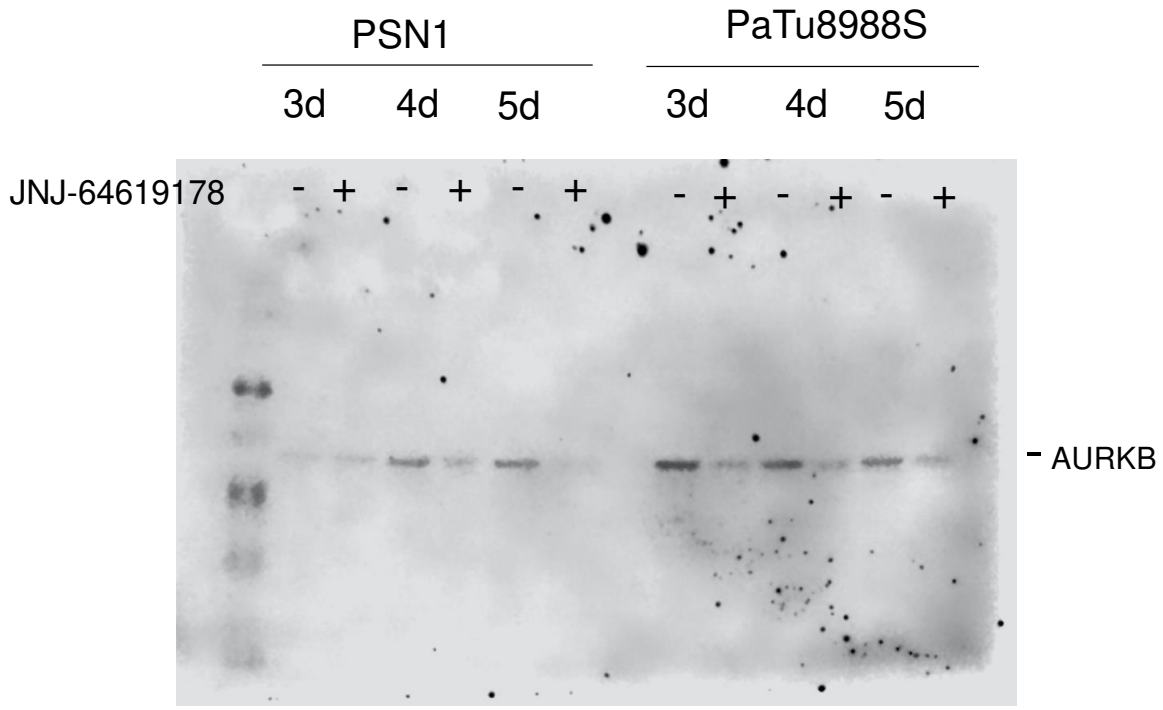

Western Blot 11-2 for Fig. 15B: PSN1 and PaTu8988S cell lines treated with 20 nM JNJ-64619178 for the indicated time-period. Antibody: Aurora kinase B (AURKB).

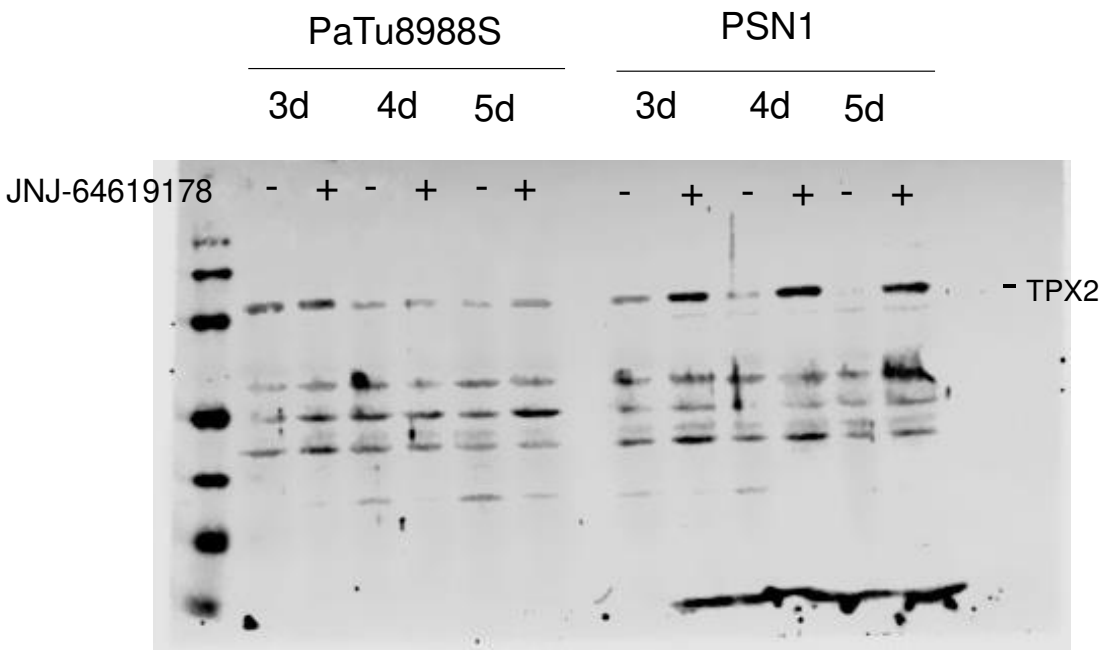

Western Blot 12-1 for Fig. 15C: PaTu8988S and PSN1 cell lines treated with 20 nM JNJ-64619178 for the indicated time-period. Antibody: TPX2.

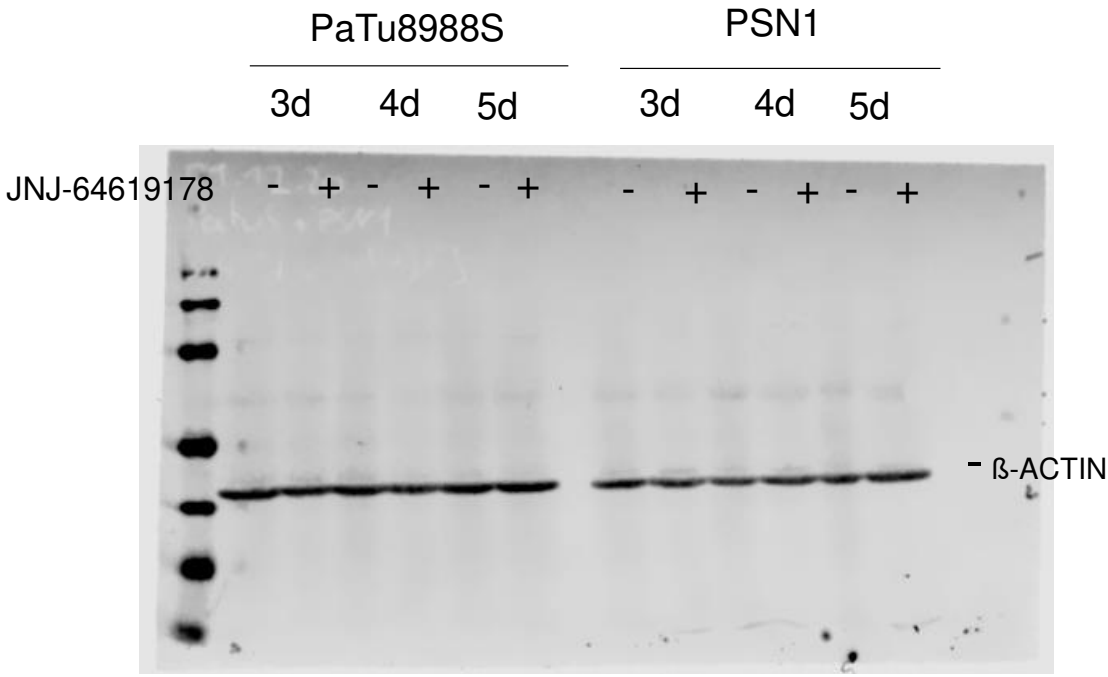

Western Blot 12-2 for Fig. 15C: PaTu8988S and PSN1 cell lines treated with 20 nM JNJ-64619178 for the indicated time-period. Antibody: ß-ACTIN.

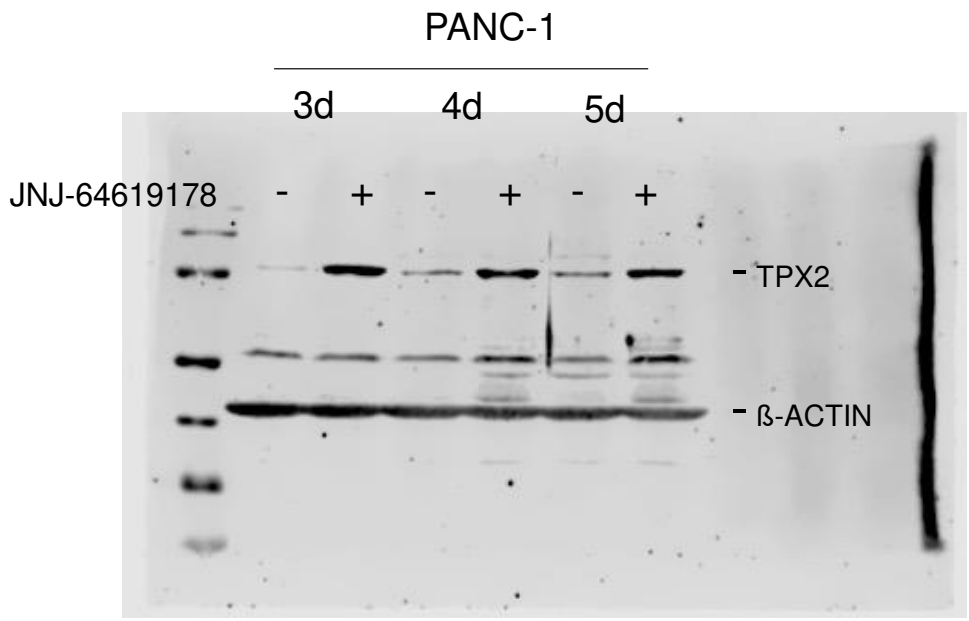

Western Blot 13-1 for Fig. 15C: PANC-1 cell line treated with 20 nM JNJ-64619178 for the indicated time-period. Antibody: TPX2 and ß-ACTIN.

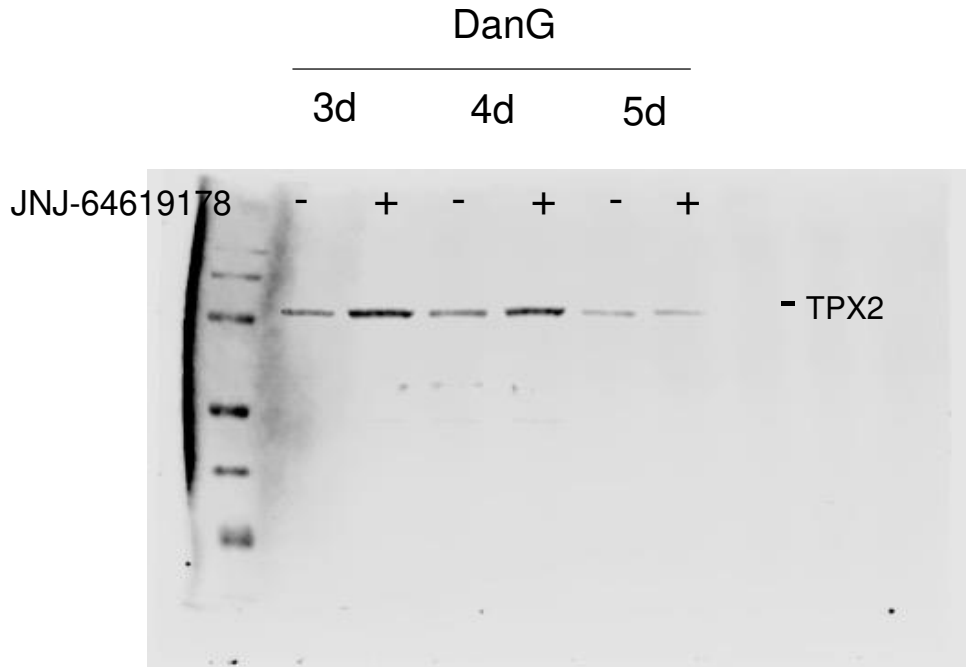

Western Blot 14-1 for Fig. 15C: DanG cell line treated with 20 nM JNJ-64619178 for the indicated time-period. Antibody: TPX2.

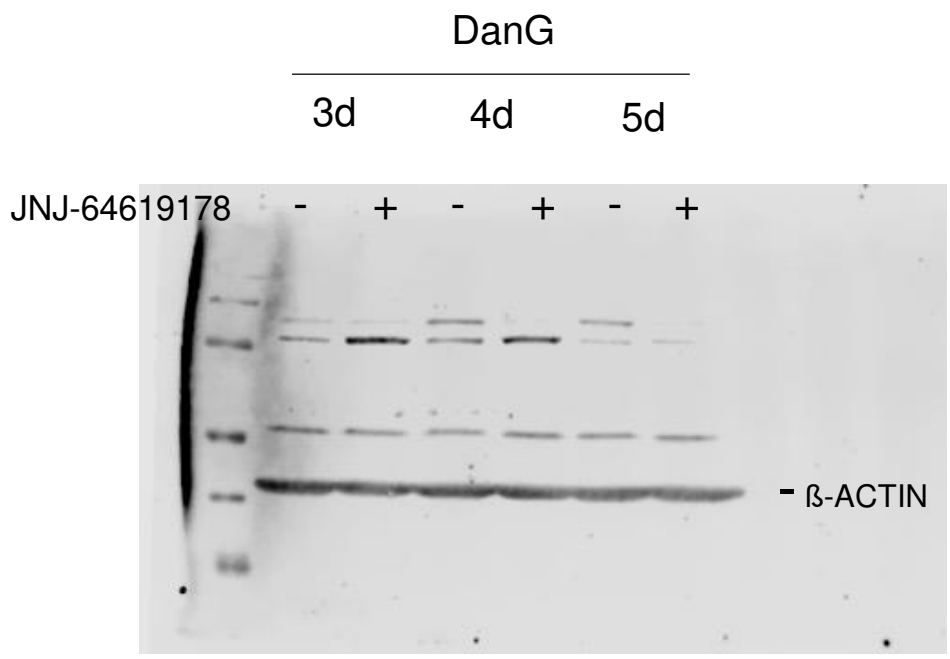

Western Blot 14-2 for Fig. 15C: DanG cell line treated with 20 nM JNJ-64619178 for the indicated time-period. Antibody: ß-ACTIN.

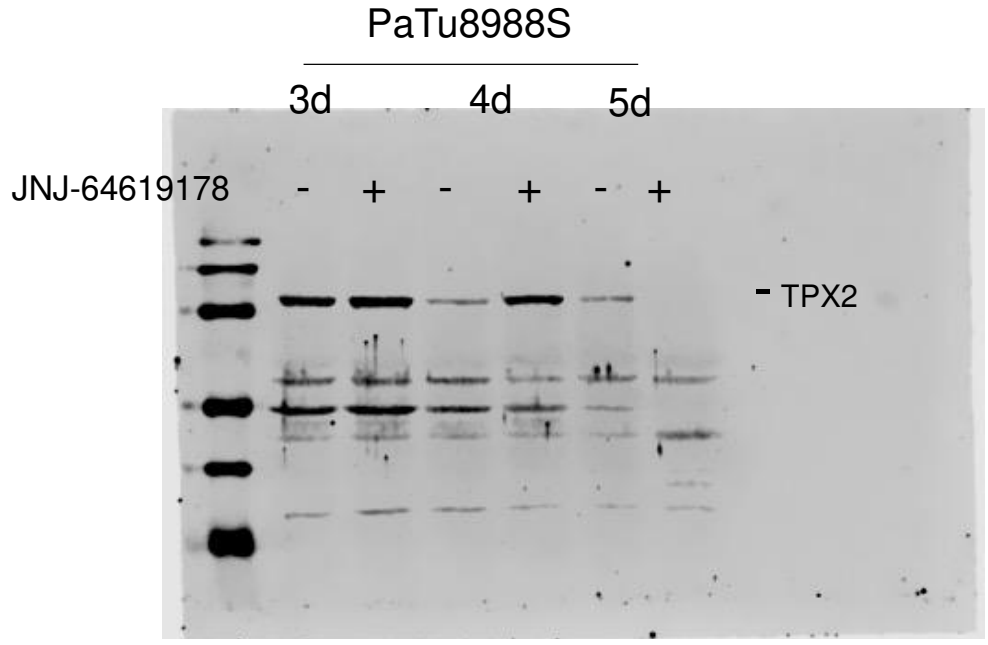

Western Blot 15-1 for Fig. 15C: PaTu8988S cell line treated with 20 nM JNJ-64619178 for the indicated time-period. Antibody: TPX2.

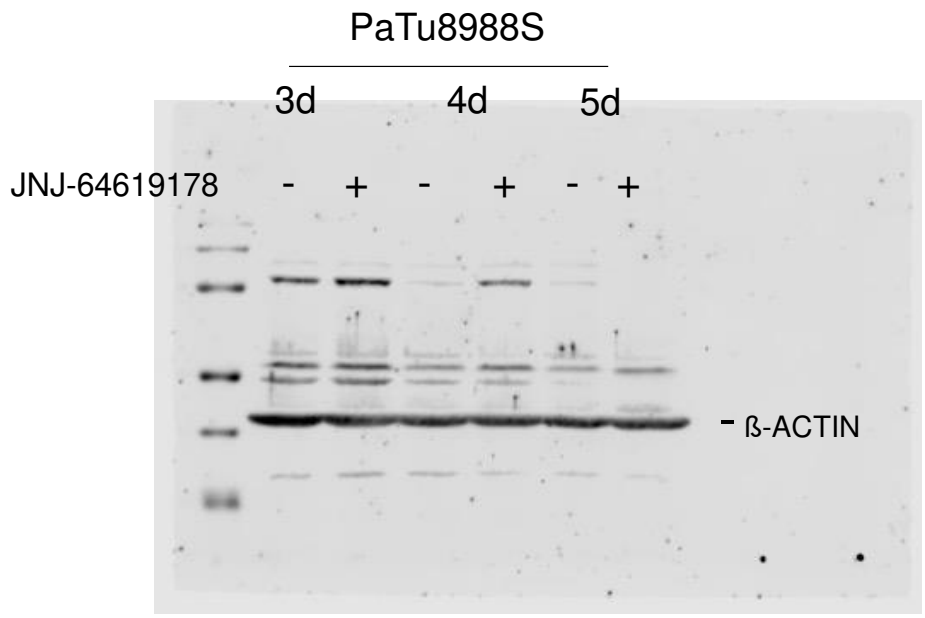

Western Blot 15-2 for Fig. 15C: PaTu8988S cell line treated with 20 nM JNJ-64619178 for the indicated time-period. Antibody: ß-ACTIN.

7. Acknowledgment

First, I want to thank my doctor father Prof. Günter Schneider for the continuous support during my Ph.D. thesis and the opportunity to work in his research group. Thank you for the unique possibility to work in the exciting field of pancreatic cancer research and for your great deal of assistance and support, which resulted in this thesis and my 1st author publication.

I would like to thank my second supervisor Prof. Maximilian Reichert who helped extensively in the organization of the organoid repository, and who always found ways to improve the organoid work.
Additionally, I want to thank my third supervisor Prof. Rainer Glaß, who offered me support during my thesis advisory committee meetings and helped me to guide my thesis in the correct direction to successfully complete it.

Furthermore, I would like to thank my collaborators in AG Saur, AG Rad, AG Reichert, AG Küster at the TUM, and AG Beyer at the LMU for all their interdisciplinary expertise.

Especially I want to acknowledge the help of all my coworkers. The inspiring atmosphere and stimulating discussions helped me a lot to stay motivated throughout the years.

Special thanks are owed to my family and my girlfriend who supported me throughout my studies with continuous encouragement and were always there in need.

Finally, I want to thank the patients who donated tumor material for my research. I hope that your donation to my work will improve the future therapy for patients with pancreatic cancer.

VII. References

1. Rahib L, Smith BD, Aizenberg R, Rosenzweig AB, Fleshman JM, Matrisian LM. Projecting Cancer Incidence and Deaths to 2030: The Unexpected Burden of Thyroid, Liver, and Pancreas Cancers in the United States. *Cancer Res*. 2014;74(11):2913 LP - 2921. doi:10.1158/0008-5472.CAN-14-0155
2. Siegel RL, Miller KD, Jemal A. Cancer statistics, 2019. *CA Cancer J Clin*. 2019;69(1):7-34. doi:https://doi.org/10.3322/caac.21551
3. Bray F, Ferlay J, Soerjomataram I, Siegel RL, Torre LA, Jemal A. Global cancer statistics 2018: GLOBOCAN estimates of incidence and mortality worldwide for 36 cancers in 185 countries. *CA Cancer J Clin*. 2018;68(6):394-424. doi:https://doi.org/10.3322/caac.21492
4. Carioli G, Bertuccio P, Boffetta P, et al. European cancer mortality predictions for the year 2020 with a focus on prostate cancer. *Ann Oncol*. 2020;31(5):650-658. doi:10.1016/j.annonc.2020.02.009
5. Fidler MM, Bray F, Soerjomataram I. The global cancer burden and human development: A review. *Scand J Public Health*. 2017;46(1):27-36. doi:10.1177/1403494817715400
6. McGuigan A, Kelly P, Turkington RC, Jones C, Coleman HG, McCain RS. Pancreatic cancer: A review of clinical diagnosis, epidemiology, treatment and outcomes. *World J Gastroenterol*. 2018;24(43):4846-4861. doi:10.3748/wjg.v24.i43.4846
7. Hidalgo M, Cascinu S, Kleeff J, et al. Addressing the challenges of pancreatic cancer: Future directions for improving outcomes. *Pancreatology*. 2015;15(1):8-18. doi:https://doi.org/10.1016/j.pan.2014.10.001
8. Quante AS, Ming C, Rottmann M, et al. Projections of cancer incidence and cancer-related deaths in Germany by 2020 and 2030. *Cancer Med*. 2016;5(9):2649-2656. doi:https://doi.org/10.1002/cam4.767
9. Capasso M, Franceschi M, Rodriguez-Castro KI, et al. Epidemiology and risk factors of pancreatic cancer. *Acta Biomed*. 2018;89(2):141-146. doi:10.23750/abm.v89i9-S.7923
10. Ilic M, Ilic I. Epidemiology of pancreatic cancer. *World J Gastroenterol*. 2016;22(44):9694-9705. doi:10.3748/wjg.v22.i44.9694
11. Heinemann V, Boeck S. Perioperative management of pancreatic cancer. *Ann Oncol*. 2008;19:vii273-vii278. doi:https://doi.org/10.1093/annonc/mdn450
12. Janssen QP, O'Reilly EM, van Eijck CHJ, Groot Koerkamp B. Neoadjuvant Treatment in Patients With Resectable and Borderline Resectable Pancreatic Cancer. *Front Oncol*. 2020;10(January):1-13. doi:10.3389/fonc.2020.00041
13. Tempero MA, Malafa MP, Al-Hawary M, et al. Pancreatic Adenocarcinoma, Version 2.2017, NCCN Clinical Practice Guidelines in Oncology. *J Natl Compr Cancer Netw J Natl Compr Canc Netw*. 2017;15(8):1028-1061. doi:10.6004/jnccn.2017.0131
14. Scheufele F, Hartmann D, Friess H. Treatment of pancreatic cancer—neoadjuvant treatment in borderline resectable/locally advanced pancreatic cancer. *Transl Gastroenterol Hepatol*. 2019;4(May). doi:10.21037/tgh.2019.04.09
15. Huang L, Jansen L, Balavarca Y, et al. Resection of pancreatic cancer in Europe and USA: an international large-scale study highlighting large variations. *Gut*. 2019;68(1):130 LP - 139. doi:10.1136/gutjnl-2017-314828
16. Del Chiaro M, Rangelova E, Halimi A, et al. Pancreatectomy with arterial

resection is superior to palliation in patients with borderline resectable or locally advanced pancreatic cancer. *HPB*. 2019;21(2):219-225. doi:https://doi.org/10.1016/j.hpb.2018.07.017
17. Gourgou-bourgade S, Sc M, Fouchardière C De, et al. FOLFIRINOX versus Gemcitabine for Metastatic Pancreatic Cancer. 2011:1817-1825.
18. Lehmann BD, Shyr Y, Pietenpol JA, et al. Identification of human triple-negative breast cancer subtypes and preclinical models for selection of targeted therapies. 2011;121(7):2750-2767. doi:10.1172/JCI45014.2750
19. Huang A, Yang X-R, Chung W-Y, Dennison AR, Zhou J. Targeted therapy for hepatocellular carcinoma. *Signal Transduct Target Ther*. 2020;5(1):146. doi:10.1038/s41392-020-00264-x
20. Chan-Seng-Yue M, Kim JC, Wilson GW, et al. Transcription phenotypes of pancreatic cancer are driven by genomic events during tumor evolution. *Nat Genet*. 2020;52(2):231-240. doi:10.1038/s41588-019-0566-9
21. Schneider G, Schmidt-Supprian M, Rad R, Saur D. Tissue-specific tumorigenesis: context matters. *Nat Rev Cancer*. 2017;17(4):239-253. doi:10.1038/nrc.2017.5
22. Murphy SJ, Hart SN, Lima JF, et al. Genetic Alterations Associated With Progression From Pancreatic Intraepithelial Neoplasia to Invasive Pancreatic Tumor. *Gastroenterology*. 2013;145(5):1098-1109.e1. doi:https://doi.org/10.1053/j.gastro.2013.07.049
23. Hruban RH, Maitra A, Kern SE, Goggins M. Precursors to Pancreatic Cancer. *Gastroenterol Clin North Am*. 2007;36(4):831-849. doi:https://doi.org/10.1016/j.gtc.2007.08.012
24. Macgregor-das AM. Molecular Pathways in Pancreatic Carcinogenesis. 2013;(June 2012):8-14. doi:10.1002/jso.23213
25. Hruban RH, Adsay NV, Albores–Saavedra J, et al. Pancreatic Intraepithelial Neoplasia: A New Nomenclature and Classification System for Pancreatic Duct Lesions. *Am J Surg Pathol*. 2001;25(5). https://journals.lww.com/ajsp/Fulltext/2001/05000/Pancreatic_Intraepithelial_Neoplasia__A_New.3.aspx.
26. Distler M, Aust D, Weitz J, Pilarsky C, Grützmann R. Precursor Lesions for Sporadic Pancreatic Cancer : PanIN , IPMN , and MCN. 2014;2014(Figure 2). doi:10.1155/2014/474905
27. Basturk O, Hong S-M, Wood LD, et al. A Revised Classification System and Recommendations From the Baltimore Consensus Meeting for Neoplastic Precursor Lesions in the Pancreas. *Am J Surg Pathol*. 2015;39(12):1730-1741. doi:10.1097/PAS.0000000000000533
28. Maitra A, Fukushima N, Takaori K, Hruban RH. Precursors to Invasive Pancreatic Cancer. *Adv Anat Pathol*. 2005;12(2). https://journals.lww.com/anatomicpathology/Fulltext/2005/03000/Precursors_to_Invasive_Pancreatic_Cancer.6.aspx.
29. Hata T, Suenaga M, Marchionni L, et al. Genome-Wide Somatic Copy Number Alterations and Mutations in High-Grade Pancreatic Intraepithelial Neoplasia. *Am J Pathol*. 2018;188(7):1723-1733. doi:https://doi.org/10.1016/j.ajpath.2018.03.012
30. Hessmann E, Schneider G, Ellenrieder V, Siveke JT. MYC in pancreatic cancer: novel mechanistic insights and their translation into therapeutic strategies. *Oncogene*. 2016;35(13):1609-1618. doi:10.1038/onc.2015.216
31. Skoudy A, Hernández-Muñoz I, Navarro P. Pancreatic ductal adenocarcinoma and transcription factors: Role of c-Myc. *J Gastrointest Cancer*. 2011;42(2):76-

84. doi:10.1007/s12029-011-9258-0
32. Dang C V, Reddy EP, Shokat KM, Soucek L. Drugging the “undruggable” cancer targets. *Nat Rev Cancer*. 2017;17(8):502-508. doi:10.1038/nrc.2017.36
33. Duffy MJ, Crown J. Drugging “undruggable” genes for cancer treatment: Are we making progress? *Int J Cancer*. 2021;148(1):8-17. doi:https://doi.org/10.1002/ijc.33197
34. Wirth M, Mahboobi S, Krämer OH, Schneider G. Concepts to Target MYC in Pancreatic Cancer. *Mol Cancer Ther*. 2016;15(8):1792 LP - 1798. doi:10.1158/1535-7163.MCT-16-0050
35. Bailey P, Chang DK, Nones K, et al. Genomic analyses identify molecular subtypes of pancreatic cancer. *Nature*. 2016;531(7592):47-52. doi:10.1038/nature16965
36. Yachida S, Jones S, Bozic I, et al. Distant metastasis occurs late during the genetic evolution of pancreatic cancer. *Nature*. 2010;467(7319):1114-1117. doi:10.1038/nature09515
37. Campbell PJ, Yachida S, Mudie LJ, et al. The patterns and dynamics of genomic instability in metastatic pancreatic cancer. *Nature*. 2010;467(7319):1109-1113. doi:10.1038/nature09460
38. Kanno A, Masamune A, Hanada K, Kikuyama M, Kitano M. Advances in Early Detection of Pancreatic Cancer. *Diagnostics (Basel, Switzerland)*. 2019;9(1):18. doi:10.3390/diagnostics9010018
39. Dang C V, O’Donnell KA, Zeller KI, Nguyen T, Osthus RC, Li F. The c-Myc target gene network. *Semin Cancer Biol*. 2006;16(4):253-264. doi:https://doi.org/10.1016/j.semcancer.2006.07.014
40. Grandori C, Cowley SM, James LP, Eisenman RN. The Myc/Max/Mad Network and the Transcriptional Control of Cell Behavior. *Annu Rev Cell Dev Biol*. 2000;16(1):653-699. doi:10.1146/annurev.cellbio.16.1.653
41. Walhout AJM, Gubbels JM, Bernards R, van der Vliet PC, Timmers HTM. c-Myc/Max Heterodimers Bind Cooperatively to the E-Box Sequences Located in the First Intron of the Rat Ornithine Decarboxylase (ODC) Gene. *Nucleic Acids Res*. 1997;25(8):1493-1501. doi:10.1093/nar/25.8.1493
42. Pelengaris S, Khan M, Evan G. c-MYC: more than just a matter of life and death. *Nat Rev Cancer*. 2002;2(10):764-776. doi:10.1038/nrc904
43. Sodir NM, Kortlever RM, Barthet VJA, et al. MYC Instructs and Maintains Pancreatic Adenocarcinoma Phenotype. *Cancer Discov*. 2020;10(4):588 LP - 607. doi:10.1158/2159-8290.CD-19-0435
44. Dang C V. c-Myc Target Genes Involved in Cell Growth, Apoptosis, and Metabolism. *Mol Cell Biol*. 1999;19(1):1-11. doi:10.1128/mcb.19.1.1
45. Bretones G, Delgado MD, León J. Myc and cell cycle control. *Biochim Biophys Acta - Gene Regul Mech*. 2015;1849(5):506-516. doi:https://doi.org/10.1016/j.bbagrm.2014.03.013
46. Meyer N, Penn LZ. Reflecting on 25 years with MYC. *Nat Rev Cancer*. 2008;8(12):976-990. doi:10.1038/nrc2231
47. García-Gutiérrez L, Delgado MD, León J. Myc oncogene contributions to release of cell cycle brakes. *Genes (Basel)*. 2019;10(3). doi:10.3390/genes10030244
48. McMahon SB. MYC and the control of apoptosis. *Cold Spring Harb Perspect Med*. 2014;4(7):1-9. doi:10.1101/cshperspect.a014407
49. Kalkat M, De Melo J, Hickman KA, et al. MYC deregulation in primary human cancers. *Genes (Basel)*. 2017;8(6):2-30. doi:10.3390/genes8060151
50. Beroukhim R, Mermel CH, Porter D, et al. The landscape of somatic copy-

number alteration across human cancers. *Nature*. 2010;463(7283):899-905. doi:10.1038/nature08822
51. Witkiewicz AK, McMillan EA, Balaji U, et al. Whole-exome sequencing of pancreatic cancer defines genetic diversity and therapeutic targets. *Nat Commun*. 2015;6:1-11. doi:10.1038/ncomms7744
52. Lenkiewicz E, Malasi S, Hogenson TL, et al. Genomic and Epigenomic Landscaping Defines New Therapeutic Targets for Adenosquamous Carcinoma of the Pancreas. *Cancer Res*. 2020;80(20):4324 LP - 4334. doi:10.1158/0008-5472.CAN-20-0078
53. Biederstädt A, Hassan Z, Schneeweis C, et al. SUMO pathway inhibition targets an aggressive pancreatic cancer subtype. *Gut*. 2020;69(8):1472 LP - 1482. doi:10.1136/gutjnl-2018-317856
54. Bian B, Juiz NA, Gayet O, et al. Pancreatic Cancer Organoids for Determining Sensitivity to Bromodomain and Extra-Terminal Inhibitors (BETi) . *Front Oncol* . 2019;9:475. https://www.frontiersin.org/article/10.3389/fonc.2019.00475.
55. DOBZHANSKY T. Genetics of natural populations; recombination and variability in populations of Drosophila pseudoobscura. *Genetics*. 1946;31(3):269-290. https://pubmed.ncbi.nlm.nih.gov/20985721.
56. Thng DKH, Toh TB, Chow EK-H. Capitalizing on Synthetic Lethality of MYC to Treat Cancer in the Digital Age. *Trends Pharmacol Sci*. 2021;42(3):166-182. doi:10.1016/j.tips.2020.11.014
57. Bedford MT, Clarke SG. Protein Arginine Methylation in Mammals: Who, What, and Why. *Mol Cell*. 2009;33(1):1-13. doi:https://doi.org/10.1016/j.molcel.2008.12.013
58. Xiao W, Chen X, Liu L, Shu Y, Zhang M, Zhong Y. Role of protein arginine methyltransferase 5 in human cancers. *Biomed Pharmacother*. 2019;114:108790. doi:https://doi.org/10.1016/j.biopha.2019.108790
59. Guccione E, Richard S. The regulation, functions and clinical relevance of arginine methylation. *Nat Rev Mol Cell Biol*. 2019;20(10):642-657. doi:10.1038/s41580-019-0155-x
60. Di Lorenzo A, Bedford MT. Histone arginine methylation. *FEBS Lett*. 2011;585(13):2024-2031. doi:10.1016/j.febslet.2010.11.010
61. Yang Y, Hadjikyriacou A, Xia Z, et al. PRMT9 is a Type II methyltransferase that methylates the splicing factor SAP145. *Nat Commun*. 2015;6(1):6428. doi:10.1038/ncomms7428
62. Tewary SK, Zheng YG, Ho M-C. Protein arginine methyltransferases: insights into the enzyme structure and mechanism at the atomic level. *Cell Mol Life Sci*. 2019;76(15):2917-2932. doi:10.1007/s00018-019-03145-x
63. Nie M, Wang Y, Guo C, et al. CARM1-mediated methylation of protein arginine methyltransferase 5 represses human γ-globin gene expression in erythroleukemia cells. *J Biol Chem*. 2018;293(45):17454-17463. doi:10.1074/jbc.RA118.004028
64. Limm K, Wallner S, Milenkovic VM, Wetzel CH, Bosserhoff A-K. The metabolite 5′-methylthioadenosine signals through the adenosine receptor A2B in melanoma. *Eur J Cancer*. 2014;50(15):2714-2724. doi:https://doi.org/10.1016/j.ejca.2014.07.005
65. Marjon K, Cameron MJ, Quang P, et al. MTAP Deletions in Cancer Create Vulnerability to Targeting of the MAT2A/PRMT5/RIOK1 Axis. *Cell Rep*. 2016;15(3):574-587. doi:10.1016/j.celrep.2016.03.043
66. Chiang K, Zielinska AE, Shaaban AM, et al. PRMT5 Is a Critical Regulator of Breast Cancer Stem Cell Function via Histone Methylation and FOXP1

Expression. *Cell Rep*. 2017;21(12):3498-3513. doi:10.1016/j.celrep.2017.11.096
67. Hamard P-J, Santiago GE, Liu F, et al. PRMT5 Regulates DNA Repair by Controlling the Alternative Splicing of Histone-Modifying Enzymes. *Cell Rep*. 2018;24(10):2643-2657. doi:10.1016/j.celrep.2018.08.002
68. Bezzi M, Teo SX, Muller J, et al. Regulation of constitutive and alternative splicing by PRMT5 reveals a role for Mdm4 pre-mRNA in sensing defects in the spliceosomal machinery. *Genes Dev*. 2013;27(17):1903-1916. doi:10.1101/gad.219899.113
69. Antonysamy S. The Structure and Function of the PRMT5:MEP50 Complex BT - Macromolecular Protein Complexes: Structure and Function. In: Harris JR, Marles-Wright J, eds. Cham: Springer International Publishing; 2017:185-194. doi:10.1007/978-3-319-46503-6_7
70. Anderson L, Henderson C, Adachi Y. Phosphorylation and rapid relocalization of 53BP1 to nuclear foci upon DNA damage. *Mol Cell Biol*. 2001;21(5):1719-1729. doi:10.1128/MCB.21.5.1719-1729.2001
71. Clarke TL, Sanchez-Bailon MP, Chiang K, et al. PRMT5-Dependent Methylation of the TIP60 Coactivator RUVBL1 Is a Key Regulator of Homologous Recombination. *Mol Cell*. 2017;65(5):900-916.e7. doi:10.1016/j.molcel.2017.01.019
72. Prabhu L, Wei H, Chen L, et al. Adapting AlphaLISA high throughput screen to discover a novel small-molecule inhibitor targeting protein arginine methyltransferase 5 in pancreatic and colorectal cancers. *Oncotarget*. 2017;8(25):39963-39977. doi:10.18632/oncotarget.18102
73. Kim H, Ronai ZA. PRMT5 function and targeting in cancer. *Cell Stress*. 2020;4(8):199-215. doi:10.15698/cst2020.08.228
74. Wu T, Millar H, Gaffney D, et al. Abstract 4859: JNJ-64619178, a selective and pseudo-irreversible PRMT5 inhibitor with potent in vitro and in vivo activity, demonstrated in several lung cancer models. *Cancer Res*. 2018;78(13 Supplement):4859 LP - 4859. doi:10.1158/1538-7445.AM2018-4859
75. Tao H, Yan X, Zhu K, Zhang H. Discovery of Novel PRMT5 Inhibitors by Virtual Screening and Biological Evaluations. *Chem Pharm Bull (Tokyo)*. 2019;67(4):382-388. doi:10.1248/cpb.c18-00980
76. Harrison RG, Greenman MJ, Mall FP, Jackson CM. Observations of the living developing nerve fiber. *Anat Rec*. 1907;1(5):116-128. doi:https://doi.org/10.1002/ar.1090010503
77. Jedrzejczak-Silicka M. History of Cell Culture. In: Rijeka: IntechOpen; 2017:Ch. 1. doi:10.5772/66905
78. Kapałczyńska M, Kolenda T, Przybyła W, et al. 2D and 3D cell cultures - a comparison of different types of cancer cell cultures. *Arch Med Sci*. 2018;14(4):910-919. doi:10.5114/aoms.2016.63743
79. Tanriverdi O, Tasar M, Yilmaz M, et al. Important milestones for cancer at the Nobel prize. *Indian J Cancer*. 2020;57(4):370-375. doi:10.4103/ijc.IJC_983_19
80. Jensen C, Teng Y. Is It Time to Start Transitioning From 2D to 3D Cell Culture? . *Front Mol Biosci* . 2020;7:33. https://www.frontiersin.org/article/10.3389/fmolb.2020.00033.
81. Langhans SA. Three-Dimensional in Vitro Cell Culture Models in Drug Discovery and Drug Repositioning . *Front Pharmacol* . 2018;9:6. https://www.frontiersin.org/article/10.3389/fphar.2018.00006.
82. Lee JY, Chaudhuri O. Modeling the tumor immune microenvironment for drug

discovery using 3D culture. *APL Bioeng*. 2021;5(1):10903. doi:10.1063/5.0030693
83. Costa EC, Moreira AF, de Melo-Diogo D, Gaspar VM, Carvalho MP, Correia IJ. 3D tumor spheroids: an overview on the tools and techniques used for their analysis. *Biotechnol Adv*. 2016;34(8):1427-1441. doi:https://doi.org/10.1016/j.biotechadv.2016.11.002
84. Clevers H, Tuveson DA. Organoid Models for Cancer Research. *Annu Rev Cancer Biol*. 2019;3(1):223-234. doi:10.1146/annurev-cancerbio-030518-055702
85. Edmondson R, Broglie JJ, Adcock AF, Yang L. Three-dimensional cell culture systems and their applications in drug discovery and cell-based biosensors. *Assay Drug Dev Technol*. 2014;12(4):207-218. doi:10.1089/adt.2014.573
86. Phan N, Hong JJ, Tofig B, et al. A simple high-throughput approach identifies actionable drug sensitivities in patient-derived tumor organoids. *Commun Biol*. 2019;2(1):78. doi:10.1038/s42003-019-0305-x
87. Pauli C, Hopkins BD, Prandi D, et al. Personalized In Vitro and In Vivo Cancer Models to Guide Precision Medicine. *Cancer Discov*. 2017;7(5):462 LP - 477. doi:10.1158/2159-8290.CD-16-1154
88. van de Wetering M, Francies HE, Francis JM, et al. Prospective derivation of a living organoid biobank of colorectal cancer patients. *Cell*. 2015;161(4):933-945. doi:10.1016/j.cell.2015.03.053
89. Lomberk G, Dusetti N, Iovanna J, Urrutia R. Emerging epigenomic landscapes of pancreatic cancer in the era of precision medicine. *Nat Commun*. 2019;10(1):3875. doi:10.1038/s41467-019-11812-7
90. Schönhuber N, Seidler B, Schuck K, et al. A next-generation dual-recombinase system for time- and host-specific targeting of pancreatic cancer. *Nat Med*. 2014;20(11):1340-1347. doi:10.1038/nm.3646
91. de Alboran IM, O'Hagan RC, Gärtner F, et al. Analysis of C-MYC function in normal cells via conditional gene-targeted mutation. *Immunity*. 2001;14(1):45-55. doi:10.1016/s1074-7613(01)00088-7
92. Nabet B, Roberts JM, Buckley DL, et al. The dTAG system for immediate and target-specific protein degradation. *Nat Chem Biol*. 2018;14(5):431-441. doi:10.1038/s41589-018-0021-8
93. Conradt L, Godl K, Schaab C, et al. Disclosure of erlotinib as a multikinase inhibitor in pancreatic ductal adenocarcinoma. *Neoplasia*. 2011;13(11):1026-1034. doi:10.1593/neo.111016
94. Parekh S, Ziegenhain C, Vieth B, Enard W, Hellmann I. The impact of amplification on differential expression analyses by RNA-seq. *Sci Rep*. 2016;6(1):25533. doi:10.1038/srep25533
95. Macosko EZ, Basu A, Satija R, et al. Highly Parallel Genome-wide Expression Profiling of Individual Cells Using Nanoliter Droplets. *Cell*. 2015;161(5):1202-1214. doi:10.1016/j.cell.2015.05.002
96. Bian B, Bigonnet M, Gayet O, et al. Gene expression profiling of patient-derived pancreatic cancer xenografts predicts sensitivity to the BET bromodomain inhibitor JQ1: implications for individualized medicine efforts. *EMBO Mol Med*. 2017;9(4):482-497. doi:https://doi.org/10.15252/emmm.201606975
97. Orben F, Lankes K, Schneeweis C, et al. Epigenetic drug screening defines a PRMT5 inhibitor sensitive pancreatic cancer subtype. *JCI Insight*. April 2022. doi:10.1172/jci.insight.151353

98. Behan FM, Iorio F, Picco G, et al. Prioritization of cancer therapeutic targets using CRISPR–Cas9 screens. *Nature*. 2019;568(7753):511-516. doi:10.1038/s41586-019-1103-9
99. Konermann S, Brigham MD, Trevino AE, et al. Genome-scale transcriptional activation by an engineered CRISPR-Cas9 complex. *Nature*. 2015;517(7536):583-588. doi:10.1038/nature14136
100. Yeo NC, Chavez A, Lance-Byrne A, et al. An enhanced CRISPR repressor for targeted mammalian gene regulation. *Nat Methods*. 2018;15(8):611-616. doi:10.1038/s41592-018-0048-5
101. Knudsen ES, Balaji U, Mannakee B, et al. Pancreatic cancer cell lines as patient-derived avatars: genetic characterisation and functional utility. *Gut*. 2018;67(3):508-520. doi:10.1136/gutjnl-2016-313133
102. Konermann S, Lotfy P, Brideau NJ, Oki J, Shokhirev MN, Hsu PD. Transcriptome Engineering with RNA-Targeting Type VI-D CRISPR Effectors. *Cell*. 2018;173(3):665-676.e14. doi:10.1016/j.cell.2018.02.033
103. Wessels H-H, Méndez-Mancilla A, Guo X, Legut M, Daniloski Z, Sanjana NE. Massively parallel Cas13 screens reveal principles for guide RNA design. *Nat Biotechnol*. 2020;38(6):722-727. doi:10.1038/s41587-020-0456-9
104. Raina K, Lu J, Qian Y, et al. PROTAC-induced BET protein degradation as a therapy for castration-resistant prostate cancer. *Proc Natl Acad Sci*. 2016;113(26):7124 LP - 7129. doi:10.1073/pnas.1521738113
105. Devaiah BN, Mu J, Akman B, et al. MYC protein stability is negatively regulated by BRD4. *Proc Natl Acad Sci*. 2020;117(24):13457 LP - 13467. doi:10.1073/pnas.1919507117
106. Ianevski A, Giri AK, Aittokallio T. SynergyFinder 2.0: visual analytics of multi-drug combination synergies. *Nucleic Acids Res*. 2020;48(W1):W488-W493. doi:10.1093/nar/gkaa216
107. Yadav B, Wennerberg K, Aittokallio T, Tang J. Searching for Drug Synergy in Complex Dose-Response Landscapes Using an Interaction Potency Model. *Comput Struct Biotechnol J*. 2015;13:504-513. doi:10.1016/j.csbj.2015.09.001
108. Tiriac H, Belleau P, Engle DD, et al. Organoid Profiling Identifies Common Responders to Chemotherapy in Pancreatic Cancer. *Cancer Discov*. 2018;8(9):1112 LP - 1129. doi:10.1158/2159-8290.CD-18-0349
109. Dantes Z, Yen H-Y, Pfarr N, et al. Implementing cell-free DNA of pancreatic cancer patient-derived organoids for personalized oncology. *JCI insight*. 2020;5(15). doi:10.1172/jci.insight.137809
110. Driehuis E, van Hoeck A, Moore K, et al. Pancreatic cancer organoids recapitulate disease and allow personalized drug screening. *Proc Natl Acad Sci*. 2019;116(52):26580 LP - 26590. doi:10.1073/pnas.1911273116
111. Braun CJ, Stanciu M, Boutz PL, et al. Coordinated Splicing of Regulatory Detained Introns within Oncogenic Transcripts Creates an Exploitable Vulnerability in Malignant Glioma. *Cancer Cell*. 2017;32(4):411-426.e11. doi:10.1016/j.ccell.2017.08.018
112. Qin Y, Hu Q, Xu J, et al. PRMT5 enhances tumorigenicity and glycolysis in pancreatic cancer via the FBW7/cMyc axis. *Cell Commun Signal*. 2019;17(1):30. doi:10.1186/s12964-019-0344-4
113. Wei X, Yang J, Adair SJ, et al. Targeted CRISPR screening identifies PRMT5 as synthetic lethality combinatorial target with gemcitabine in pancreatic cancer cells. *Proc Natl Acad Sci U S A*. 2020;117(45):28068-28079. doi:10.1073/pnas.2009899117
114. Roos WP, Kaina B. DNA damage-induced cell death by apoptosis. *Trends Mol*

Med. 2006;12(9):440-450. doi:10.1016/j.molmed.2006.07.007
115. Lin CY, Lovén J, Rahl PB, et al. Transcriptional amplification in tumor cells with elevated c-Myc. *Cell*. 2012;151(1):56-67. doi:10.1016/j.cell.2012.08.026
116. Han T, Goralski M, Gaskill N, et al. Anticancer sulfonamides target splicing by inducing RBM39 degradation via recruitment to DCAF15. *Science*. 2017;356(6336). doi:10.1126/science.aal3755
117. Ge L, Wang H, Xu X, et al. PRMT5 promotes epithelial-mesenchymal transition via EGFR-β-catenin axis in pancreatic cancer cells. *J Cell Mol Med*. 2020;24(2):1969-1979. doi:10.1111/jcmm.14894
118. Kryukov G V, Wilson FH, Ruth JR, et al. MTAP deletion confers enhanced dependency on the PRMT5 arginine methyltransferase in cancer cells. *Science*. 2016;351(6278):1214-1218. doi:10.1126/science.aad5214
119. Mavrakis KJ, McDonald ER 3rd, Schlabach MR, et al. Disordered methionine metabolism in MTAP/CDKN2A-deleted cancers leads to dependence on PRMT5. *Science*. 2016;351(6278):1208-1213. doi:10.1126/science.aad5944
120. Brehmer D, Beke L, Wu T, et al. Discovery and Pharmacological Characterization of JNJ-64619178, a Novel Small Molecule Inhibitor of PRMT5 with Potent Anti-Tumor Activity. *Mol Cancer Ther*. January 2021:molcanther.0367.2021. doi:10.1158/1535-7163.MCT-21-0367
121. Koh CM, Bezzi M, Low DHP, et al. MYC regulates the core pre-mRNA splicing machinery as an essential step in lymphomagenesis. *Nature*. 2015;523(7558):96-100. doi:10.1038/nature14351
122. Hsu TY-T, Simon LM, Neill NJ, et al. The spliceosome is a therapeutic vulnerability in MYC-driven cancer. *Nature*. 2015;525(7569):384-388. doi:10.1038/nature14985
123. Harrison JC, Haber JE. Surviving the breakup: the DNA damage checkpoint. *Annu Rev Genet*. 2006;40:209-235. doi:10.1146/annurev.genet.40.051206.105231
124. Hanahan D, Weinberg RA. Hallmarks of Cancer: The Next Generation. *Cell*. 2011;144(5):646-674. doi:https://doi.org/10.1016/j.cell.2011.02.013
125. Yang D, Liu H, Goga A, Kim S, Yuneva M, Bishop JM. Therapeutic potential of a synthetic lethal interaction between the MYC proto-oncogene and inhibition of aurora-B kinase. *Proc Natl Acad Sci U S A*. 2010;107(31):13836-13841. doi:10.1073/pnas.1008366107
126. Schneeweis C, Hassan Z, Schick M, Keller U, Schneider G. The SUMO pathway in pancreatic cancer: insights and inhibition. *Br J Cancer*. 2021;124(3):531-538. doi:10.1038/s41416-020-01119-6
127. Sachamitr P, Ho JC, Ciamponi FE, et al. PRMT5 inhibition disrupts splicing and stemness in glioblastoma. *Nat Commun*. 2021;12(1):979. doi:10.1038/s41467-021-21204-5
128. Espiau-Romera P, Courtois S, Parejo-Alonso B, Sancho P. Molecular and Metabolic Subtypes Correspondence for Pancreatic Ductal Adenocarcinoma Classification. *J Clin Med*. 2020;9(12):4128. doi:10.3390/jcm9124128
129. Tikhanovich I, Zhao J, Bridges B, Kumer S, Roberts B, Weinman SA. Arginine methylation regulates c-Myc-dependent transcription by altering promoter recruitment of the acetyltransferase p300. *J Biol Chem*. 2017;292(32):13333-13344. doi:10.1074/jbc.M117.797928

VIII. Publication list

1) Orben F, Lankes K, Schneeweis C, Hassan Z, Jakubowsky H, Krauß L, Boniolo F, Schneider C, Schäfer AP, Murr J, Schlag C, Kong B, Öllinger R, Wang C, Beyer G, Mahajan UM, Xue Y, Mayerle J, Schmid RM, Kuster B, Rad R, Braun CJ, Wirth M, Reichert M, Saur D, Schneider G. Epigenetic drug screening defines a PRMT5 inhibitor sensitive pancreatic cancer subtype. JCI Insight. 2022 Apr 19:e151353. doi: 10.1172/jci.insight.151353. Epub ahead of print. PMID: 35439169.

2) Schneeweis C, Hassan Z, Ascherl K, Wirth M, Koutsouli S, Orben F, Krauß L, Schneider C, Öllinger R, Krämer OH, Rad R, Reichert M, Robles MS, Saur D, Schneider G. Indirect targeting of MYC sensitizes pancreatic cancer cells to mechanistic target of rapamycin (mTOR) inhibition. Cancer Commun (Lond). 2022 Apr;42(4):360-364. doi: 10.1002/cac2.12280. Epub 2022 Mar 7. PMID: 35253411; PMCID: PMC9017755.

3) Doffo J, Bamopoulos SA, Köse H, Orben F, Zang C, Pons M, den Dekker AT, Brouwer RWW, Baluapuri A, Habringer S, Reichert M, Illendula A, Krämer OH, Schick M, Wolf E, van IJcken WFJ, Esposito I, Keller U, Schneider G, Wirth M. NOXA expression drives synthetic lethality to RUNX1 inhibition in pancreatic cancer. Proc Natl Acad Sci U S A. 2022 Mar 1;119(9):e2105691119. doi: 10.1073/pnas.2105691119. PMID: 35197278; PMCID: PMC8892327.

4) Peschke K, Jakubowsky H, Schäfer A, Maurer C, Lange S, Orben F, Bernad R, Harder FN, Eiber M, Öllinger R, Steiger K, Schlitter M, Weichert W, Mayr U, Phillip V, Schlag C, Schmid RM, Braren RF, Kong B, Demir IE, Friess H, Rad R, Saur D, Schneider G, Reichert M. Identification of treatment-induced vulnerabilities in pancreatic cancer patients using functional model systems. EMBO Mol Med. 2022 Apr 7;14(4):e14876. doi: 10.15252/emmm.202114876. Epub 2022 Feb 4. PMID: 35119792; PMCID: PMC8988213.

5) Lier S, Sellmer A, Orben F, Heinzlmeir S, Krauß L, Schneeweis C, Hassan Z, Schneider C, Patricia Gloria Schäfer A, Pongratz H, Engleitner T, Öllinger R, Kuisl A, Bassermann F, Schlag C, Kong B, Dove S, Kuster B, Rad R, Reichert M, Wirth M, Saur D, Mahboobi S, Schneider G. A novel Cereblon E3 ligase modulator with antitumor activity in gastrointestinal cancer. Bioorg Chem. 2022 Feb;119:105505. doi: 10.1016/j.bioorg.2021.105505. Epub 2021 Nov 20. PMID: 34838332.

6) Biederstädt A, Hassan Z, Schneeweis C, Schick M, Schneider L, Muckenhuber A, Hong Y, Siegers G, Nilsson L, Wirth M, Dantes Z, Steiger K, Schunck K, Langston S, Lenhof HP, Coluccio A, Orben F, Slawska J, Scherger A, Saur D, Müller S, Rad R, Weichert W, Nilsson J, Reichert M, Schneider G, Keller U. SUMO pathway inhibition targets an aggressive pancreatic cancer subtype. Gut. 2020 Aug;69(8):1472-1482. doi: 10.1136/gutjnl-2018-317856. Epub 2020 Jan 30. PMID: 32001555; PMCID: PMC7398468.

7) Dantes Z, Yen HY, Pfarr N, Winter C, Steiger K, Muckenhuber A, Hennig A, Lange S, Engleitner T, Öllinger R, Maresch R, Orben F, Heid I, Kaissis G, Shi K, Topping G, Stögbauer F, Wirth M, Peschke K, Papargyriou A, Rezaee-Oghazi M, Feldmann K, Schäfer AP, Ranjan R, Lubeseder-Martellato C, Stange DE, Welsch T, Martignoni M, Ceyhan GO, Friess H, Herner A, Liotta L, Treiber M, von Figura G, Abdelhafez M, Klare P, Schlag C, Algül H, Siveke J, Braren R, Weirich G, Weichert W, Saur D, Rad R, Schmid RM, Schneider G, Reichert M. Implementing cell-free DNA of pancreatic cancer patient-derived organoids for personalized oncology. JCI Insight. 2020 Aug 6;5(15):e137809. doi: 10.1172/jci.insight.137809. PMID: 32614802; PMCID: PMC7455062